CRANFIELD UNIVERSITY
LIBRARY

CRANFIELD UNIVERSITY

E CLAFFEY

A MATHEMATICAL MODEL OF DIAJET ABRASIVE WATER JET MACHINING

SCHOOL OF INDUSTRIAL AND MANUFACTURING SCIENCE

Ph.D THESIS

ProQuest Number: 10820962

All rights reserved

INFORMATION TO ALL USERS
The quality of this reproduction is dependent upon the quality of the copy submitted.

In the unlikely event that the author did not send a complete manuscript
and there are missing pages, these will be noted. Also, if material had to be removed,
a note will indicate the deletion.



ProQuest 10820962

Published by ProQuest LLC (2019). Copyright of the Dissertation is held by Cranfield University.

All rights reserved.
This work is protected against unauthorized copying under Title 17, United States Code
Microform Edition © ProQuest LLC.

ProQuest LLC.
789 East Eisenhower Parkway
P.O. Box 1346
Ann Arbor, MI 48106 – 1346

CRANFIELD UNIVERSITY

SCHOOL OF INDUSTRIAL AND MANUFACTURING SCIENCE

Ph.D THESIS

Academic Year 1995-6

E CLAFFEY

A Mathematical model of DIAJET abrasive water jet cutting

Supervisor: Dr. R. L. Allwood

April 1996

© Enda Claffey, BHR Group Limited 1996

Abstract

A mathematical model of ductile material cutting with an abrasive suspension jet has been developed. This is based on erosive wear of material by solid particle impact. The largest contribution is assumed to be from near-normal impacts. This 'deformation wear' causes work-hardening and subsequent brittle fracture of the material. A threshold velocity exists, below which no erosion takes place. The value of this velocity is dependent on the material ultimate tensile strength. The depth of cut achievable for a given traverse speed is dependent on the threshold velocity and the fracture strength of the material. For brittle fracture this has a value of E/10.

A simulation of particle acceleration within a cutting nozzle was also undertaken by applying the Navier-Stokes equation to the boundary conditions. This revealed that the particle velocity is almost identical to the theoretical (Bernoulli's) slurry velocity for the nozzles used in this project.

The model has been validated against a range of operating parameters such as pressure, abrasive, abrasive concentration, and material properties. This has confirmed the validity of the assumptions, with a good correlation. Some predictions, however, gave a better fit if only 60% of the measured abrasive discharge was used. Highly alloyed materials produced a less satisfactory fit to the model.

To Katie

ACKNOWLEDGEMENTS

I wish to express my sincere gratitude to all who helped me during my research. In particular, all the jetting staff (past and present) at BHR Group for their advice and assistance, my supervisors Dr R L Allwood, Mr R M Fairhurst, and Mr D Lowe who guided me in my work. Thank you to Dr G Oddie for his help in carrying out the laser anemometry measurements, and finally my family and friends for their support over the past three years.

TABLE OF CONTENTS

CHAPTER 1 - INTRODUCTION AND BACKGROUND 1

1.1 Introduction 1

1.2 Background 5

1.3 Generation of an abrasive water jet 7

1.3.1 Entrainment type abrasive water jet. 7

1.3.2 Pressurised slurry (suspension) abrasive water jet 9

1.4 Material erosion by solid particle impact 13

1.4.1 Cutting wear of ductile materials 14

1.4.2 Deformation wear of ductile materials 16

1.4.3 Brittle materials 18

1.4.4 Effect of the angle of attack 18

1.4.5 Effect of particle size 20

1.5 Cutting by abrasive water jet 24

1.5.1 Experimental trends 24

1.6 Optimisation of nozzle design 31

1.6.1 The structure of a turbulent water jet 31

1.6.2 Consideration of abrasive particle velocity 34

1.7 Characterisation of abrasive particles 38

1.7.1 Particle size 38

1.7.2 Abrasive material properties 39

1.7.3 Particle shape 39

1.7.4 Measurement techniques 40

CHAPTER 2 - REVIEW OF RELEVANT MODELS DEVELOPED 44

2.1 Solid particle erosion model 44

2.1.1 Finnie's Model 44

2.1.2 Bitter's model 51

2.1.3 Neilson and Gilchrist 60

2.1.4 Tilly 63

2.1.5 Fairhurst 66
2.1.6 Hashish 68
2.1.7 Sheldon and Kanhere 72
2.1.8 Jennings, Head, and Manning 74
2.1.9 Kim and Zeng 74
2.1.10 Hutchings 75
2.1.11 Kragelsky 77
2.2 Cutting by abrasive water jet 78
2.2.1 Hashish 78
2.2.2 Walters and Saunders 84
2.2.3 Abudaka 86
2.3 Review of acceleration models 89
2.3.1 Finnie 89
2.3.2 Fairhurst 90
2.3.3 Guo, Cheng, Liu 91
2.3.4 Shimizu and Wu 93
2.3.5 Pekarek, Lowe, and Huitt 94
2.3.6 Nadeau, Stubbley, and Burns 96
2.3.7 Benchaita, Griffith, and Rabinowicz 98

CHAPTER 3 - MODEL OF ABRASIVE WATER JET CUTTING 101
3.1 Cutting wear 103
3.2 Deformation wear 107
3.3 Threshold particle velocity 109
3.4 Material properties 109
3.5 System effects - calculation of particle velocity 112
3.5.1 Description of the forces arising 114
3.5.2 Continuity equations 115
3.5.3 Practical considerations 116
3.6 Prediction of abrasive particle velocity 117
3.7 Abrasive water jet prediction procedure 118

CHAPTER 4 - EXPERIMENTAL PROCEDURES 120
4.1 Introduction 120
4.2 Abrasive water jet parameters - measurement and control 120
4.2.1 Pressure (water velocity) 121
4.2.2 Traverse speed 122
4.2.3 Material properties 124
4.2.4 Abrasive material properties 124
4.2.5 Depth of cut 125
4.3 Pumping equipment 125
4.4 Abrasive water jet system 127
4.4.1 Abrasive metering control. 127
4.4.2 Abrasive discharge device 132
4.4.3 Piping requirements 133
4.4.4 Abrasive containing vessels 133
4.4.5 Nozzle 134
4.5 System calibration 135
4.6 Laser Doppler Anemometry 139

CHAPTER 5 - RESULTS AND DISCUSSION 143
5.1 Preliminary experimental results 143
5.2 Cutting trials 144
5.2.1 Brass CZ108 half-hard 144
5.2.2 Aluminium 147
5.2.3 Stainless steel 304L 148
5.2.4 Mild steel 148
5.2.5 Marble 149
5.2.6 Correlation of the abrasive water jet cutting model 149
5.3 Particle exit velocity 156
5.4 Discussion 158

CHAPTER 6 - CONCLUSIONS AND RECOMMENDATIONS 168

BIBLIOGRAPHY 170

REFERENCES 170

APPENDIX A - CALCULATION OF ENERGY ABSORBED BY IMPACTING SPHERES 178

APPENDIX B - GOVERNING EQUATIONS FOR TWO-PHASE FLOW 181

APPENDIX C - SAMPLE MATHCAD CALCULATION AND RESULTS ... 188

LIST OF FIGURES

1.1 Entrainment cutting head 9
1.2 Suspension jet systems 12
1.3 Erosive wear modes 17
1.4 Erosive rate vs. angle of attack (ductile) 19
1.5 Effect of particle size on erosive wear 22
1.6 Critical particle size effects 22
1.7 Effect of particle size on brittle erosion 23
1.8 Particle size effects in awj cutting 23
1.9 Effect of pressure on cutting performance 25
1.10 Effect of traverse rate on depth of cut 25
1.11 AWJ cut surface characteristics 27
1.12 Visualisation of AWJ cutting 29
1.13 Brass sample cut by awj 30
1.14 Development of a turbulent water jet 33
1.15 Combined roundness and sphericity 43
1.16 Size distribution of olivine AFS 80 43
2.1 Micro-machining 45
2.2 Erosive wear versus angle of attack 50
2.3 Stress distribution for impacting spheres 51
2.4 Effective radius of particle 54
2.5 Material erosion 59
2.6 Erosive wear characteristics 62
2.7 Erosion versus particle size 65
2.8 Predicted erosive performance of DIAJET system 67
2.9 Shape of eroded volume 67
2.10 Cutting wear 68
2.11 Development of the jet through the material 83
2.12 Step removal (deformation wear) 83
2.13 Water usage vs. abrasive concentration 85
2.14 Water usage vs. pressure 85

2.15 Velocity through the nozzle 94
2.16 Velocity increase through convergent section of nozzle 95
2.17 Velocity through the nozzle 98
2.18 Impinging awj 100
2.19 Particle trajectories in an awj 100
3.1 Step removal in deformation wear 102
3.2 Erosion by shallow particle impact 103
3.3 Cutting wear parameters 106
4.1 AWJ cutting table 123
4.2 High pressure, low flow pump with AC inverter drive 128
4.3 DIAJET circuit 129
4.4 DIAJET cutting system 130
4.5 DIAJET nozzles 136
4.6 DIAJET awj cutting 137
4.7 DIAJET abrasive discharge calibration 138
4.8 Laser Doppler anemometry - vector diagram 142
4.9 LDA experimental setup 142
5.1 69 MPa, 0.4 mm nozzle results 144
5.2 - 5.13 Predicted vs. actual DIAJET cutting 150-154
5.14 - 5.16 LDA measurement results 155
5.17 30 MPa LDA measurement result 156
5.18 Particle velocity through nozzle 158
5.19 Cut depth due to deformation wear 159
5.20 SEM analysis of AWJ cut surface 160
5.21-5.23 Cutting performance versus material properties 164
5.24-5.26 Cutting performance predictions 167

NOTATION

A	cross-sectional area of nozzle bore
α	angle of impact between the particle and the target material
α_0	angle of impact yielding maximum erosion
α_t	angle of impact at the top surface of the target material
b	width of erosion volume by a single particle
	width of spreading jet
B_a	inter-phase momentum transfer
c	fraction of particles cutting in an idealised manner
C_d	drag coefficient of particle
C_f	wall drag friction coefficient
d	abrasive particle diameter
δv	volume of material removed
ϵ	material specific energy for deformation wear
ζ	material specific energy for cutting wear
	coefficient of nozzle contraction
F_f	Wall drag friction force
H_d	depth of indentation at start of plastic deformation
H_{max}	depth of indentation after collision
I	particle moment of inertia
K	ratio of horizontal to vertical cutting reaction force
l	length of cut (particle/material contact length)
m	mass of abrasive particle
M	mass flow rate of abrasive particle
θ	orientation angle of particle
	half the nozzle inlet convergant angle
θ_0	initial orientation angle of particle
λ	coefficient of pipe friction
μ	dynamic viscosity
ν	kinematic viscosity
ν_1	Poisson's ratio of target material
ν_2	Poisson's ratio of abrasive material
P	operating pressure

ρ	density
σ	material flow stress
σ_y	elastic yield stress
σ_{uts}	ultimate tensile strength
Q_e	energy of elastic deformation
Q_{pe}	energy of elastic-plastic deformation
Q_p	energy to form permanent indent
r	particle radius
R	nozzle entry radius
R_x	horizontal cutting reaction force
R_y	vertical cutting reaction force
S	Wall shear stresses
t	time
τ	material shear strength
ϕ	ratio of vertical to horizontal reaction forces
ψ	length to depth ratio of the deformaed crater
ω	exit angular velocity
V	abrasive particle velocity
V_e	the threshold velocity for erosion
V_l	component of particle velocity parallel to surface of target material
$V_\perp$	component of particle velocity parallel to surface of target material
x	distance travelled by the particle parallel to the material surface
	distance travelled by particle through the nozzle
y	distance travelled by the particle perpendicular to the material surface
W	erosion rate

The following subscripts are used to make the above terms specific:

a	abrasive (material)
w	water
c	cutting wear
d	deformation wear
t	relative to the particle tip
m	properties of the pseudo-fluid

CHAPTER 1 - INTRODUCTION AND BACKGROUND

1.1 Introduction

The aim of this project is to acquire an understanding of the mechanics of abrasive water jet (AWJ) cutting as applied to the machining of material. In particular, we require a predictive model of cutting with abrasive suspension jets[1] to enable assessment of a potential range of operating conditions to achieve a particular task. This information can then be used to guide the development of future cutting systems. This work has been driven by a number of EU-funded projects directed towards increasing the competitiveness of abrasive water jet cutting in manufacturing industries such as jobbing shops and casting fettling.

Abrasive water jet machining is the name given to the process of material removal by abrasive particles suspended in a high velocity water-jet. It is a non-traditional 'power beam' machining technique, similar to laser and plasma cutting, where there is no direct mechanical contact between the tool and the material. Several advantages arise from such processes over traditional machining systems. Low reaction forces are important, but the lack of tooling costs, and thus cheap and fast-turnaround of designs, is possibly the most significant driving force behind these processes.

The rival power beam methods have limitations in that the heat generated during the cutting process may be unacceptable. In addition, the range of material types and thicknesses that can be cut is limited. Abrasive water jet cutting systems, on the other hand, do not rely on heat and thus create no heat affected zone. They have been used to cut almost every known material, to thicknesses of more than 300 mm. Advanced materials cutting, such as Metal Matrix Composites, are a particular example of where abrasive water jets excel.

However, in conventional cutting operations (for instance 10 mm thick stainless steel) abrasive water jets are much slower than its rivals with little improvement in operating

[1] An AWJ formed by expanding a high pressure suspension of water and abrasive through a single nozzle.

performance since their advent in the marketplace. Lasers, in contrast, have been continuously developed and are typically 4-5 times faster than current entrainment[2] type systems for the above material thickness.

The suspension jet AWJ systems offer the greatest potential to close this performance gap and make abrasive water jet cutting systems more attractive to the marketplace. To improve these systems, we must increase our knowledge of the cutting process by modelling the system\material interaction. This requires a model of abrasive water jet cutting which also considers the cutting systems to aid in their subsequent improvement.

Section 1.2 provides the background on cutting by abrasive water jet. Current abrasive water jet cutting equipment and its capabilities are discussed in section 1.3, and potential markets for future systems alluded to.

Section 1.4 reviews the existing theories of wear by solid particle erosion. Two mechanisms of erosive wear, differentiated by the angle of impact of the abrasive particle onto the material, have been identified [1]. At small angles of particle impact, a process similar to a single point cutting tool removes material [2]. This is known as the **cutting wear** mode and is predominant in the more ductile materials. The actual erosion rate increases sharply with increasing impact angles up to a maximum between 10°-20°. It then decreases just as sharply until this wear mode is no longer valid (20°-30°). At greater angles of impact wear occurs by fracture of the material. This **deformation wear** mode can be observed, to some extent, in all ductile and brittle materials. The erosion rate continues to decrease with increasing angle, but at a much lower rate, up to the maximum of 90°. Figure 1.4 shows the trend. In general, the erosion rate was found to be proportional to the particle velocity with an exponent of between two and three for **ductile classes** of material. For **brittle classes** of materials, this exponent is usually greater than three. A third mechanism, that of fatigue of the material surface, has also been proposed [3,4].

---

[2]An abrasive water jet system where the abrasive is entrained into a high-speed water jet via a venturi (see section 1.2.1).

The effect of abrasive particle size on cutting performance is given special mention, section 1.4.5. This is warranted due to the trend towards high pressure, small-diameter-nozzle suspension jets (0.2 mm and less). These systems operate with particle sizes (< 100 μm) previously thought to be ineffective for material removal [5, 6].

Section 1.5 reports on the experimental findings on abrasive water jet cutting, including a visualisation of the cutting process and examination of the surface generated by an AWJ.

In order to incorporate the cutting system into a mathematical model, it is necessary to identify and understand the key differences between systems. The two critical features of abrasive water jet systems identified during studies are the abrasive particle's exit velocity and the particle size reduction occurring during the acceleration process. Section 1.6 discusses some important aspects obtained from the papers, and from experimental analysis.

Finally, in section 1.7 the characteristics of the abrasive particles relevant to the mathematical models are mentioned. The transport characteristics of systems of abrasive particles, useful in developing cutting systems, are also discussed.

Chapter 2 presents the existing models of abrasive water jet cutting. Firstly, a review of models of material erosion by solid particle impact is given. This is followed with the models developed to describe abrasive water jet cutting. The review reports models developed from the theory of erosive wear and from empirical studies.

The cutting models encountered need to be improved to make them system dependent. In particular, the experimentally derived coefficients must be eliminated and a better estimate of the particle velocity (must be) included. One model of the cutting process appeared suitable as a basis of developing the model of a suspension jet system [7]. It combines Hashish's improved model of cutting wear (section 2.1.6) and Bitter's deformation wear [1]. The material properties used in the model were chosen based on experimental observations of the cutting process.

A review of particle acceleration is presented to facilitate incorporating the system into the model to be derived. Literature published since the start of this Ph.D have attempted to model the acceleration through the nozzle of suspension systems [8]; however, only one accurately describes the forces due to the extreme accelerations experienced during acceleration in the nozzle [9].

Chapter 3 reports the development of the mathematical model of cutting by suspension jet. A key part of this is the identification of the material properties influential in determining the material removal rate. The model accounts for abrasive shape and density, but not particle size, as this will be shown to be unimportant for practical particle sizes. Although this model could be used to predict cutting performance in both ductile and brittle material, this model is more suited for ductile materials. From the indications of projects running concurrently with my Ph.D, the need for a model for metal cutting is apparently greater than for brittle materials. The increased inhomogeneity of brittle materials limits the usefulness of a detailed model.

This chapter ends with a model to calculate the particle exit velocity for a suspension jet, and a comment on the apparent suitability of the model. This was derived from analysis of Navier-Stokes equations and considering conservation of momentum. The resulting model has been coded in Pascal for a Runge-Kutta approximation. With the complete equation of motion, the Stokes drag term normally considered for phase momentum exchange was overshadowed by other acceleration forces. The theoretical suspension velocity, dependent on the abrasive density and concentration, is a good approximation to the particle exit velocity for suspension jet systems.

An attempt was made to correlate the velocity predictions with experimental results. Laser Doppler anemometry was used to measure the jet exiting the nozzle. However, all the measurements taken were erroneous due to surface variations of the water jet. This model was also used independently of the cutting model to investigate the design of DIAJET nozzles.

Chapter 4 describes the experiments carried out to provide the test data to validate the model developed in chapter 3. The chapter ends with a complete description of the equipment used throughout this project.

Chapter 5 presents the results of the test work, and discusses the suitability of the combined model in relation to prediction of DIAJET cutting performance over a range of operating conditions. The test results obtained are used to analyse critically the models of the previous chapter. Future work is suggested to improve the results obtained.

Additional issues dealt with in this chapter are attempts to explain anomalies mentioned by previous researchers. Despite most claims to the contrary [5,6], experiments have shown that small particle sizes (less than 100 μm) do not significantly affect cutting performance, if sized to the nozzle diameter. By sizing is meant choosing particles with an average particle size of about one-third to one-half the nozzle diameter. This will always involve sieving the abrasive to avoid nozzle blockages.

Chapter 6 provides the conclusions to this project, with recommendations for future work.

1.2 Background

Man has always harnessed the power of water as a cheap renewable source. Watermills helped revolutionise the early industrial world while steam was the main source of motion for both transport and machinery.

We have always found new ways of using this never-ending resource and in the late 19th century water was used to mine gravel banks and goldmine's in California. This was later extended to coal pits where soft coal was literally washed down the pit face and collected at the bottom. With the development of reliable high pressure pumping equipment, water jets were used for applications such as marine fouling removal and drain-cleaning.

Water jets are now used extensively in the mining industry. Initially they were used to cool the drilling head, but as higher pressures became more easily attainable, the water jet was used to fracture the surface, reducing energy necessary for the actual drilling process. Similarly, these fracture cracks aid explosive charges in removing rock-faces.

The equipment first found its way into the production environment when used to descale billets. Impurities remaining on the surface of a billet leaving the furnace is removed using the impact and thermal force of a jet of cold water at pressures of up to 20 MPa. Similar pressure water jets can be used for cleaning and descaling castings, for example, engine blocks.

By the early 1970's high velocity water jets were used in industrial environments cutting paper, leather and other soft materials [10]. These applications still exist today as economical high pressure water jets have been made possible by the development of intensifier pumping systems.

Low pressure high flow water jets were used extensively for cleaning. However, when these proved inadequate on heat softenable material blocking pipe work, a venturi arrangement that drew steam into the jet was used to much better effect [11].

Research into cutting and cleaning by abrasive water jet has been carried out since the 1960's in the oil industry [12]. The abrasive water jet machining technique was first commercialised, however, in 1983 and has since been used for every conceivable cleaning and cutting operation. BHRA's Jet Cutting and Cleaning bibliographies show the wide-ranging applications of these tools [13-14]. In recent years the method has even been used for turning and machining although these are still in the early stages of commercial development. A more viable application for the techniques is two-dimensional profiling of material. The ability to cut almost any material has led to a concentration of effort in this market.

A significant advantage of abrasive water jet cutting is the inherent cold-cutting nature of the process that eliminates the heat affected zone produced by other machining methods. This also allows cutting in areas where there may be a risk of an explosion. Applications where such systems can be found are in nuclear decommissioning, also the demilitarisation market for disposing of now redundant weapons.

Recent developments in manufacturing trends have also spurred on the development of such machines. Just in time manufacturing requires a fast turnaround on small batches of products at economical prices. However traditional machining techniques (such as punches and presses) are proving too awkward for this evolving methodology. Prototype costs cannot be kept low when expensive dies must be made for possibly ten off, resulting in limited testing of concepts leaving a shortfall in the design strategy. Abrasive water jets are easily adapted to new designs, requiring only the reprogramming of a profiling table or robot.

1.3 Generation of an abrasive water jet

Abrasive water jets can be formed by two distinct methods. These are differentiated by when the abrasive is introduced into the system.

1.3.1 Entrainment type abrasive water jet.

The first method, the entrainment system, uses two nozzles. A small diameter orifice, called the primary orifice, produces a high velocity water jet. The depression formed by the venturi effect as this jet travels through the mixing chamber entrains abrasive (and air) into the jet. The abrasive continues to be accelerated by the water as the three-phase jet is collimated by a mixing tube typically four times the diameter of the primary nozzle and around 60 diameters in length.

Typical operating pressures are 350 MPa, with primary orifice and mixing tube diameters of 0.4 and 1.2 mm respectively. Figure 1.1 shows a schematic of an entrainment head. The need to create sufficient vacuum to achieve acceptable cutting rates currently limits the size of the nozzles to a minimum of 0.18 and 0.7 mm for the primary orifice and mixing tube.

The entrainment system is very simple, requiring only the design and manufacture of a jet pump [15]. The main disadvantage of this system is the loss in power density of the jet as it expands in the larger bore mixing tube. In addition, the abrasive concentration is limited to about 15% by weight of the water flow rate. Attempts to increase this value, by using multiple orifices or pressurised abrasive feed systems, have only been partially successful resulting in uneven abrasive flow and inconsistent cutting performance.

In addition, around 90% of the exiting jet is composed of air. This reduces the maximum theoretical velocity achievable with entrainment systems, further decreasing the efficiency.

The primary nozzle was conventionally made from synthetic sapphire that, although brittle, exhibits superior compressive strength to withstand the high pressures to which it is subjected. More recently synthetic diamond is being used, its superior heat conduction lessening thermal effects of the water boiling as it is accelerated.

Because of the chaotic nature of the mixing process, the jet produced is inhomogeneous resulting in considerable wear to the mixing tube and breakup of the abrasive particles. The conditions at entrainment are similar to the pure water cutting of geological materials like the silica-based abrasives frequently used in abrasive water jet cutting. This results in rounder and more crack-ridden particles less likely to damage the impacted surface.

Another consequence of this chaotic mixing is a nonsymmetric final jet, leading to inaccuracies in the machining process. Attempts to improve mixing, by the development of a radial array of abrasive entrances for example, have been unsuccessful. In certain designs, wet abrasive is drawn (or pumped) in, also with little improvement. The only real progress made to date has been the production of harder mixing tubes for a longer and more consistent life.

The mixing tube is made from the hardest material available, as the abrasive jet quickly wears this component. Toughness is also important to resist brittle fracture from the high

impact forces. Cermets are typically used, with the traditional Cobalt-bonded Tungsten Carbide cermets being increasingly replaced by Boron Carbide.

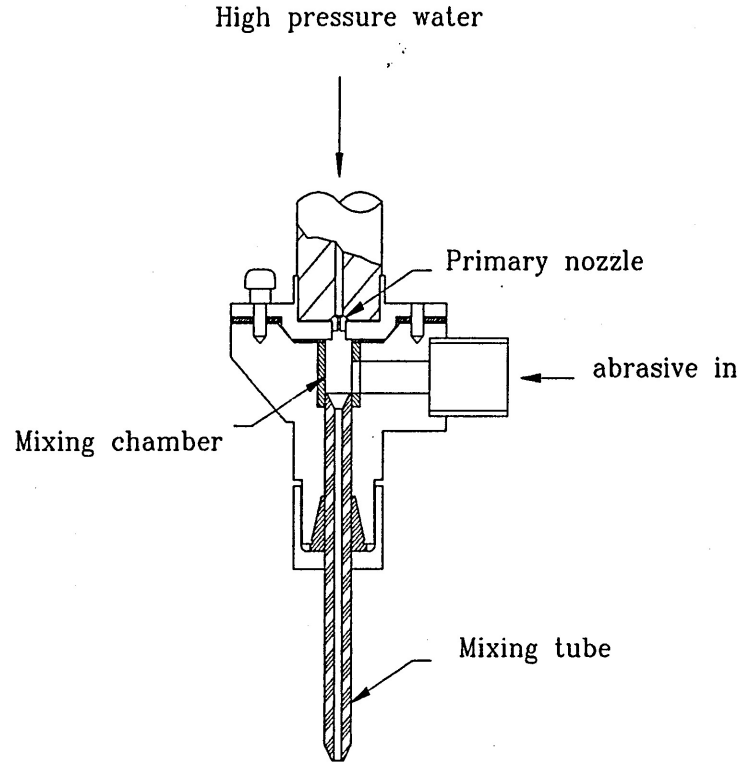

Figure 1.1 Entrainment cutting head [7]

1.3.2 Pressurised slurry (suspension) abrasive water jet

The second method of producing a high velocity water jet consists of pumping a premixed slurry of abrasive and water through a high pressure nozzle. This method requires a vessel (capable of withstanding the operating pressure) to contain the abrasive, and various components to isolate and meter the abrasive. The efficiency rises significantly over entrainment systems with denser jets and less particle damage during acceleration. However, the need for vessels operating at system pressure has constrained typical operating pressures to 35-69 MPa due to the lack of availability of low cost vessels at the higher pressures.

Two different principles of operation are employed in producing a pressurised slurry abrasive water jet, differentiated by how the abrasive is metered into the water flow.

(a) The first involves metering a percentage of the total water flow through the vessel to discharge abrasive stored within. This discharged grit combines with the remainder of the flow and the mixture is subsequently expanded through a nozzle to produce the high velocity jet [16]. This type of system is known as a direct injection abrasive water jet, and is the basis of the DIAJET system under investigation in this study.

(B) The alternative design is the abrasive suspension jet [17]. In this design the abrasive is held in suspension in the vessel. This is achieved by mixing additives with the water, usually flocculants. The vessel itself is usually separated into two parts by a floating piston. The top half contains the motive fluid usually water supplied from an intensifier. The lower half contains the suspended abrasive. This mixture is pumped out by pumping clean water into the top volume, and subsequently expanded in a nozzle. This system is less complicated than the DIAJET system as fewer components see abrasive flows.

Figure 1.2 shows schematics of both systems. Both of the systems shown are manual, or batch, systems. Once the vessel has discharged all the grit the system must be shut down and the vessel refilled at atmospheric pressure. Generally a system incorporating two vessels is employed to allow continuous operation of the system. While the first vessel is discharging, the other is being recharged at low pressure. Isolation is achieved by incorporating check valves into the lines connecting the vessels to the nozzles.

In the literature all types of systems using a single nozzle (to expand a high pressure, water and abrasive mixture) are termed abrasive suspension jets, to distinguish them from the more traditional entrainment-type abrasive water jet (section 1.3.1 above).

The suspension jet suffers fewer nozzle wear problems than the entrainment system, above. The water and abrasive are mixed while at low velocity and then gradually accelerated through the nozzle. Careful design aims to keep the abrasive in the middle of the jet and

away from the nozzle wall. Particle degradation is therefore less than that occurring in entrainment systems resulting in efficiency gains over the entrainment system. Also, nozzle sizes can be smaller resulting in more efficient and accurate cut surfaces with better surface finish due to the smaller size particles being used.

The additional complexity of pressurised slurry systems coupled with the lack of abrasive resistant high pressure components (specifically valves) has, until recently, precluded this design from making an impact on the precision machining market. Never-the-less this system has made a considerable impact on the offshore contracting and decommissioning market where the high initial cost is more than compensated for by the performance. The use of pressurised slurry also enables the system to operate underwater at depths not possible with conventional entrainment systems.

Current research cutting systems operate at pressures similar to entrainment systems, giving a three to five-fold increase in cutting performance.

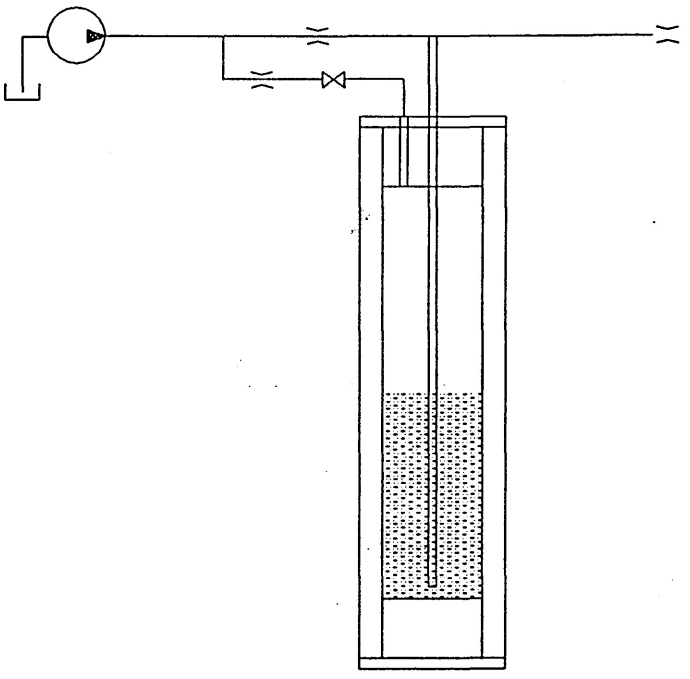

Figure 1.2a DIAJET pressurised slurry system [16]

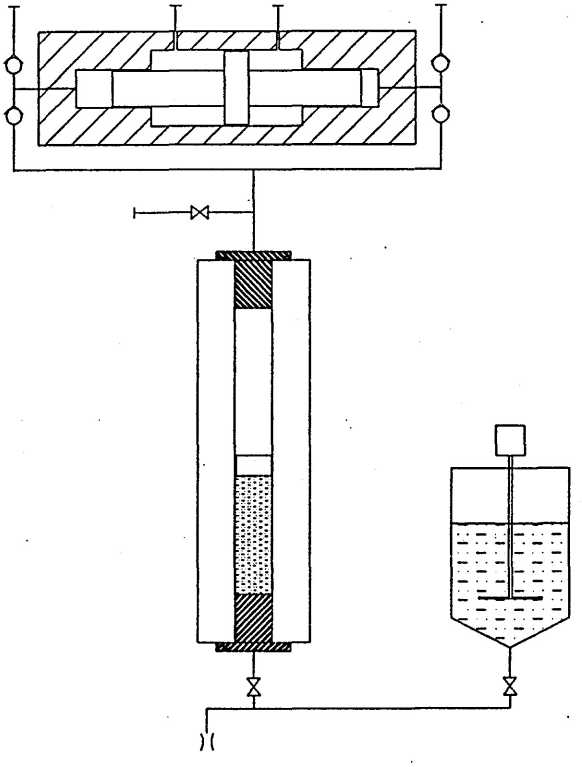

Figure 1.2b Suspension jet system [17]

1.4 Material erosion by solid particle impact

All material removal takes place by the wear of material whether by liquid, solid or gaseous means. One of these wear mechanisms, erosion, is defined as the removal of material from a solid surface due to mechanical interaction between the surface and *impinging* particles in a fluid stream. These particles may be solid (as in this study), liquid drops (in steam turbines for example), or gaseous (causing cavitation on collapse). Abrasion, on the other hand, is the loss of material that occurs when particles or other proturbences are *forced* against and *move along* the solid surface [18].

The essential difference between the two is that erosion involves the transfer of kinetic energy to the surface and abrasion does not. This means that in erosion, material removal varies with the velocity squared of the impinging particles (or some greater power). Abrasive wear, on the other hand, is a linear function of the velocity (and the applied force).

Investigations into the erosive wear of materials have been carried out from the 1930's, when DeHaller [19] distinguished two types of erosive mechanisms of metals. He also showed that this erosion could be distinguished by the angle of impact of the particle. Wellinger [20] investigated the effects of erosion on low and high carbon steels, exhibiting ductile and brittle properties respectively. The trials showed that soft ductile materials were more resilient to large (normal) impact angles than low, while the converse holds true for the more brittle material. This work was expanded on by Wellinger and Uetz [21] and provides the basis for most of the existing models of particle erosion. Holtey [22] also attributed the material removal in erosion to two distinct processes, which he called "rubbing" and "shock" wear. Hard steels were found to resist "rubbing" wear best, while softer steels resistant "shocks" imparted by eroding abrasives better.

Bitter identified the two erosion modes as cutting wear and deformation wear, distinguished by the angle of impact of the abrasive particle on the surface [1]. He explained mathematically that the cutting wear mode prevails at shallow angles of impact while the deformation wear mode becomes dominant at larger angles. He distinguished between these

erosion modes in ductile and brittle classes of material. Ductile material is more vulnerable to cutting wear while brittle materials (including hard metals) tends to wear via the mechanism of deformation wear. The following study will consider these two modes separately.

1.4.1 Cutting wear of ductile materials

Holtey's rubbing wear of soft materials [22] was explained by Finnie [2,23] and Bitter [1] to be particle impacts at low trajectory angles. In this cutting wear mode, the particle strikes the material and machines out a small chip while slightly rotating backwards [2]. The material here is removed by a cutting or displacing process, as in metal cutting or grinding.

This explanation of cutting wear applies for angular particles with sharp edges, equivalent to cutting tools of small, positive, rake angles. It is commonly called micro-machining, to distinguish from the following descriptions of cutting wear. Figure 1.3a shows the different types of cutting wear described here.

Hutchings and Winter [24], Hutchings [25] distinguished a further two mechanisms of low angle impacts. These were called ploughing deformation and cutting deformation, caused by spherical particle and angular particle impact respectively.

In ploughing deformation, a spherical particle extrudes the metal in front of it into a lip of approximately 10% to 25% of the crater volume. This lip is subsequently removed by a combination of fresh particles, and fragments of the previous particle. Particles with a large, negative rake angle will produce a similar effect, leaving a characteristic deep triangular-shaped crater. The particles rotate forward during cutting and exit with considerable rotational energy. This Hutchings termed cutting deformation [25].

For lower values of rake angles the particle will rotate backwards during cutting, producing a shallower, longer, crater with the lip removed, i.e. the micro machining mentioned earlier.

The possibility of material removal by particle fragments was investigated by Tilly [5]. He showed photographic and metallurgical evidence for a two-stage erosion process. Initially, the impacting particle produces an indentation and possibly removes a chip of metal. Particle fragments are projected radially from the primary site, producing secondary erosion. The findings of Maji and Sheldon [26] supported Tilly's two stage mechanism for brittle abrasive particles.

Smeltzer et al. [27] observed thermal effects in the machined craters for a wide range of metal alloys and heat treatments. Micro-smearing of the metal was observed suggesting the presence of localised temperatures approaching or exceeding the melting point of the metal. A thermal model of erosion is proposed, the impacting particle's energy being sufficient to cause localised melting The erosion rate decreases with increasing angles of impact, as more of the eroded material is redeposited on the surface.

Jennings et al. [28] also studied erosion from consideration of thermal effects. Here, the molten material was assumed to adhere to, and be removed by, the previous particles.

Winter and Hutchings [29] considered adiabatic-shear effects that are more dominant in metals such as titanium. Localised deformation results from the thermal softening of metals, causing both shear and tensile stresses in the material.

Bellman and Levy [30] and Levy [31] suggested a platelet mechanism of erosion. Particle impacts give rise to localised work-hardening of the surface. Repeated impacts produce a surface of hardened platelets, and once a steady strength and depth are achieved erosion occurs. This theory accounts for the apparent delay in the steady state erosion of materials. Such an unsteady process can be seen in the "flicking" of the emerging jet during cutting.

Kragelsky explained low impact angle erosion in terms of the fatigue theory of solid body erosion [32]. Wear occurs from the repeated rupture of friction bonds between the abrasive and the material. As the particle proceeds in its trajectory, an alternating stress distribution

(compressive in front, tensile behind) is set up and ultimately leads to fracturing of the material surface [33].

1.4.2 Deformation wear of ductile materials

The above methods of material erosion are also possible with large angles of impact. Those based on the scratching and subsequent removal of a chip would have little contribution from near normal impacts. Finnie suggests that the initial impacts leave a roughened surface, and therefore near-normal impacts never occur in steady state [2]. Most researchers, however, support variants of the theory of strain-hardening and subsequent fracture of the surface [1,4].

A model of particle embedding for softer materials has been suggested by Cousens and Hutchings [34]. This new layer of pseudo-material containing the embedded particles is fractured away during subsequent impacts. Edington and Wright postulated a similar theory [35]. Figure 1.3b details the mechanisms discussed for deformation wear.

The platelet mechanism discussed earlier [30, 31] has also been investigated by Rickerby and MacMillan [36-38] for deformation wear of aluminium. A threshold velocity of greater than 200 m/s has been shown to exist for chip removal of polycrystalline aluminium [39, 40], and a similar value is required for normal impacts to cause shear lip formation at the crater rim [41]. Thus, chip removal is unlikely to account for much erosion here.

Other proposed mechanisms of near normal impact erosion include Tilly's model of secondary erosion by fractured particles [5]. This mechanism is more evident at high impact angles of impact and is more suitable for large and soft types of particles.

The thermal effects proposed by Smeltzer et al., mentioned for cutting wear, are also applicable to deformation wear [27].

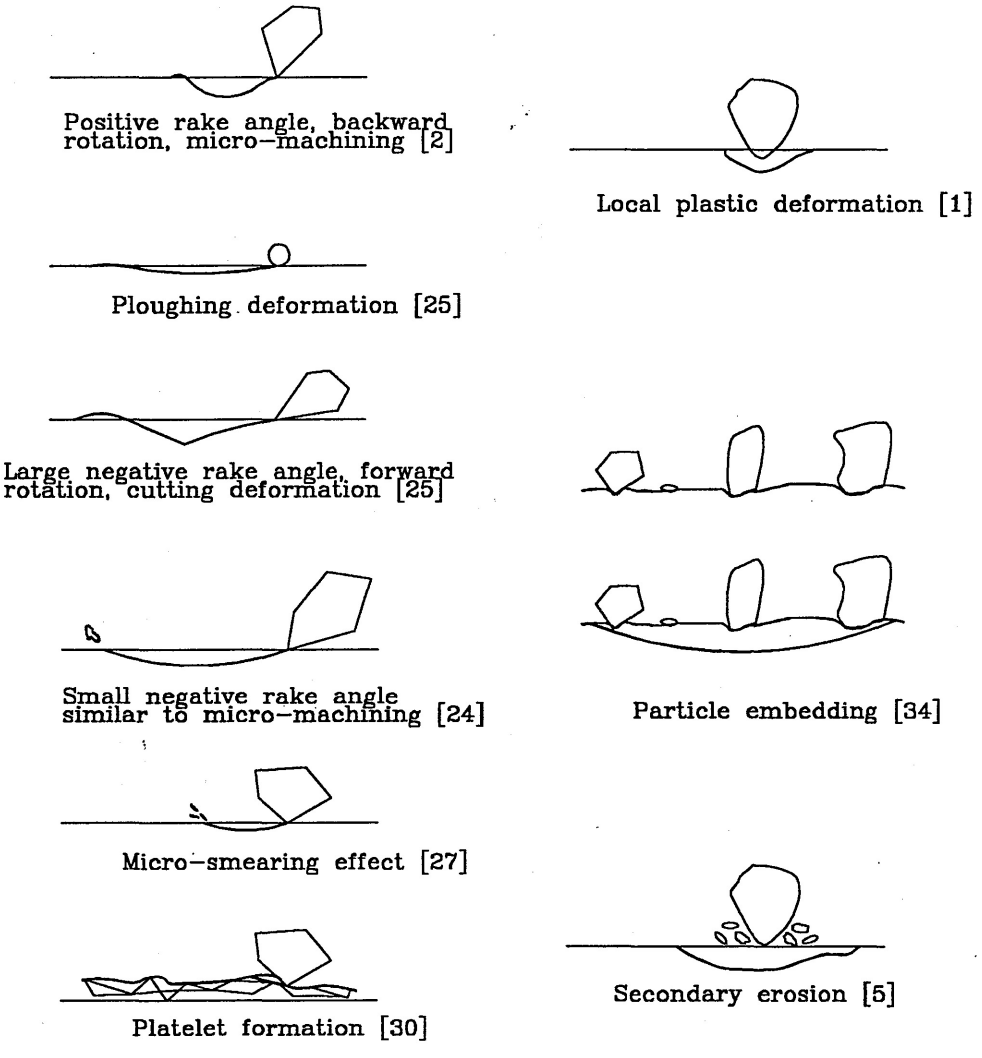

(a) Shallow angles of impact (b) Large angles of impact

Figure 1.3 erosive wear modes

1.4.3 Brittle materials

Although the study of brittle material erosion is more complex than that of ductile materials, there is less disagreement over the actual mechanism responsible. Repeated impacts cause crack growth and subsequent fracture of the material.

Studies of quasi-static erosion tests over a range of brittle materials have yielded eroded surfaces consisting of three types of cracks [42]. These are radial cracks, spreading out from the periphery of the crater during initial loading of the surface; subsurface circular cracks formed within the plane of the load axis at higher loads; and lateral cracks propagating parallel to the surface during unloading. Further trials on solid particle impacts revealed Hertzian conical cracks under fully elastic contact [43]. Their formation depends on the abrasive particle size and the material stress intensity factor [44].

Above a certain value of impact loading the purely elastic response becomes elastic-plastic and the three types of crack mentioned above occur. This transition impact load depends on the material hardness, the fracture toughness and the surface characteristics of the target.

In addition, Sheldon and Finnie showed that small angles of impact can cause plastic deformations, the brittle material appearing similar to the ductile micro machining process discussed previously [45]. Normal angle impact of small particles below a certain critical size also results in plastic flow rather than cracks in brittle materials. Brittle materials will behave in a ductile manner if the impacting particle velocity exceeds a minimum value. This may be a result of small particles impacting between surface flaws with no crack propagation. These phenomena were found less likely to occur if the material is significantly harder than the abrasive particle.

1.4.4 Effect of the angle of attack

As well as identifying two different erosion modes distinguished by impact angle, most researchers observed that the erosion rate was dependent on the impact angle within each mode. This can be clearly seen in the results of Finnie [2]. In figure 1.4 the maximum

erosion rate occurs for an impact angle of between 10°-20°, with the erosion rate falling sharply to zero for decreasing angles of attack. For larger angles, the erosion rate initially drops sharply, then decreases at a much slower rate. This change is due to the deformation wear mode taking over shortly after the maximum value of erosion rate. However, Finnie believed that only cutting wear took place in erosion [2]. Although this would predict zero erosion for impacts normal to the surface, Finnie presumed that initial low-impact angles produced a roughened surface. Therefore, near normal impacts were impossible.

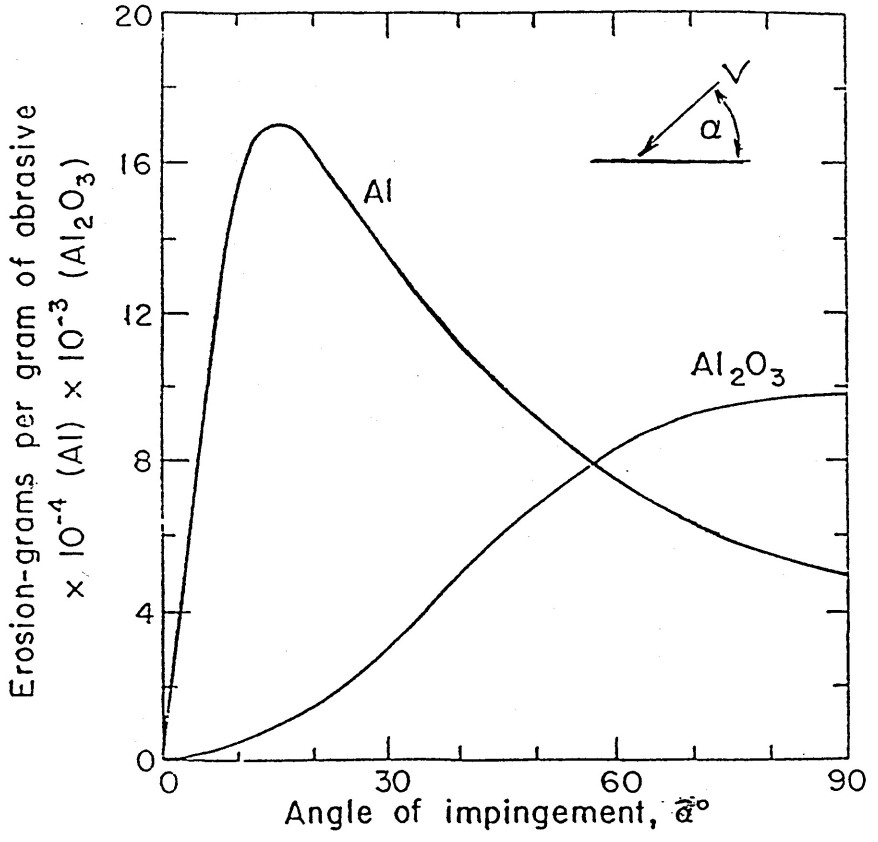

Figure 1.4 Erosion rate versus angle of attack [2]

1.4.5 Effect of particle size

Generally, it has been observed that erosion increases with an increase in particle size for both ductile materials [5, 27, 45] and brittle materials [45-47]. However, the majority of erosion and cutting wear models encountered do not attempt to include particle size effects.

Contrary to this, Tilly bases his model of erosion on the existence of particle size effects. He showed that fragmentation of large particles upon impact will cause additional secondary erosion [5]. The probability of small particle breakage and consequently, the probability of secondary erosion, is low. Smaller particles will thus produce decreasing levels of erosion, figure 1.5. Eventually a particle size is reached below which no erosion takes place. This value is highly dependent on a number of parameters, particularly particle velocity.

Smeltzer et al. [27] experimentally showed that volume loss per single particle is linearly proportional to the volume of the single particle in the range 1 to 200 microns, as shown in figure 1.6. This graph also confirms the existence of a critical particle size below which no erosion occurs, in this case 20 microns.

Fairhurst observed a marked decrease in erosion with decreasing particle size [6]. Particles below 150 microns were found to be less than half as effective as larger particles for the suspension jet system used. This is an important observation, given that one objective of this project is to predict the potential performance of the descendants of Fairhurst's system (i.e. DIAJET) using abrasive smaller than the minimum size quoted.

Budinski and Chin showed a linear relationship between particle diameter and crater area. The maximum crater area observed was about d/3, while the maximum crater depth was about d/10, where d is the particle diameter [48]. Observations on critical particle size are also reported in Misra and Finnie [49]. Sheldon and Finnie [45] showed that the erosion mode of brittle materials will become ductile for small particle sizes at high speeds, as shown in figure 1.7. Also that particle size does not influence volume removal, provided that the size is greater than about 100 microns [50].

Misra and Finnie studied the size effect of the abrasive particles on erosive wear to identify the mechanisms by which particle size affects wear results [9]. They excluded the secondary erosion model proposed by Tilly [5], in which particle fragmentation causes further erosion as particle size increases. They also excluded other factors related to abrasion on the basis that abrasion and erosion processes should be similar as far as particle size is concerned. They concluded that the material near the eroded zone exhibits higher flow stress for small particles than for large particles. Hutchings attributes the size effects to the material strain rate sensitivity. As the particle size decreases, the strain rate, and consequently material resistance to erosion, will increase [39].

Hashish [51], however, experimentally identified the existence of an optimum particle size for many materials when cutting with an entrainment abrasive water jet, (figure 1.8). This is contrary to the erosive behaviour mentioned above, and contradicts the supposition by many researchers that particles below 100-150 microns would not be effective in erosion [5, 6, 50]. This discrepancy is most likely due to the effect of particle-particle interactions within the system and the effect of particle size and volume on the drag forces experienced by a single particle. Another explanation may be the interaction of the particles with the boundary layer of the jet as well as the interaction with the rebounding water jet. These effects would be greater at the higher pressures, and hence velocities, used by Hashish with the abrasive water jet.

For brittle materials, no controversy exists on the effect of particle size, as larger particles will induce more cracks and consequently more erosion. The erosion rate is most commonly attributed to being proportional to the particle diameter to the fourth power [47, 52].

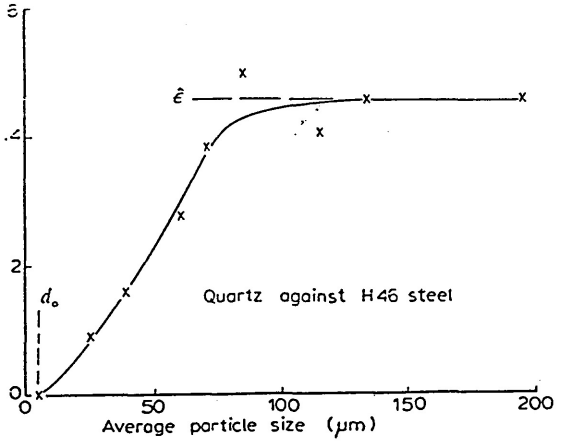

Figure 1.5 Effect of particle size on erosive wear [5]

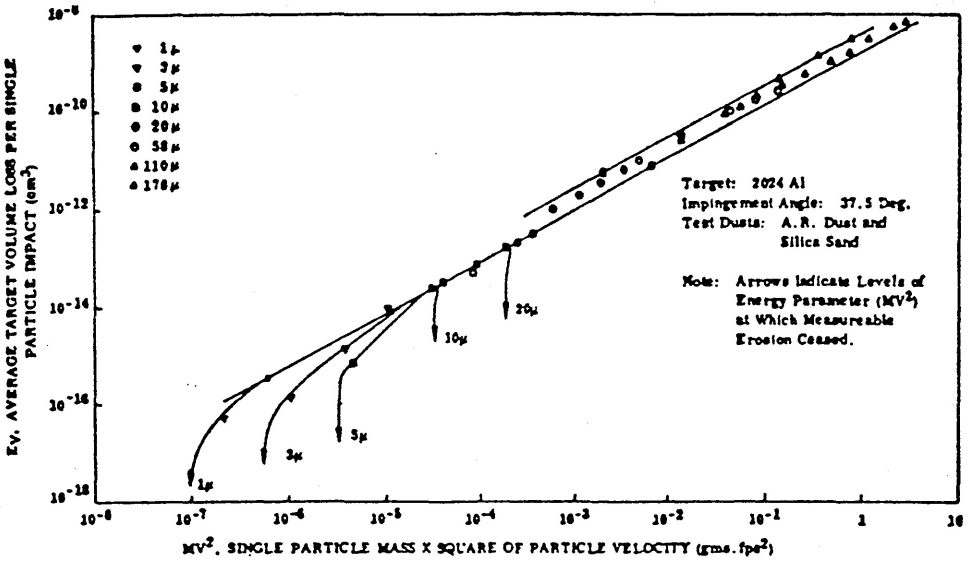

Figure 1.6 Critical particle size effects [27]

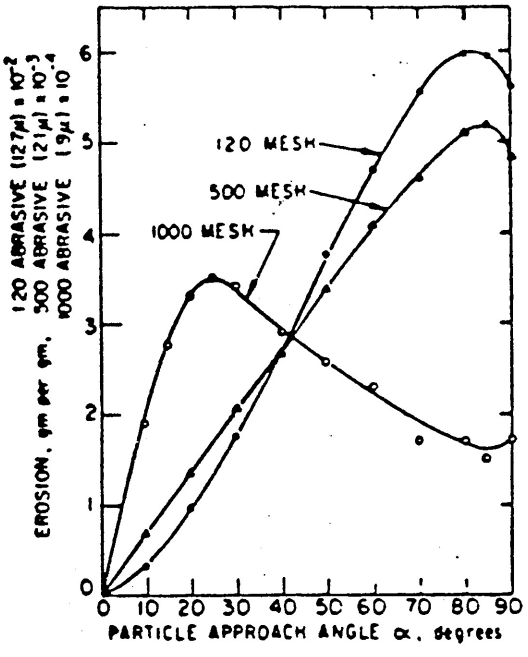

Figure 1.7 Effect of particle size on brittle erosion [50]

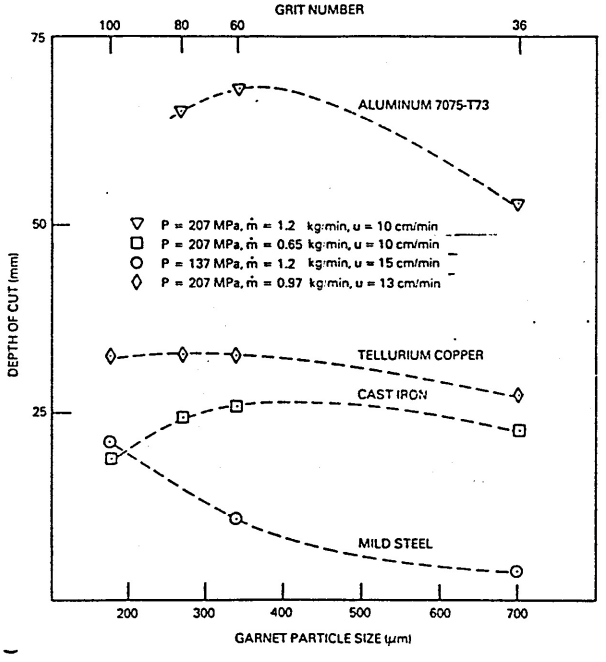

Figure 1.8 Particle size effects in AWJ cutting [51]

1.5 Cutting by abrasive water jet

Section 1.4 above, contains an account of experimental investigation of solid particle erosion. The key findings are the relationship between erosion rate and particle velocity, as well as the variation of the erosion rate with the angle of attack. For the purposes of analysis of abrasive water jet cutting systems, the effect of particle size may also be significant. The following sections describe the effect of operating parameters on the cutting performance of abrasive water jet systems. The characteristics of the generated surface are also discussed.

1.5.1 Experimental trends

Material cutting by abrasive water jet is a complicated process, involving not only the operating parameters of the cutting system (pressure, flow rate), but also the speed of traversal of the target material and the abrasive particle parameters themselves. The efficiency of the various methods used to produce an abrasive water jet also has a large impact on performance figures produced from different systems. The following information has been experimentally determined for an entrainment system [51]. Similar comparisons for a suspension jet will be shown in chapter 5 based on the results of experiments carried out during this project.

The achievable depth of cut at a fixed traverse speed is chosen as the means of comparing changes in operating parameters. The parameter considered to have the largest effect is the operating pressure. Cutting performance has been found to be linearly proportional to this variable, figure 1.9. As the water jet velocity is proportional to the square root of this value, and particle velocity assumed proportional to the water velocity, this implies cutting efficiency proportional to the kinetic energy of the particle. This is lower than the exponent of velocity of 2.5 found from cutting wear erosion, suggesting that deformation wear is the predominant mode for abrasive water jet cutting. In addition, a threshold pressure was found, below which cutting of the material would not occur. This is equivalent to Bitter's identification of a threshold velocity [1].

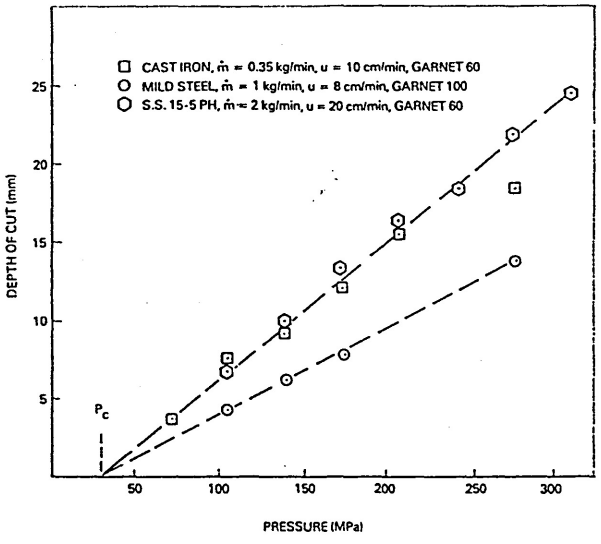

Figure 1.9 Effect of pressure on cutting performance [51]

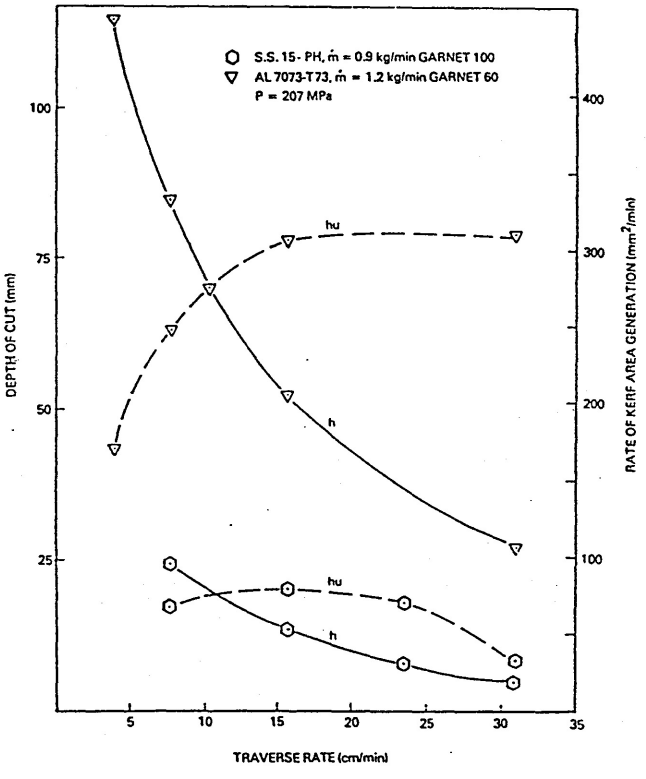

Figure 1.10 Effect of traverse rate on depth of cut [51]

The effect of the traversal rate on cutting depth is shown in figure 1.10. This graph also contains the product of traverse rate and cut depth, showing the existence of an optimum cutting condition for maximum material removal. This suggests that multi-pass cutting, where only a portion of the material depth is cut during each traversal of the jet, may be more efficient in some cases than single pass cutting. However, the cut surface quality is likely to be poor, and so this is of limited use in precision machining operations.

The influence of the abrasive is also of interest, particularly considering the cost of some abrasives is four times higher than others (garnet versus silica sand for instance). As expected, cutting depth increases with increasing abrasive usage. However, this relationship is slightly less than linear. This fact is attributed to reduced particle velocities and increased particle interaction (damage) with increased mass loading of the abrasive water jet. Cutting depth is also seen to increase slightly with increasing abrasive density.

A decrease in abrasive particle size has been shown to yield an increase in cutting depth, as can be seen from figure 1.8. The higher velocity attained by smaller particles during acceleration as well as their tendency towards sharper edges could explain this observation. However, it does contradict the findings of the experiments on solid particle erosion, where the converse was found. A possible cause for this anomaly is the influence of the boundary layer on a particle's trajectory, as discussed in section 1.4.5.

1.5.1.1 Visualisation of the cutting process

Abrasive water jet offers significant advantages over traditional machining techniques, section 1.2. However, this and other non-contact machining methods do have some disadvantages. The most significant of these are the deviation from the required profile as the jet changes direction, known as overshoot and the edge taper due to the divergence of the jet. The possibility of abrasive particles remaining embedded in the cut material can cause a problem in some applications also, as in the aerospace industry. Burrs are also evident on certain materials, especially aluminium. Figure 1.11 shows the characteristics of a surface cut by an abrasive water jet [53].

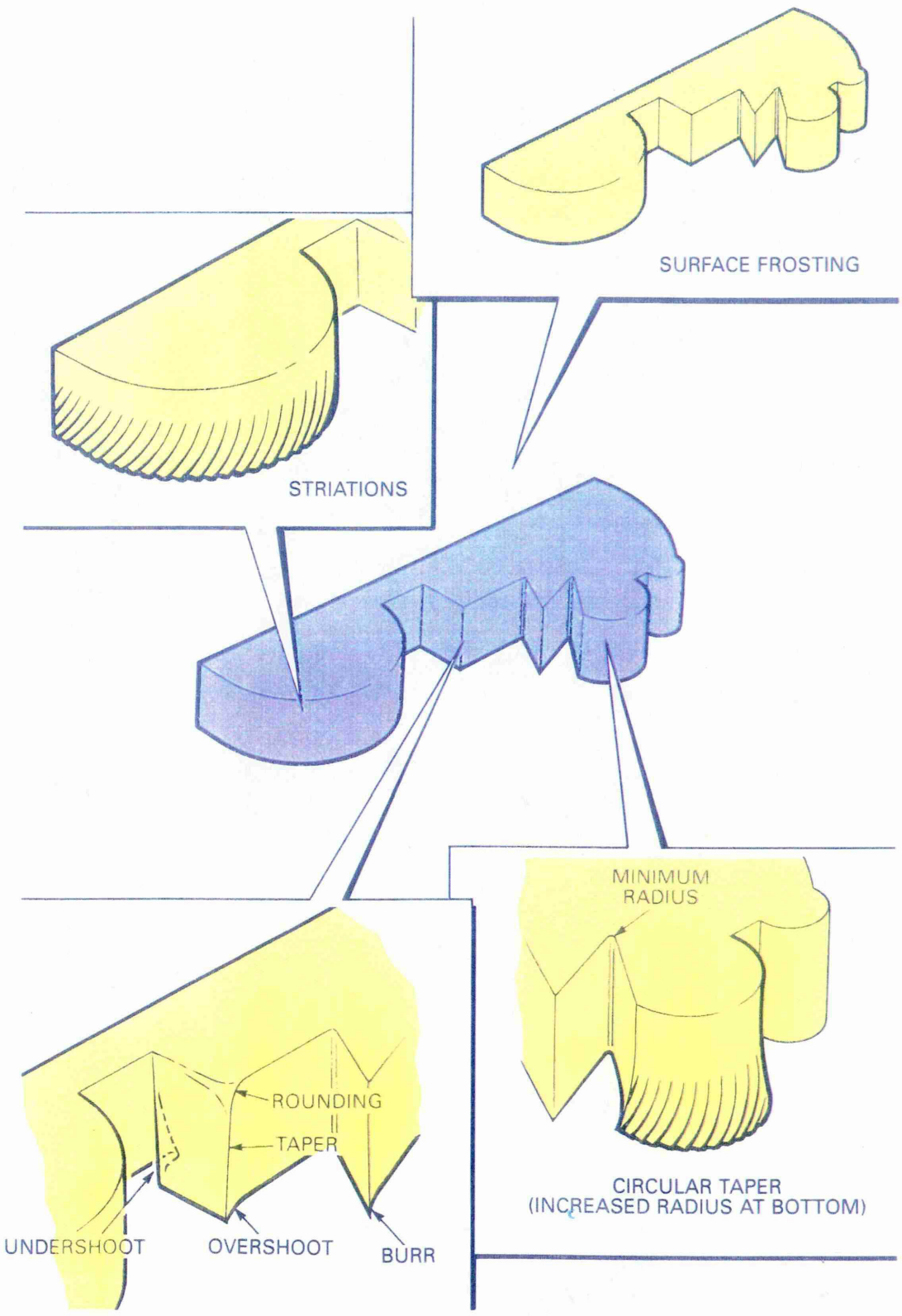

Figure 1.11 AWJ cut surface characteristics [53]

An abrasive water jet system delivers a high velocity beam of water and abrasive particles towards the intended target. Upon leaving the nozzle, this beam starts to diverge, much as a pure water jet. The distance between the nozzle exit and the workpiece, called the stand-off distance, determines the width (or kerf) of the cut. Although this jet is too complicated to analyse, the spreading characteristics of a pure water jet can give some insight into the analysis of an abrasive water jet. This is further discussed in section 1.6. The spreading of water jets can be delayed by the addition of viscosity-enhancers into the mixture [54].

High speed cameras have been used to observe the AWJ cutting of transparent materials [51]. A schematic of the cutting process is shown in figure 1.12. This clearly shows the two cutting modes [1]. A steady state interface exists to a depth of h_c, the limit of cutting mode wear. At the workpiece exit an uncut triangle of material is observed, showing the step normally removed during the deformation wear cutting mode.

In piercing, or hole drilling, the jet erodes the material by deformation wear alone. For entrainment systems, the air contained within the expanding jet allows the mixture to exit the hole. For suspension jets this waste product generates a contra-flow in the pierced hole, which has the effect of retarding the incoming jet. The effect of this is readily evident in the erosion tests of Fairhurst [6] where the trajectory of small particles is greatly altered by the exiting jet.

1.5.1.2 Characteristics of surfaces cut using abrasive water jets

Figure 1.13 shows a photograph of a brass sample cut by an abrasive water jet. The edge taper shown in figure 1.11(decreasing width) is the most widely achieved edge profile. The rounded top edge is a result of jet spreading between the nozzle exit and the material. However, it is possible to achieve the inverse profile or a combination of the two, resulting in barrel-shaped edges. These cuts are commonly found in the DIAJET cutting of thick material, the barrel shape being predominant for greater stand-off distances. Such a feature can be put to advantage, for example the slotting of pipes to make filters.

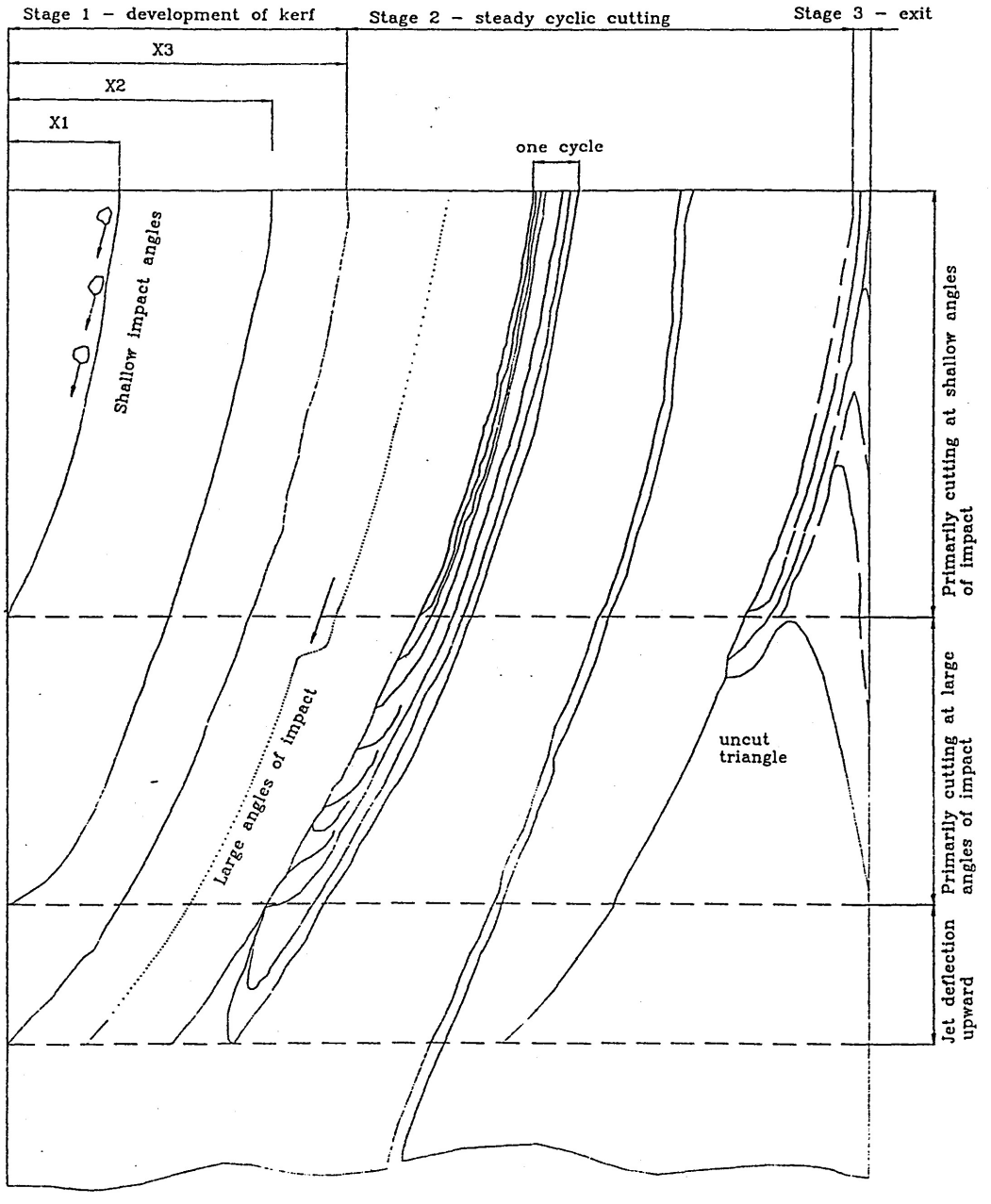

Figure 1.12 Visualisation of AWJ cutting [51]

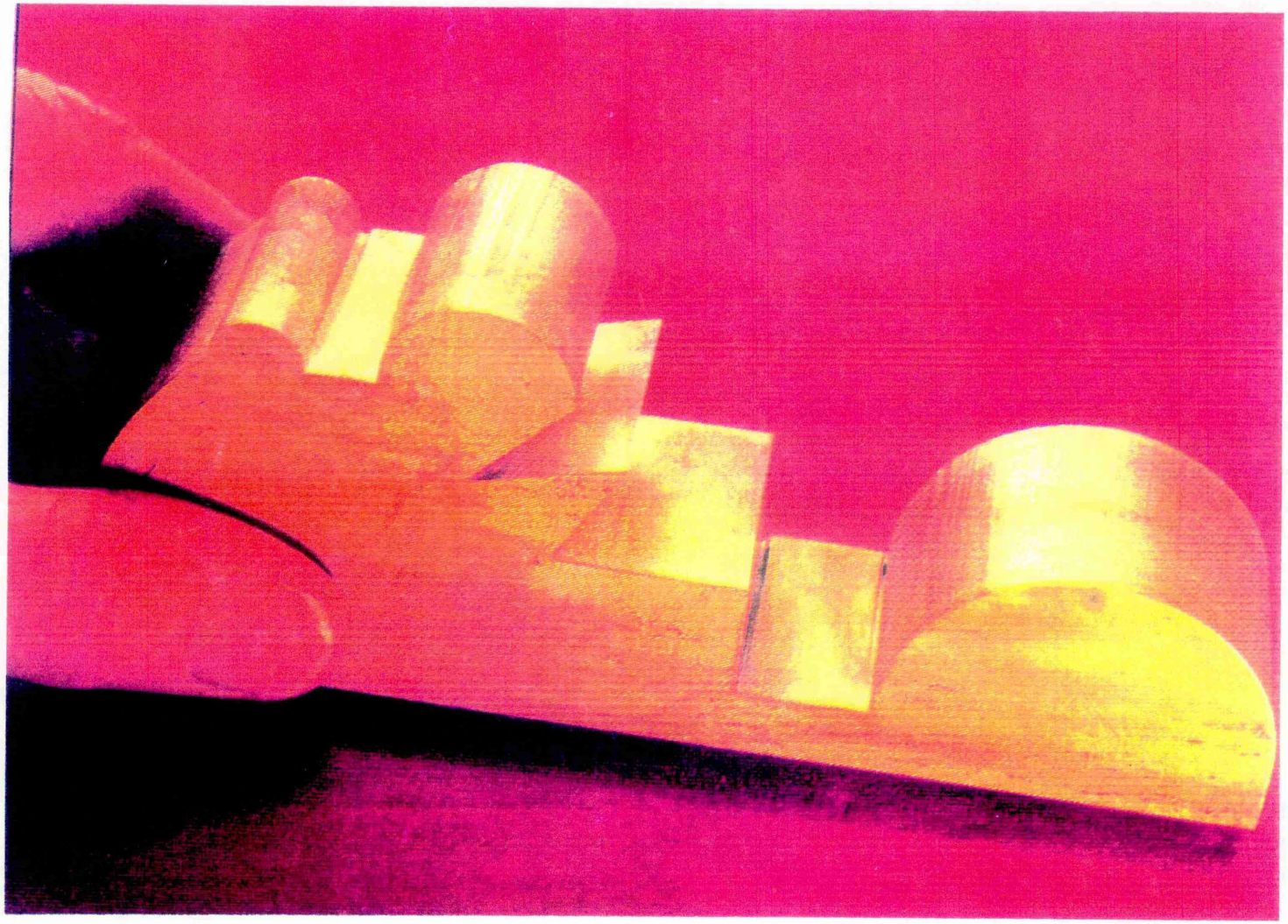

Figure 1.13 Brass sample cut by abrasive water jet

The other noticeable features of the cut surface are the surface roughness and the striations. The striations are predominant over the lower part of the surface whilst being barely noticeable in the upper part. The striations are quite regular, with their height increasing with increasing depth. Many attempts have been made to explain these variations in terms of system parameters, pressure or abrasive fluctuations [55, 56]. These striations occur with all power beam methods.

1.6 Optimisation of nozzle design

In suspension jet systems, the potential energy of the high pressure mixture is converted into the kinetic energy of a high velocity water jet. This jet is very complex in nature. However, a basic understanding of its characteristics can be gained from studying the development of a pure water jet.

1.6.1 The structure of a turbulent water jet

The water flow within the nozzle may be classified according to two distinct regions:

1) An inviscid core region where the effects of viscosity are negligible and radial velocity gradients are relatively small,

2) A boundary layer region adjacent to the wall within which the effects of fluid viscosity are confined. Within this region the velocity gradients are high, with the water velocity increasing from zero at the wall to 99% of the free-stream velocity.

In the presence of a strongly negative pressure gradient, associated with fluid acceleration in the contraction, the boundary layer thickness decreases. Careful design of the nozzle eliminates the possibility of unfavourable (positive) pressure gradients as this may lead to boundary layer separation at the nozzle inlet, or cavitation at the nozzle exit. In addition, the roughness of the wall must be such that individual roughness elements should be within the boundary layer or roughness-induced cavitation may occur.

Once outside the nozzle, the jet may continue to contract if the final nozzle contour is nonparallel and the diameter of the jet reaches a minimum before subsequent jet development. Turbulent mixing takes place between the jet fluid and the stationary fluid so as to equalise their velocities. Figure 1.14 shows the development of a turbulent jet, split into three main regions - the initial, transitional, and the main region.

The initial region is defined as the distance within which the centre-line pressure remains equal to the nozzle pressure. This region is characterised by an almost inviscid potential core moving at the exit velocity, surrounded by mixing layers [57].

The transition region is characterised by the propagation of the fine scale turbulent eddies on the surface of the jet. These disturbances are driven by a classical Helmholtz instability mechanism and are amplified and modified by the action of aerodynamic drag forces. The propagation of the surface waves leads to entrainment of the surrounding air or water.

As a result the jet dynamic pressure is reduced and the initial region reduced. When the wave amplitude approaches the local jet radius, entrained fluid reaches the jet centre-line and the jet breaks up into discrete 'packets' or slugs of flow. In the main region further development of these large scale structures occurs. Further aeration of the packets occurs due to secondary breakup of the jet. Atomization of the jet surface leads to the development of a region of fine droplets surrounding the broken core.

For a jet whose velocity is much less than the velocity of sound propagation, the pressure is substantially uniform throughout the jet and surrounding fluid. Thus the net force on the jet is zero and axial momentum is conserved.

Dimensional analysis suggests that the width of the jet increases linearly with the axial distance [58]. Consideration of the above yields a jet of circular cross section with a cetreline velocity decreasing inversely with x, the axial distance from the nozzle [59].

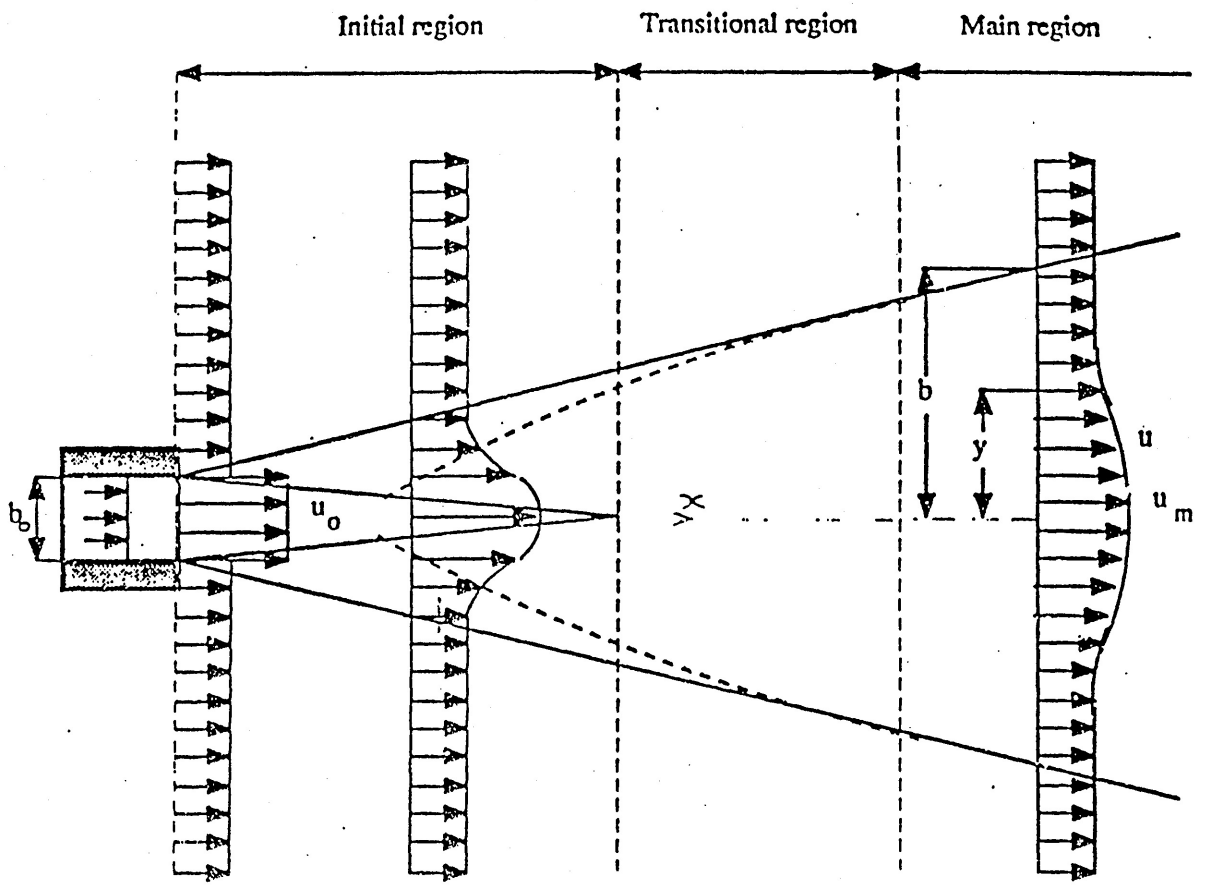

Figure 1.14 Development of a turbulent water jet [58]

The spread of the initial region is different from that in the main region [58]. The thickness of the spreading jet, b, is given by a square root relationship with a constant of proportionality of 0.237, i.e.

$$b = 0.237\sqrt{x}$$

The above observations are for water jets issuing into air. For submerged cutting, i.e. water jet into water, the relationships still hold although the constant of proportionality will differ. In this case the core potential vanishes quickly, after about one diameter [57].

Entrainment systems are composed of approximately 95% air, and this affects the spreading characteristics. Suspension jets, on the other hand, are purely water and abrasive, and their spreading is correspondingly less. However, smaller diameter and shorter parallel sections give rise to larger turbulent boundary layers, and spreading is increased, especially for velocities above the sonic velocity of the mixture.

1.6.2 Consideration of abrasive particle velocity - interphase momentum exchange

Models and experimental results of erosion and abrasive water jet cutting have shown the critical dependence of these areas on the particle velocity.

Existing work seemed to suggest that short parallel sections of standard DIAJET nozzles (~ 10 diameters) would allow the particles to achieve only 80% of the water velocity [8, 12]. If these models are valid then substantial improvements in cutting performance could be obtained by re-designing the nozzle including making it longer. In addition, the harsher conditions of the higher pressure DIAJET systems and the use of harder abrasives means that nozzle life is now a major factor in the economics of abrasive suspension jet cutting. If the nozzles could be made longer, and thus last longer, this alone would be worth the investigation, even if no further improvement in cutting performance was obtained.

The original form of the interphase momentum transfer was derived empirically in investigations of the flow around fixed bodies, and in the study of particulate settling [60].

Newton calculated the force on a sphere to be:

$$F_n = 0.22\pi a^2 \rho v^2$$

for small values of v, the relative velocity between fluid and particle, for which inertia effects are unimportant.

In 1850, Stokes also solved the equations of motion of fluid flow, again at low relative velocities [61]. For these conditions he also assumed that inertial effects can be omitted, yielding:

$$F_{St} = 6\pi a \mu v \qquad for\ Re < 1$$

C_D is the coefficient of drag for the body under consideration, defined as

$$C_D = Drag\ force\ /\ \pi a^2 \frac{1}{2} \rho v^2$$

It can be seen from the above equations that C_D [Stokes] = 24/Re and C_D [Newton] = 0.44Re a Reynolds number for the flow condition Re = Ua/υ.

Oseen [62] partially considers the inertial force, yielding a drag coefficient of

$$C_D = \frac{24}{Re}(1 + \frac{3}{16}Re)$$

At Re>10, separation of the boundary layer on the sphere occurs. The streamlines in the wake curl up to form a stationary vortex ring at the rear of the sphere. Further increases in Re lead to a growth of the vortex in size and strength. In a laminar stream at Re = 500 the vortex system separates from the body and a wake is formed. The vortex ring continues to form and shed from the sphere, producing an instantaneous wake drag force. At much higher Reynolds numbers, the value of C_D is assumed constant, with a value of about 0.1. Forces due to the displaced mass of water, and time dependent forces have an increasingly greater effect. It is no longer valid to just consider the drag force due to the relative velocity; the convective acceleration terms in Navier-Stokes equation are increasingly important.

A common approach to modelling this situation is to use a modified particle equation based on a more thorough analysis of the Navier-Stokes equation, yielding terms that accounts for the flow unsteadiness and other high acceleration phenomena.

Many people have presented solutions to this problem in the ensuing years. The generally accepted form of this equation of motion of a particle settling under gravity in a fluid otherwise at rest is [63]:

$$\frac{4\pi a^3}{3}\rho_p\dot{v} = -\frac{2\pi a^3}{3}\rho\dot{v} - 6\pi\mu a\left(v + \frac{a}{\sqrt{\pi\nu}}\int_{t_o}^{t} dt_1 \frac{\dot{v}(t_1)}{\sqrt{t-t_1}}\right) - \frac{4\pi a^3}{3}(\rho_p - \rho)g$$

The disturbance flow produced by the sphere is here assumed to be at a sufficiently low relative Reynolds number to solve the equation from the results of unsteady Stokes flow. In deriving this equation, the particle and fluid are assumed to be at rest at $t = t_0$. The term for apparent (or virtual) mass is here equal to one half of the mass of water displaced by the particle. This only strictly applies for spherical particles [641].

Tchen expanded the work of Basset, Boussinesq and Oseen to include the effects of a particle moving in a steady, non-uniform flow [63]. This was basically achieved by superpositioning a flow of velocity u on the system above, where the particle velocity v is now the relative velocity (v-u). By considering flow further into the past, the influence of the state of motion before t_0 will vanish. Therefore this integrand can be taken from $-\infty$.

The equation of motion for the particle is then given by:

$$\frac{4\pi a^3}{3}\rho_p\dot{v} = -\frac{4\pi a^3}{3}\rho\dot{u} - \frac{2\pi a^3}{3}\rho(\dot{v}-\dot{u}) - 6\pi\mu a\left((v-u) + \frac{a}{\sqrt{\pi\nu}}\int_{-\infty}^{t} dt_1 \frac{\dot{v}(t_1)-\dot{u}(t_1)}{\sqrt{t-t_1}}\right) - \frac{4\pi a^3}{3}(\rho_p - \rho)g$$

Corrections to this model have been proposed over the years [65]. In particular, the method of superposition yields incomplete terms for the undisturbed flow field and the pressure gradient force.

The majority of models applied to the analysis of acceleration in abrasive water jet systems are less complex than those given above. Guo et al., section 2.3.3, modelled the acceleration process considering only drag and virtual mass forces. They found that, while the water is accelerated in the convergent section of the nozzle, the majority of the particle acceleration occurred in the parallel section. Similar results were obtained by the other papers reviewed in section 2.3. The particle velocity at nozzle exit is quoted as being only 80% of the theoretical maximum water velocity, suggesting improvements in nozzle design could be significant. A proper investigation of particle acceleration was necessary therefore, not just to obtain a velocity for use in the cutting model, but also to seek design improvements.

Experimentally, the particle velocity is quite difficult to measure. Laser Doppler anemometry was unsuccessfully tried during the course of this project (see chapter 5). The only real validation of the model of particle velocity is achieved by the goodness of fit of the cutting model when using the predicted values of velocity, and indications from averaged values during system calibration.

1.7 Characterisation of abrasive particles

The three most important characteristics of an abrasive particle are its size, material/composition, and shape. The particle material determines its mechanical properties such as density and hardness, and usually its shape also. This section discusses the characteristics of abrasive particles influential in the erosion process.

1.7.1 Particle size

The particle size is important in that it affects properties such as the surface per unit volume and the settling velocity of the particle, thus affecting the velocity of the particle and the required transport velocity respectively. Though the models are developed for one idealised particle size and shape, one needs to know the distribution of particle sizes in a mixture and to define a mean size that in some way represents the behaviour of the particulate mass as a whole. Important operations relating to systems of particles include storage in hoppers, flow through orifices and pipes, and metering of flow. Table 1.1 gives a sample measured particle distribution for Olivine AFS 80, used in this study.

Mesh	mm	Amount retained by sieves, %
60	0.250	1
80	0.177	34
120	0.125	49
170	0.088	12
230	0.063	3
Pan	<0.063	max 1
Average grain size, mm		0.18
AFS number		88
Tolerances		± 10%

Table 1.1 Particle size distribution of Olivine AFS 80

1.7.2 Abrasive material properties

Table 1.2 lists the properties of some commonly used abrasive materials in AWJ cutting.

	Garnet	Olivine	Zircon
Composition	Al_2O_3: 20.35 % MgO: 12.35% CaO: 2.95% FeO: 9.70% Fe_2O_3: 12.50% MnO: 0.85% SiO_2: 41.30%	MgO: 49.50% SiO_2: 42.50% Fe_2O_3: 7.00% Cr_2O_3: 0.20% Al_2O_3: 0.45% NiO: 0.30% MnO: 0.03% CaO: 0.02%	ZrO_2: 66.50 % SiO_2: 32.50% Al_2O_3: 0.30% TiO_2: 0.10% Fe_2O_3: 0.06%
Bulk density g/cm^3	3.9 to 4.9	1.7 to 1.9	4.6
Hardness (Mohs)	8.3	6.5 to 7.5	7.5
Specific gravity	4.3	3.3	5.2
Grain shape	sub-angular	angular	angular
Roundness	.57	.4	.35
Sphericity	.75	.75	.75
Colour	pale green	red	white

Table 1.2 Abrasive properties

1.7.3 Particle shape

The particle of simplest shape is a sphere, in that because of its symmetry, the question of orientation does not have to be considered. No other particle has this characteristic. Frequently, the size of a particle of irregular shape is defined in terms of the size for an equivalent sphere. However, the particle is represented by a sphere of different size according to the property selected, for example the sphere with the same settling velocity or with the same volume as the particle.

1.7.3.1 Sphericity

A measure of particle shape that is frequently used is the sphericity, S, defined by the relation:

$$S = \sqrt[3]{\frac{volume\ \ of\ particle}{volume\ \ of\ circumscribing\ \ sphere}}$$

Greater details on sphericity classification and measurements can be found in Coulson and Richardson [66]. The above equation can be expressed as $S = \frac{d_e}{d_p}$ where d_e = equivalent diameter, which is defined as 3 6v/r where v is the actual particle volume, d_p = the diameter of the circumscribing sphere, which is the maximum intercept through the particle.

1.7.3.2 Roundness

The roundness, R_f, is defined as $R_f = \frac{average\ diameter\ of\ corners\ and\ edges}{diameter\ of\ maximum\ inscribed\ circle}$. When the corners are sharp, their average diameter will be small and the roundness will be small. Spherical particles have a roundness of 1. Figure 1.15 is a combined roundness and sphericity chart applicable for sand grains [67].

1.7.4 Measurement techniques

A wide range of techniques is available, both for single particles and for systems of particles. The following are methods applicable to the size range of particles generally encountered in abrasive water jetting.

1.7.4.1 Sieving

Sieve analysis is carried out using a nest of sieves, each lower sieve being of smaller aperture size. The sieve sets are selected with a constant ratio of aperture sizes. The sieves are mounted on a vibrator. The sieving is based purely on the linear dimensions of a particle and whether or nor that particle will pass through an aperture depends not only upon its size, but on the probability that it will be presented at the required orientation.

1.7.4.2 Microscopic analysis

Microscopic analysis allows measurement of the projected area of the particle and enables an assessment to be made of its two-dimensional shape. The shape of the particle is then compared to a standard chart to estimate the sphericity and roundness, figure 1.15. Scanning electron microscopy also allows analysis of the structure of the individual particles. This can detect flaws in the particles. Such techniques have been used here to compare particles before and after passing through the nozzle and material, also to examine the cut surface for embedded particles.

1.7.4.3 Light and sound scattering methods.

These methods depend on the wave scattering by particles in a direction at right angles to the incident beam. The fraction of the incident light scattered is directly proportional to the concentration of the particles and to the cube of their diameter. Similar techniques based on reflection rather than scattering may also be used.

1.7.4.4 Systems of particles

1.7.4.4.1 Particle size distribution

Most particulate systems of practical interest consist of particles of a wide range of sizes and it is necessary to be able to give a quantitative indication of the mean size and of the spread of sizes. The results of a size analysis can be most conveniently represented by means of a cumulative weight fraction curve, in which the proportion of particles (x) smaller than a certain size (d) are plotted against that size.

In most practical determinations of particle size, the size analysis will be obtained as a series of steps, each step representing the proportion of particles lying within a certain range of size. From these results a cumulative size distribution can be built up and this can then be approximated by a smooth curve if the size intervals are sufficiently small. A typical curve for a size distribution on a cumulative basis is shown in figure 1.16. This curve rises from zero to unity over the range from the smallest to the largest particle size present.

The distribution of particle sizes can be seen most readily by plotting a size frequency curve also shown in figure 1.16, in which the slope of the cumulative curve is plotted against particle size. The most frequently occurring size is thus shown by the maximum of the curve. For naturally occurring materials, the curve will generally have only one peak. However particles formed by crushing larger particles may show two peaks, one characteristic of the material and the other characteristic of the crushing equipment.

1.7.4.5 Mean particle size

It is often desirable to express the size of a system of particles in terms of one number. This has been chosen as the size of the opening through which a certain percentage of the material will pass [68]. For example, the size d_{50} is the size of the opening through which 50% of the material will pass. The size d_{80} is a useful rough comparative measure for the size of material that has been through a crusher.

This mean particle size could be based on weight, surface area, linear dimensions and so it is important to know which geometric mean is relevant to the discussion.

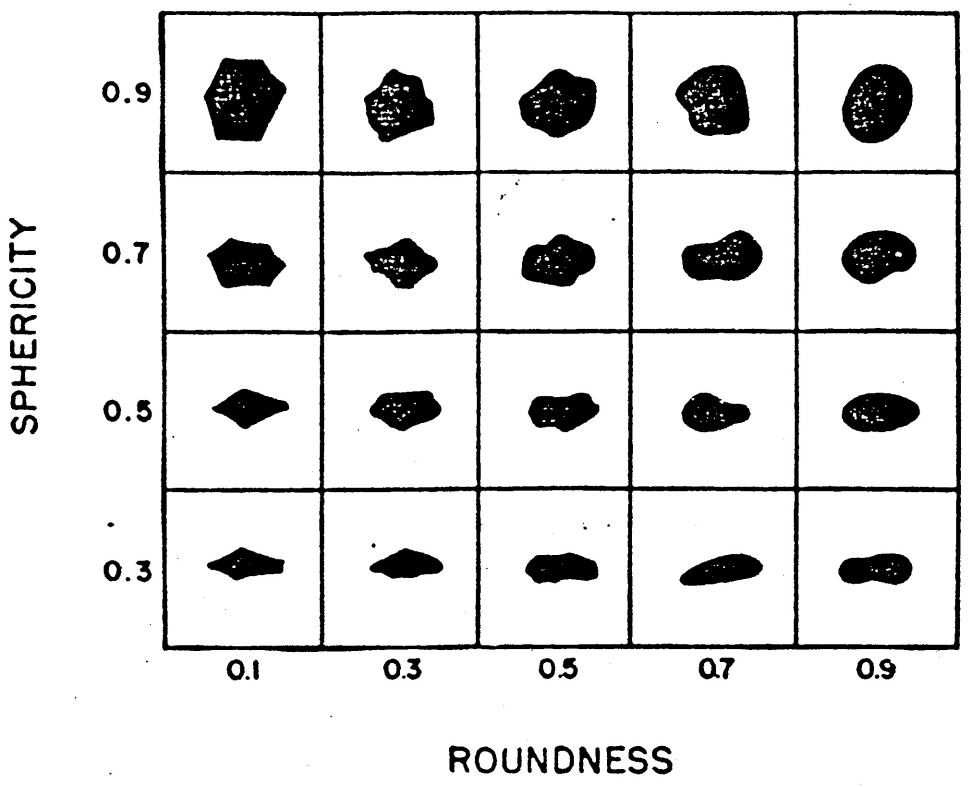

Figure 1.15 Combined roundness and Sphericity chart [67]

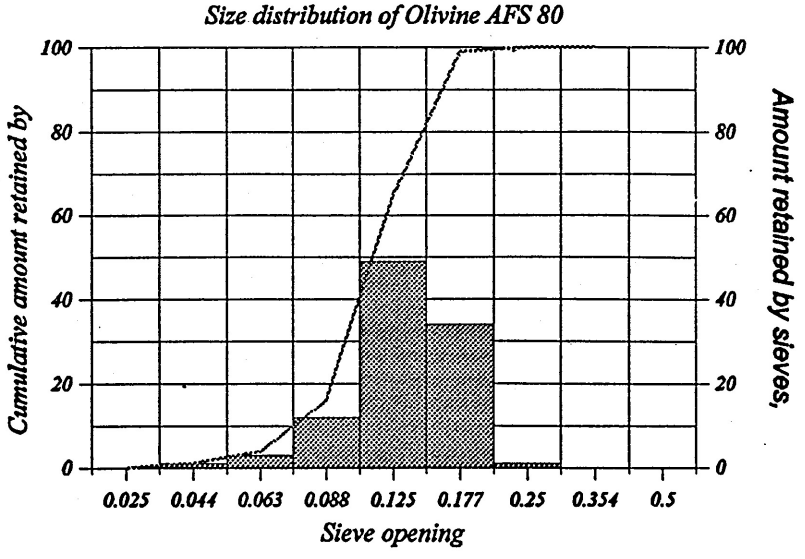

Figure 1.16 Size distribution of olivine AFS 80

CHAPTER 2 - REVIEW OF RELEVANT MODELS DEVELOPED BY PREVIOUS WORKERS

2.1 Solid particle erosion model

The previous section shows that the nature of particulate erosion is too complex to expect that complete analytical models could be developed. However, significant contributions made in this field have yielded empirical models that can be used to predict approximately erosion results. The most common approach in developing such models is to use the single particle impact process. The volume removed by multiple particle impacts is then calculated by adding volumes removed by single particles corrected by an experimental factor.

However, the fact that the geometry and possibly mechanical features of the surface will change as the multiple impact erosion proceeds may handicap this approach. Alternative approaches, such as data curve fitting or global energy balance analyses, have proven no more successful in explaining the physics of the erosion phenomena.

This section reviews the significant efforts made to model the erosion process by solid particle impact for both ductile and brittle material. This distinction, however, may not be adequate for the erosion process. For example, Sheldon and Finnie noticed that under certain erosion conditions a nominally brittle material, such as glass, may exhibit an erosion characteristic similar to that of ductile aluminium [45]. A material that shows a peak of erosion at relatively shallow angles of impact is ductile, as has been observed for steel, aluminium, copper. Materials that show maximum erosion at normal impact angles, such as alumina or glass, are brittle. Again, this criterion of classification is not accurate, as the erosion of a "ductile" material can exhibit both ductile and brittle behaviour.

2.1.1 Finnie's Model

Finnie proposed one of the first models of erosive wear in 1958, and has reported continuous refinements since [2, 23, 49, 69-71]. He likened erosion to the action of an individual tooth on a grinding wheel. The model developed is therefore similar to that of machining by a single point tool. Figure 2.1 shows a particle moving at a velocity v that

raises a lip in front of it as it proceeds in its cutting trajectory. The particle is assumed rigid and doesn't fracture during cutting. The cutting tip has the coordinates (x_t,y_t), through which the material reaction forces are assumed to act. The particle's centre of gravity has coordinates (x,y).

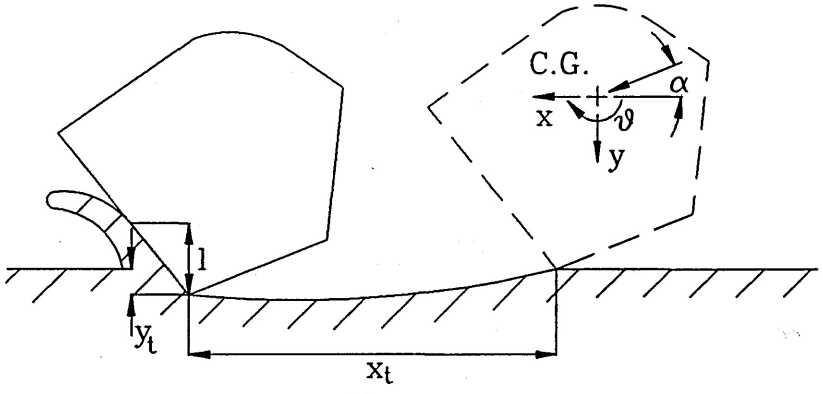

Figure 2.1

The ratio of the horizontal to vertical reaction force R_x/R_y is assumed constant, equal to k; this assumes negligible particle rotation throughout the cutting process. i.e. $\theta = 0$. Finnie found experimentally that $\theta<18°$, thus justifying this assumption. Furthermore, the ratio of the length of cut (l) to the depth of cut (y_t) is assumed constant, equal to ψ. This value, calculated from grinding studies, is approximately 2 [23].

From the assumption of negligible rotation, the relationships between the two sets of coordinates are approximately:

$$x_t \approx x + r\,\theta$$

$$y_t \approx y$$

Finnie neglects elastic forces and assumes a constant plastic stress during cutting, of magnitude σ in the horizontal direction.

For a uniform width b, the reaction forces acting on the particle are:

$$m\ddot{x} = -\sigma l b = -\sigma\psi y b \qquad 2.1$$

$$m\ddot{y} = km\ddot{x} = -k\sigma\psi y b \qquad 2.2$$

$$I\ddot{\theta} = r(m\ddot{x}) = -r\sigma\psi y b \qquad 2.3$$

Initially $x = v\cos\alpha$, $y = v\sin\alpha$, $\theta = \theta_0$ and $x = y = \theta = 0$.

Noting equation 2.2 is the equation for simple harmonic motion we can solve this, and substitute into the other equations to get:

$$x = \frac{v\sin\alpha}{\beta k}\sin\beta t + \left(v\cos\alpha - v\frac{\sin\alpha}{k}\right)t \qquad 2.4$$

$$y_t = y = v\frac{\sin\alpha}{\beta}\sin\beta t \qquad 2.5$$

$$\theta = \frac{mrv\sin\alpha}{\beta k}(\sin\beta t - \beta t) + \dot{\theta}_o t \qquad 2.6$$

where

$$\beta = \left[\frac{\sigma\psi bk}{m}\right]^{0.5}$$

The total volume removed by the particle is calculated from:

$$V = \int_0^{t_c} b y_t dx_t = \int_0^{t_c} b y \frac{d(x + r\theta)}{dt} dt$$

where t_c is the length of time the particle is in contact with the material.

The solution of this integral is [69]:

$$V = \frac{mv^2\left(\cos^2\alpha - \left(\frac{\dot{x}_t'}{u}\right)^2\right)}{4\sigma\left(1+\frac{mr^2}{I}\right)}$$

where x_t' is the horizontal velocity of the tip at time t_c.

To determine t_c we can distinguish between two different ways for the particle to stop cutting. At low angles of impact, the particle 'skims' the surface and cutting stops when the particle leaves the material, i.e. when $y_t = 0$. At higher α, cutting will cease when the particle stops travelling in the direction of cut, i.e. $dx_t/dt = 0$.

It can be shown [2] that for low alpha,

$$\dot{x}_t' = v\cos\alpha - \frac{2v}{P}\sin\alpha$$

where $P = \frac{k}{\left(1+\frac{mr^2}{I}\right)}$, I being the moment of inertia of the particle.

This only applies for $\tan\alpha < \frac{P}{2}$, after which x_t' as given above will be negative.

Thus the eroded volume is given by:

$$V = \frac{mv^2}{4\sigma\left(1+\frac{mr^2}{I}\right)}\frac{2}{P}\left[\sin 2\alpha - \frac{2}{P}\sin^2\alpha\right] \qquad \tan\alpha \le \frac{P}{2} \qquad 2.7$$

$$V = \frac{mv^2}{4\sigma\left(1+\frac{mr^2}{I}\right)}\cos^2\alpha \qquad \tan\alpha \ge \frac{P}{2} \qquad 2.8$$

From the differential of equation 2.7, the maximum erosion will take place at $\tan 2\alpha = P$.

Practical abrasive grains will have a moment of inertia between $I = \frac{1}{2}mr^2$ and $\frac{1}{3}mr^2$ [70], thus P will be between 0.5 and 0.66 and the maximum erosion occurs at between 13 and 16° and the transition will occur at between 14° and 18.5°.

Figure 2.2 shows this prediction (dashed line). Note the prediction of zero volume removal at impact angles close to normal. Possible reasons given for this are:

- Once cutting has begun, the particles strike a roughened surface at varying angles and thus normal impacts never occur.
- Multiple impacts on the surface cause low-cycle fatigue fractures.

Finnie attempts to include the effects of particle rotation in the model. Although impossible to measure the initial rotation of the particles, Finnie assumes an Omega distribution of initial rotations θ_0 [69]. Replacing $v\cos\alpha$ with $v\cos\alpha \pm \theta_0 r$ yields an erosion versus angle characteristic with some erosion at 90°.

Replacing m, the mass of a particle, with M the mass flow of the abrasive, and including the above observations and c for the fraction of particles cutting in this idealised manner we get

$$V = \frac{cMv^2}{16\sigma}\cos^2\alpha \qquad \alpha \geq 14$$

$$V = \frac{cMv^2}{4\sigma}[\sin 2\alpha - 4\sin^2\alpha] \qquad \alpha \leq 14$$

For angles close to the maximum erosion (15° to 20°):

$$V \approx 0.075\left(\frac{MV^2}{2}\right)p$$

i.e. the erosion is proportional to the kinetic energy of the particle. This is at odds with experimental findings, which exhibits a velocity exponent between 2.3 and 2.5.

To rectify this shortcoming, Finnie and McFadden [71] placed the reaction forces at the centre of the contact path of the particle instead of at the tip as in the previous analysis.

This modifies equation 2.6, angular rotation, to:

$$I\ddot{\theta} = (r-y)m\ddot{x}-2ym\ddot{y} \\ = -\sigma\psi by(r-y)+2(k\sigma\psi yb)y \qquad 2.9$$

Assuming, as before, the initial values of $\theta=\theta_0=0$ and putting $I = \frac{1}{3} mr^2$, we get

$$\theta = \frac{15v^2\sin^2\alpha}{16\beta^2r^2}(2(\beta t)^2+\cos 2\beta t-1)+\frac{3v\sin\alpha}{2r\beta}(\sin\beta t-\beta t)$$

Case 1, above, for low angles of impact with the particle leaving the material is given by $t_c = n\pi/\beta$. Integrating over this period yields:

$$V = \frac{mv^2}{\sigma\psi k}(\sin 2\alpha-4\sin^2\alpha)+\frac{15\pi b}{4r}\left(\frac{v\sin\alpha}{\beta}\right)^3$$

For large angles of impact, t_c must be determined numerically for a given α and then the volume calculated.

The following table 2.1 shows the exponent as a function of λ, the penetration depth to particle diameter ratio, and V_2/V_1, the ratio of particle velocities. This now predicts a velocity exponent of greater than two, rising with the angle of attack, as has been observed experimentally. The modified erosion rate vs. angle of attack is shown on figure 2.2 (solid line).

Table 2.1 : The velocity exponent n [71]

λ	V_2/V_1	$\alpha = 11$	$\alpha=15$	α 18
0.125	2	2.25	2.38	2.49
	1.75	2.24	2.36	2.46
	1.5	2.22	2.34	2.44
0.100	2	2.21	2.33	2.42
	1.75	2.20	2.31	2.40
	1.5	2.19	2.29	2.37
0.075	2	2.17	2.27	2.37
	1.75	2.16	2.25	2.35
	1.5	2.15	2.24	2.34

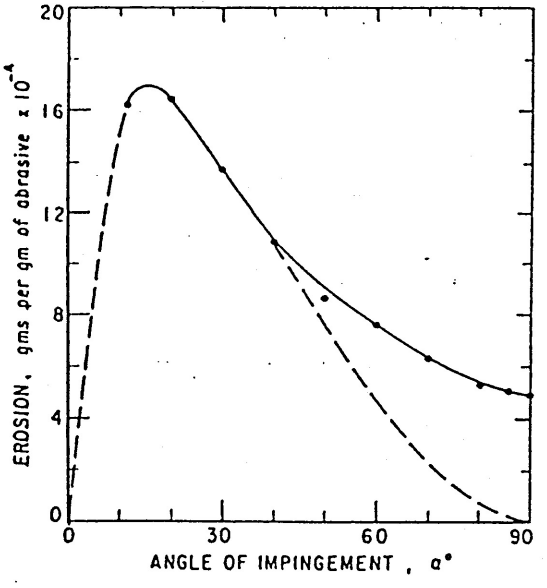

Figure 2.2 Erosive wear versus angle of attack

2.1.2 Bitter's model

Bitter employed energy balance techniques to develop models which distinguished between two different mechanisms of erosive wear, depending on the angle of impact [1]. This was prompted by observations that two types of erosive wear could be distinguished [19-20].

The basis of the deformation wear mode is strain-hardening of the surface due to repeated deformations of near normal impacts, causing fragments to be subsequently removed by fracture. Cutting wear, on the other hand, is brought about by shallow angle impacts exceeding the shear strength of the material. As such, the model is applicable to both ductile and brittle classes of materials.

(a) Deformation wear.

The approach taken was to model the particle hitting the surface as a sphere impacting on a flat surface (infinitely large radius sphere). The forces were calculated from studies by Hertz [72], the relevant details of which are reported in appendix A. Figure 2.3 depicts a (spherical) particle impacting onto a surface.

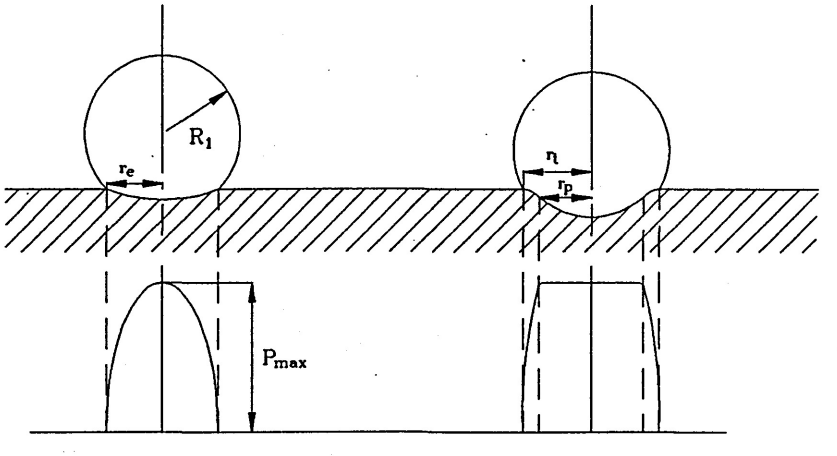

Figure 2.3

Let V be the initial velocity of the particle. The energy balance of the collision is:

$$\frac{mV^2}{2} = Q_e + Q_{pe} + Q_p \qquad 2.10$$

Q_e and Q_{pe} are the elastic energy absorbed in the regions of elastic and elastic-plastic deformation respectively, and Q_p is the total energy expended in forming the permanent indentation.

According to Hertz, the velocity required to just cause plastic deformation ($\sigma_{max} = \sigma_y$) is given by:

$$V_{el} = \frac{\pi^2}{2\sqrt{10}} \frac{\sigma_y^{2.5}}{\rho_p^{0.5}} \left[\frac{1-\nu_1^2}{E_1} + \frac{1-\nu_2^2}{E_2} \right]^2 \qquad 2.11$$

For the case of plastic deformation, the elastic energy absorbed outside the area of permanent deformation can be shown to be a constant, equal to that required to just cause plastic deformation. Thus, the elastic energy absorbed in the elastic region is:

$$Q_e = \frac{1}{2} m V_{el}^2$$

The potential energy of the elastic deformation in the area subjected to a plastic-elastic load is:

$$Q_{pe} = \frac{1}{2} h_{el} \sigma_y \pi r_p^2$$

where $h_{el} = \frac{\pi^2}{4} \sigma_y^2 r \left[\frac{1-\nu_1^2}{E_1} + \frac{1-\nu_2^2}{E_2} \right]^2$ is the depth of the indentation for the just-plastic condition.

The formation of the permanent indentation requires an amount of energy equal to:

$$Q_p = \int_0^{H_{max}} \pi r_p^2 \sigma_y dH \approx \pi r H_{max}^2 \sigma_y$$

where H_{max} is the depth of the indentation after collision. As $r^2_{pmax} = 2RH_{max}$ we can write

$$Q_{pe} = \sqrt{\frac{15}{4} Q_e Q_p}$$

Substituting into our total energy equation, 2.10, re-arranging and neglecting second order terms gives: $Q_p \approx \left[\sqrt{Q}-\sqrt{Q_e}\right]^2$ i.e.

$$Q_p \approx \frac{1}{2}m\,[V-V_{el}]^2$$

If we define ϵ as the energy needed to remove one unit volume of material by normal impact then for particles with velocity magnitude v impacting at an angle of α the erosion rate is:

$$W_D = \frac{\frac{1}{2}M\,[v\sin\alpha-V_{el}]^2}{\epsilon} \qquad 2.12$$

If $V\sin\alpha < V_{el}$ no erosion occurs, as the particle just rebounds without causing permanent deformation.

For sharp edged particles the apparent density will be large, resulting in small V_e values. V_e is seen to be strongly related to the yield strength and thus the hardness. Therefore this model, which assumed constant yield strength, applies from the point where the erosion process has become stationary.

A highly deformed surface layer has then been formed on the body, with an almost constant value of σ_{ult} [73]. Cracks form within the deformed layer once this maximum value has been reached, and a flake is removed from the surface. The exposed surface is already highly deformed, and the process continues. Hence the value of yield strength is actually the ultimate strength. Further found that plastic deformation sets in if the pressure on the surface is 1.06 the ultimate yield strength [74].

(b) Cutting wear model

The cutting wear model corresponds to the particles striking the body at an acute angle, scratching out some material from the surface. Two distinct conditions could cause the particle to stop cutting, namely:

(a) the particle exits with a component of horizontal velocity after cutting, and
(b) the horizontal velocity component becomes zero during the collision.

Case (a): The particle still has a horizontal velocity component as it exits the material,

$$\dot{x} \neq 0$$

Let the energy required to scratch out a unit volume of material be ζ (assuming the particles are not destroyed). Thus the volume cut from the body by one particle is:

$$W_{cl} = \frac{\frac{1}{2}m\,(X_0^2 - X_1^2)}{\zeta}$$

To calculate x_1, the exit velocity, Bitter considered a plastic-elastic collision at an acute angle assuming the particle to be spherical. This is validated by noting a particle will only penetrate the material to a depth of about one-tenth its radius, i.e. only the rounded tip of a non-spherical particle penetrates into the surface. Thus the particle is modelled as a sphere with radius equal to the radius of curvature, r, and density $(R/r)^3$ that of the actual density for a particle volume equal to $4/3\ \pi\ r^3$ (as shown in figure 2.4 below):

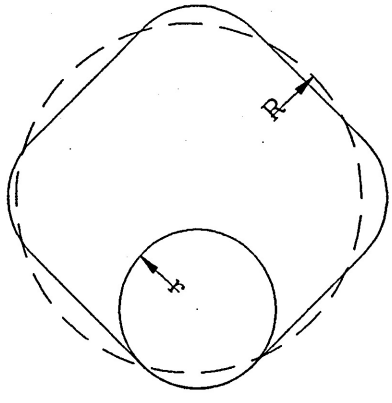

Figure 2.4

Assuming the area of contact, A, is subjected to the shear load ζ, the energy equation can be written as:

$$A\zeta = -m\frac{d\dot{x}}{dt} \qquad 2.13$$

Since the depth of penetration is small in relation to the particle diameter we can say

$$A \approx \frac{4}{3} r_p H = \frac{4}{3}\sqrt{2R}H^{\frac{3}{2}}$$

where H has the same significance as the deformation wear model above.

Substituting this into equation 2.13 and integrating gives

$$\dot{x}_0 - \dot{x}_1 = \frac{4\sqrt{2R}}{3m}\zeta\int H^{\frac{3}{2}}dt \qquad 2.14$$

Bitter comments that Finnie [23] has shown that any rotation (for example imparted due to friction) is negligible.

The particle's motion can be split into two parts, the first period ending when the particle's vertical component of velocity is zero and the second period when the particle is pressed back out of the material by the elastic reaction forces set up in both particle and material during the collision.

The first part of the first period is purely plastic and no erosion occurs. For the duration of the second part of the first period, the elastic-plastic collision, Bitter uses equations derived by Andrews [75-76]:

$$t_1 - t_0 = (\frac{\pi}{2} + \delta)\sqrt{\frac{m}{\pi R \sigma_y}} \qquad 2.15$$

in which δ is a correction for the elastic deformation.

Bitter ignores this small term to obtain the equation for a purely elastic collision as

$$t_1 - t_0 = \frac{\pi}{2n} \quad \text{where} \quad n = \sqrt{\frac{\pi R y}{m}} \ .$$

The penetration depth is given by:

$$H = H_{max} \sin [n(t-t_o)]$$

Substitution into 2.14 and graphical integration gives:

$$V_{t0} - V_{t1} = \frac{0.873 \frac{4}{3} \sqrt{2R}\, H_{max}^{\frac{3}{2}} \zeta}{n m}$$

where V_{t1} is the parallel velocity component at the end of the first period.

During the second period the particle continues its cutting action. The elastic reaction forces, however, press the particle out of the surface and decreases the penetration depth, as in the deformation wear above, to:

$$\Phi_{max} = H_{max} + h_{el} \qquad 2.16$$

The total force on the contact area during the first part of the second period (see deformation wear) then yields an equation of motion of:

$m \frac{dV}{dt} = \pi r_p^2 y + \frac{2}{3} \pi r_e^2 y$ from which follows

$$\frac{dV}{dt} = \frac{2\pi R y H}{m} + \frac{4\pi R y h_{el}}{3m} \qquad 2.17$$

Since during the first part of the second period H decreases to zero, h_{el} remaining constant, we may put $V = -\frac{dH}{dt}$.

Multiplication of the above two equations yields

$$\frac{dx}{dt} = n\sqrt{2}\sqrt{\left(H_{max}^2 - H^2\right) + \frac{4}{3}h_{el}(H_{max} - H)}$$

The decrease of the horizontal velocity component during the second period can then be written as:

$$\dot{x}(t_1) - \dot{x}(t_2) = \frac{4}{3}\frac{\sqrt{RH_{max}^2}}{m}\frac{\zeta}{n}\int \frac{x^{\frac{3}{2}}dx}{\sqrt{1 - x^2 + \frac{4}{3}\frac{h_{el}}{H_{max}}(1-x)}}$$

The total decrease of horizontal velocity during the collision is then given by:

$$\frac{d\dot{x}(t_0)}{dt} - \frac{d\dot{x}(t_2)}{dt} = \frac{4\sqrt{2R}H_{max}^{\frac{3}{2}}\rho}{3nm}[0.873 + \frac{1}{2}\sqrt{2}f(x)]$$

where f(x) is the result of the integral given in equation 2.18.

By substituting in for the variables, and using the assumption that $\frac{V\sin\alpha}{V_e} > 1.5$, the energy expended by the particle in scratching the material is given by:

$$W_{cl} = 2M\frac{C(V\sin\alpha - V_e)^2}{\sqrt{V\sin\alpha}}\left[V\cos\alpha - \frac{C(V\sin\alpha - V_e)^2}{\sqrt{V\sin\alpha}}\zeta\right]$$

Case (2): cutting wear equation when $\dot{x}_2 = 0$

The horizontal velocity component may become zero during the first period, during the second period or in the boundary case at the end of the first period. For this last case, the particle retardation is given by:

$$\frac{\tau A}{m} = \frac{\frac{4}{3}\sqrt{2R}H^{\frac{3}{2}}\tau}{m}$$

where τ, the material stress, has a maximum value of the elastic yield stress, σ_y. Since H, the indentation depth, has a maximum of R/10, the maximum retarding force in the horizontal direction is given by:

$$\frac{\frac{4}{3}\sqrt{0.002}RH^2\sigma_y}{m}$$

From equation 2.15, the vertical retardation is at least:

$$|a_\perp| > \frac{0.2\pi R^2\sigma_y}{m}$$

Thus the ratio of the retardations is $\frac{a_1}{a_\perp} < 0.094$. Since, in the case being considered, both components of velocity become zero at the same time (in the end of the first period), $\frac{V_1}{V_\perp} = \frac{V\cos\alpha}{V\sin\alpha} = \cot\alpha < 0.094$. Thus $\alpha > 84.5°$, i.e. only near-normal impacts will halt a particle.

If the horizontal motion becomes zero exactly at the end elastic first part of the first period, the energy absorbed in just causing yield to the depth h_{el} would be $\frac{2}{3}\sqrt{2R}H_{max}^{\frac{3}{2}}h_{el}\sigma_y$.

Elimination of h_{el} and H produces:

$$\frac{1}{2}V^2{}_1(t_2) = \frac{1}{2}m\left[0.82\sigma_y^2\sqrt{\frac{\sigma_y}{d}\left(\frac{1-q_1^2}{E_1}+\frac{1-q_2^2}{E_2}\right)^2}\right]^h[V\sin\alpha - V_e]^{\frac{3}{2}}$$

If the horizontal velocity of the particle should become zero sooner (in the first period) or later (in the second period) the area subject to shear and hence its elastic energy would be smaller.

Therefore: $\frac{1}{2}mV_{el}[V\sin\alpha - V_e]^{\frac{3}{2}} \geq \frac{1}{2}mV_1^2(t_2) \geq 0$ where $V_{el} = 0.82\sigma_y^2\sqrt{\frac{\sigma_y}{d}\left(\frac{1-q_1^2}{E_1}+\frac{1-q_2^2}{E_2}\right)^2}^h$

The energy absobed by the cutting wear equals $\frac{1}{2}m(V^2\cos^2\alpha - V_1^2(t_2))$.

Therefore we can write:

$$\frac{1}{2}mV^2\cos^2\alpha \geq \frac{1}{2}m(V^2\cos^2\alpha - V_1^2(t_2))$$

$$\geq \frac{1}{2}m\left[V^2\cos^2\alpha - V_{el}(V\sin\alpha - V_e)^{\frac{3}{2}}\right]$$

Bitter calculates the cutting wear based on the last term in the above equation. For a mass M of particles, the cutting wear per unit volume is given by:

$$W_{C2} = \frac{\frac{1}{2}m\left[V^2\cos^2\alpha - V_{el}(V\sin\alpha - V_e)^{\frac{3}{2}}\right]}{\rho} \qquad 2.19$$

These wear modes are graphically shown in figure 2.5.

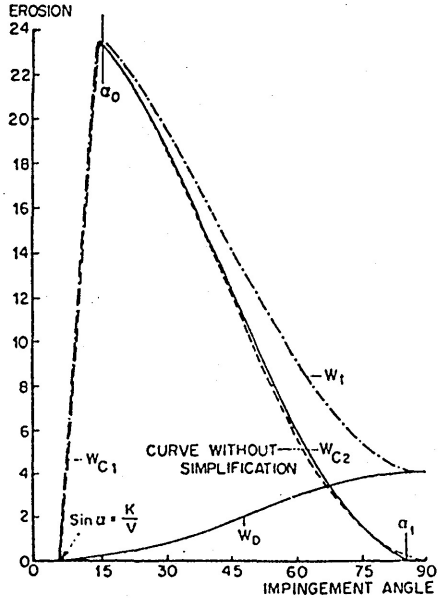

Erosion of a soft and ductile material.

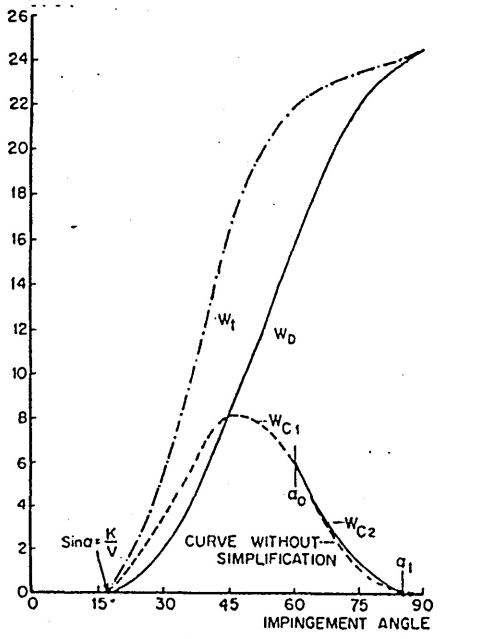

Erosion of a hard and brittle material.

Figure 2.5 [1]

2.1.3 Neilson and Gilchrist

Neilson and Gilchrist developed a simpler analytical model based on the findings of Bitter and their own experimental observations [77].

From tests they confirmed a model of erosive wear should include:

(i) The normal component of the kinetic energy of the impacted particles is absorbed in the specimen surface and accounts for deformation wear.

(ii) For certain hard materials, subject principally to deformation wear, there is a limiting component of velocity normal to the surface below which no erosion takes place. This limiting value is dependent on particle shape.

(iii) The kinetic energy component parallel to the surface is associated with cutting wear.

(iv) For cutting wear and large angles of attack the particles come to rest in the surface and the total parallel component of the kinetic energy contributes to the cutting wear. For small angles of attack, however, the particles may sweep into the surface and finally leave again with a residual amount of kinetic energy.

The maximum erosion occurs at approximately 20° for ductile materials. This angle is independent of the type of abrasive or the particle velocity and is, in fact, a material constant. More brittle materials have maximum erosion at larger angles of impact. The damage (erosion rate) increases with increasing particle velocity, and with decreasing particle size. The tests also show an initial gain in material mass, due to embedded abrasive particles, until the critical velocity is reached. The erosion mechanisms identified were surface cracking with subsequent intersection for brittle material (Glass), and cutting wear for ductile material (Aluminium).

Denoting the amount of kinetic energy required to remove a unit mass of material for cutting and deformation wear as ϕ and ϵ respectively, the above comments suggest the following model:

$$W = \frac{M(V^2\cos\alpha^2 - v_p)}{2\phi} + \frac{M(V^2\sin\alpha - V_e)}{2\epsilon} \qquad \alpha < \alpha_o \qquad 2.20$$

$$W = \frac{MV^2\cos\alpha^2}{2\phi} + \frac{M(V\sin\alpha - V_e)}{2\epsilon} \qquad \alpha > \alpha_o \qquad 2.21$$

where W is the erosion due to a mass M of particles at an angle of attack α and a particle velocity of V. V_e is the normal component of velocity below which no erosion takes place, and v_p is the residual parallel component of particle velocity at small angles of attack. α_o is the angle of attack at which v_p is zero. It is dependent on the initial velocity component parallel to the surface and increases with decreasing angles of attack.

This may be represented by: $\gamma = (\frac{v_p}{V\cos\alpha})^2$ where an appropriate function of α to account for the erosion trend is: $\gamma = 1 - \sin(n\alpha)$.

Thus the expression for cutting wear at small angles of attack becomes:

$$\frac{MV^2\cos^2\alpha \sin n\alpha}{2\phi} \qquad 2.22$$

At $\alpha = \alpha_o$, $\sin(n\alpha_o) = 1$, i.e. $\alpha_o = \pi/2n$.
We may study the effect of the angle of impact on erosion by studying the derivatives of these equations. Neglecting Ve these are, for $\alpha > \alpha_o$

$$\frac{dW}{d\alpha} = MV^2\cos\alpha\sin\alpha(\frac{1}{\epsilon} - \frac{1}{\phi})$$

The following observations aid in our understanding of the effect of material and angle of attack on the predominant erosion mode.

- $dW/d\alpha = 0$ $\epsilon = \phi$, and erosion is independent of α for $\alpha > \alpha_o$; and equal to α_{max}
- $dW/d\alpha > 1$ $\phi > \epsilon$, and erosion increases with increasing α; $\alpha_{max} = 90$
- $dW/d\alpha < 1$ $\epsilon > \phi$ and erosion decreases with increasing α; $\alpha_{max} < \alpha_0$ i.e. predominantly cutting wear.

For $\alpha<\alpha_o$ equating the differential to zero yields:

$$\frac{\phi}{\epsilon} = \sin n\alpha_{max} - \frac{n\cos\alpha_{max}}{2\tan\alpha_{max}}$$

where α_{max} is the angle where $dW/d\alpha = 0$.

- for $\phi/\epsilon = 0$ the only possible solution is $\epsilon = \infty$ and therefore no deformation wear occurs.

The above observations are summarised in figure 2.6.

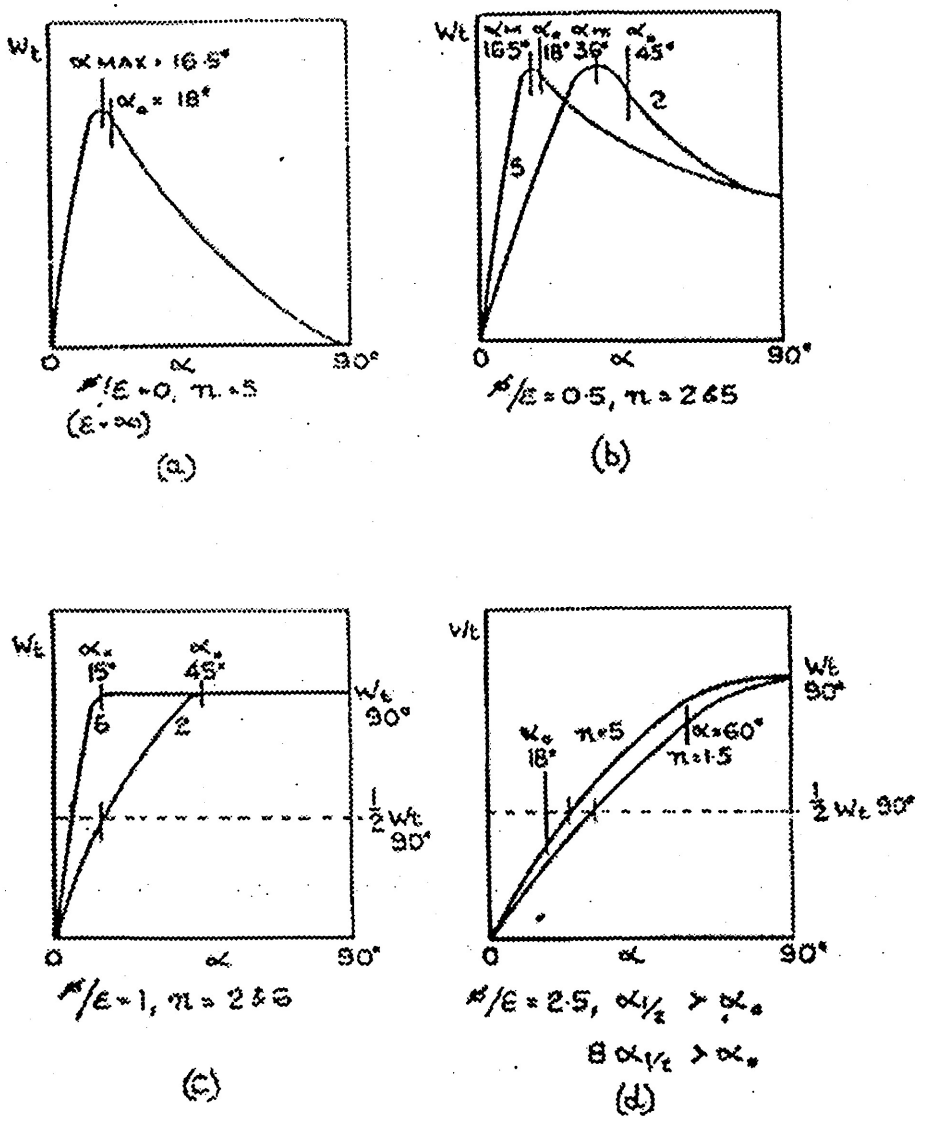

Figure 2.6 Erosive wear of ductile and brittle classes of materials [77]

2.1.4 Tilly

Tilly reports experimental results indicating that, in parallel with Bitter's threshold velocity, there exists a threshold particle size below which no erosion occurs [5]. The reason for this is not clear but may be due to the lower impact stresses of the smaller particles.

The erosion process is thus divided into two stages:

(i) primary erosion in which particles larger than the threshold size erode the material and are broken down in the process; and

(ii) secondary erosion where the particle fragments themselves erode the surface. In this case particle size is not considered.

(i) Primary erosion

Introducing this threshold particle size (d_0) into Bitter's energy balance equation [1] gives the elastic energy term at which erosion just takes place as:

$$Q_e = \frac{\pi}{12}\rho d_0^3 V_e^2$$

Thus the expended energy is:

$$Q_p = \frac{\pi}{12}\rho(d^{\frac{3}{2}}V_r - d_0^{\frac{3}{2}}V_e)^2$$

where V_r is the test velocity.

Rearranging, and introducing a specific energy of primary erosion ϵ, the primary erosion factor E_p is:

$$E_p = \frac{V_r^2}{\epsilon}\left[1-(\frac{d_0}{d})^{\frac{3}{2}}\frac{V_e}{V_r}\right]^2$$

For values of d, V larger than their threshold values, E_p is a maximum for a given V_r. Thus primary erosion at any velocity is given by:

$$E_p = E_{pmax}\frac{V^2}{V_r}\left[1-(\frac{d_0}{d})^{\frac{3}{2}}\frac{V_e}{V}\right]^2$$

Values for threshold size can be obtained from experiment at the test velocity. E_{pmax} can then be calculated from measurements at a velocity and particle size much greater than the threshold values.

(ii) Secondary erosion

Secondary erosion due to particle breakup on impact is assumed directly proportional to the initial kinetic energy of the particle and the extent of fragmentation. No threshold conditions seemed to be in operation. Thus, the secondary erosion factor (E_s) can be expressed as:

$$E_s = \frac{V_r^2}{\epsilon_2} F$$

where ϵ_2 is the energy required to remove a unit volume associated with this secondary erosion, and F the degree of fragmentation. The fragmentation is itself a function of velocity, particle size, and impact angle and is defined:

$$F_{d,v} = \frac{W_o - W}{W_o}$$

where W_0 is the initial proportion of the sample (by weight) within the specified size range and W is the proportion afterwards. If all particles are broken up then F = 1 and this maximum secondary erosion (E_{smax}) will be $V_r^2/2\epsilon_2$.

Secondary erosion at any other conditions is then given by:

$$E_S = E_{smax}\left(\frac{V}{V_r}\right)^2 F_{d,v}$$

The total erosion is then given by:

$$E = E_{pmax}\frac{V^2}{V_r}\left[1-\left(\frac{d_0}{d}\right)^{\frac{3}{2}}\frac{V_c}{V}\right]^2 + E_{smax}\left(\frac{V}{V_r}\right)^2 F_{d,v}$$

Values for the threshold conditions, fragmentation, and maximum erosion can be derived from experiments at one velocity. Figure 2.7 shows the results of such tests, together with experimental data for the predictions.

(iii) Influence of particle size.

For the test conditions considered by Tilly the model above yields a velocity dependence with an exponent greater than two, as expected. Small particles that do not fragment will tend to an exponent of 2 as the velocity increases; likewise conditions much greater then the threshold conditions will yield an exponent of 2.

(iv) Influence of impact angle.

Tilly states that this model adequately accounts for impact angle, primary erosion being dominant at low angles with the role of secondary increasing with increasing angle of impact. However, impact angle is not incorporated in the model above, which is essentially based on Bitters model for normal impacts.

The model is quite complex in that many experiments must be carried out to determine the coefficients and fragmentation. Goodwin, Sage, and Tilly reported a method to calculate the fragmentation. The d_{50} particle size is used with a coefficient of curvature $d_{50}^2/d_{30}d_{60}$ to calculate the change in F as a function of velocity and initial average particle size.

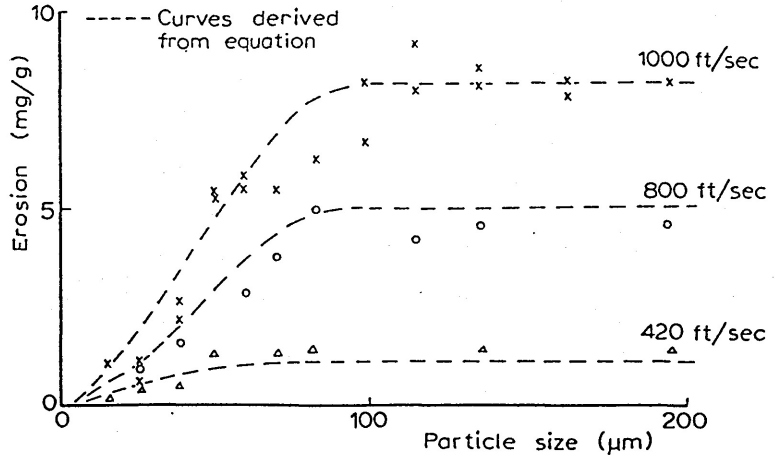

Figure 2.7 Erosion versus particle size [5]

2.1.5 Fairhurst

Fairhurst modelled the erosion process as both cutting wear and deformation wear based on the work of Bitter [6].

Cutting wear was developed almost identically to that of Finnie [2]; however, the material forces at the surface were treated differently by specifying an angle for the reaction forces. This, in effect, is similar to Finnie's inclusion of a ratio of horizontal to vertical forces. This angle would be difficult to determine experimentally, and the ratio of forces is almost constant in practical situations [2], negating the process of choosing a value that best fits the experimental findings.

In addition, the inclusion of both horizontal and vertical reaction forces in the equation of rotation is only valid for elliptical particles, in which case the assumption of $y_t \approx y$ is less accurate.

For deformation wear, the volume of material removed is assumed to be proportional to the kinetic energy of the particle:-

$$W \propto \frac{M(V\sin\alpha)^2}{2}$$

This mode occurs for $\alpha<\alpha_0$ as it is assumed to occur only when the impacting particles are brought to rest. In order to fit the experimental data the final form used for the deformation erosion was:-

$$E_{def} = \frac{E_{max}}{\epsilon}\sin^2(\alpha-\alpha_0)$$

where ϵ is the deformation erosion constant for a particular particle velocity. Figure 2.8 shows the erosion predicted by the combined model against experimental results. δ and ϵ were chosen to give the best fit to the experimental data.

However, the angle of attack for particles less than 150 microns could not be predicted due to divergence of the model for high values of δ.

One important finding of the experiment is the sensitivity of particle erosion is to particle size. Investigation of the shape of the eroded volumes, figure 2.9, suggests that the smaller particles are being deflected by the exiting water and eroding by cutting wear. The larger particles contain increasing amounts of initial energy and are less disturbed by the flow pattern. They continue on their original trajectory, eroding by deformation wear in the example shown.

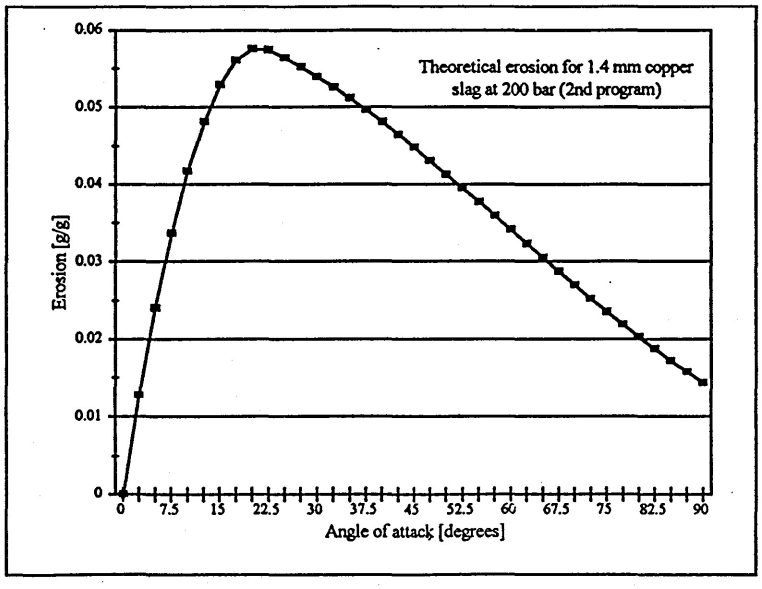

Figure 2.8 Predicted erosive performance of DIAJET system [6]

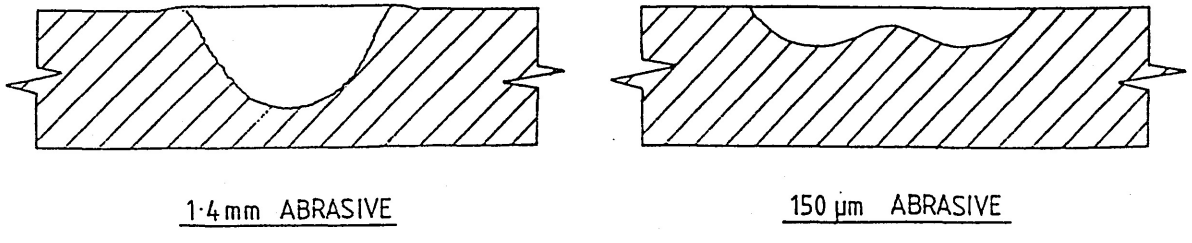

Figure 2.9 Eroded volumes [6]

2.1.6 Hashish

Hashish [7] proposed an improved model of erosion by solid particle impact developed along the lines of Fairhurst above [6]. The cutting wear mode was again developed using a methodology similar to Finnie [2], but taking account of the particle shape. Deformation wear was accounted for by using Bitter's model [1].

(a) Cutting wear

In the cutting wear model, Hashish expanded an existing model of cutting wear [45] to include the crater width variation as the particle ploughed through the material. Figure 2.10 shows schematically a particle ploughing into the surface of the material.

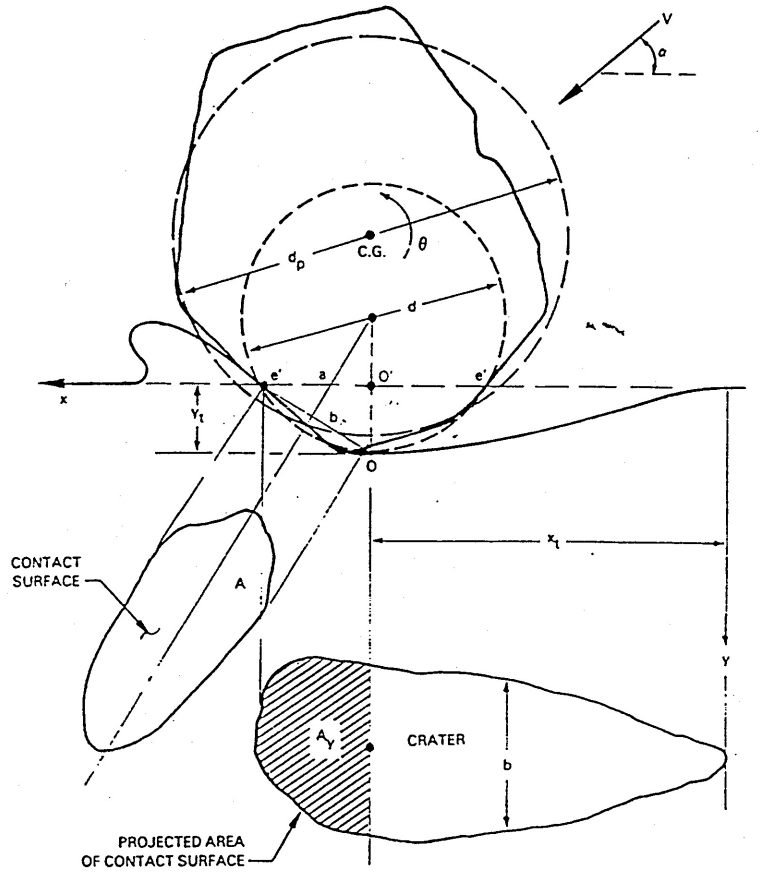

Figure 2.10 cutting wear [7]

Hashish calculates the projected area of the contact surface normal to the y direction is approximately:

$$A_y = \frac{\pi}{2} a^2$$

where a is the contact distance o-e. When y is small compared to d, a can be related to y as:

$$a = \sqrt{yd}$$

The projected area of the contact surface normal to the x direction is equivalent to the segment e-e'. When y is small, the area A_x of this circular segment is:

$$A_x = \frac{4}{3} y\sqrt{yd}$$

The equations of motion are then:

$$m\ddot{x} = -\frac{4}{3}\sigma y\sqrt{yd} \qquad 2.23$$

$$m\ddot{y} = -\frac{\pi}{2}\sigma yd \qquad 2.24$$

$$I\ddot{\theta} = \frac{2}{3}\sigma d_p y\sqrt{yd} \qquad 2.25$$

Equation 2.24 can be re-written as: $\ddot{y} = -\beta_1^2 y$ with $B = \sqrt{\frac{\pi\sigma d}{2m}}$

This is an ordinary differential equation, the solution with boundary conditions y = 0 at t = 0, and y' = Vsin α at t = 0 yielding:

$$y = \frac{V\sin\alpha}{\beta_1}\sin\beta_1 t$$

Similarly we can write for x_t and θ:

$$\ddot{x} = -\frac{8\beta_1^2}{3\pi\sqrt{d}} y\sqrt{y}$$

$$\frac{d_p}{2}\ddot{\theta} = \frac{2\beta_1^2}{3\pi d}\left(\frac{md_p^2}{I}\right) y\sqrt{y}$$

Combining with the derivative, equation 2.23 yields:

$$\ddot{x}_t = -\Omega y\sqrt{y}$$

and substituting for y:-

$$\ddot{x}_t = -\Omega(\frac{V\sin\alpha}{B_1})^{1.5}\sin\beta_1 t^{1.5} \qquad 2.26$$

where $$\Omega = \frac{8B_1^2\gamma}{3\pi\sqrt{d}}, \qquad \gamma = 1 + \frac{mr^2}{I}$$

For spherical particles γ has a value of 3, and 4⅓ for abrasive particles. Equation 2.26, above, can be integrated to calculate the x component of the tip velocity as:

$$\dot{x}_t = V\cos\alpha - \Omega(\frac{V\sin\alpha}{B_1})^{1.5}\int_0^t \sin\beta_t^{1.5}\,dt$$

The total volume of material swept by the particle is given by:

$$\delta v = \int_0^t A_x\dot{x}_t\,dt + \int_0^t A_y\dot{y}\,dt$$

Using the following substitutions

$$\Omega_2 = V\cos\alpha$$

$$\Omega_1 = \frac{4}{3}\sqrt{d}(\frac{V\sin\alpha}{B_1})^{1.5}$$

$$\Omega_3 = (\frac{V\sin\alpha}{\beta_1})^{1.5}\Omega$$

$$I_n = \int_0^z \sin z^{1.5}, \qquad z = \beta t$$

Thus

$$\delta v = I_n(\frac{\Omega_1\Omega_2}{\beta_1})[1-(\frac{1}{2}\frac{I_n\Omega_3}{\beta_1\Omega_2})] + \frac{\pi}{4}d(\frac{V\sin\alpha}{B_1})^2\sin^2 Bt_1 \qquad 2.27$$

As with the previous analysis, cutting stops when one of the following conditions occur:

1) Particle exits material after ploughing out a volume, y=0 at $t = t_c$

2) Particle loses one or both of its components of momentum.

1) For the case where the particle exits the material, equation 2.24 yields

$$t_c = \frac{\pi}{\beta_1}$$

Thus the second term of equation 2.27 is zero, and the first term becomes:

$$\frac{\delta v}{d^3} = \frac{7}{6}\left(\frac{V}{V_K}\right)^{2.5}\sin 2\alpha\sqrt{\sin\alpha}\left[1-\frac{7\gamma}{3\pi}\sqrt{\frac{V}{V_K}}\frac{\sin\alpha^{1.5}}{\cos\alpha}\right] \qquad 2.28$$

where V_k is the characteristic velocity defined as

$$V_K = \beta_1 d$$

2) The condition of the particle exiting the material will be true for shallow angles of impact (less than α_0) which satisfies the condition

$$\dot{x}_t = 0, \quad t = t_c$$

Noting equation 2.26 can be re-written as:

$$\dot{x}_t = \Omega_2 - \frac{I_n \Omega_3}{\beta_1}$$

the boundary condition yields:

$$\frac{I_n \Omega_3}{\beta_1 \Omega_2} = 1 \qquad 2.29$$

Substituting for Ω_2 and Ω_3 and I_n into 2.29 gives the limit angle as

$$\tan\alpha_o\sqrt{\sin\alpha_o} = \frac{3\pi}{14\gamma}\sqrt{\frac{V_K}{V}}$$

For $\alpha < 30°$, we can ignore the second bracketed term in equation 2.28, giving a simplified value for the erosion as:

$$\frac{\delta v}{d^3} = \frac{7}{6}\left(\frac{V}{V_K}\right)^{2.5}\sin 2\alpha\sqrt{\sin\alpha}$$

Substituting $m = (\pi/\sigma)\,\rho_p\, dp^3$ and $R_f = d/dp$, V_k as previously defined yields:

$$\delta v = \frac{7}{\pi}\frac{m}{\rho_p}\left(\frac{V}{C_k}\right)^{2.5}\sin 2\alpha\sqrt{\sin\alpha} \qquad 2.30$$

where,

$$C_K = \sqrt{3\sigma\frac{R_f^{\frac{3}{5}}}{\rho_p}} \qquad 2.31$$

This equation gives the erosion dependence on velocity of 2.5, more in-line with the experimental results than Finnie's original model [2].

(b) Deformation wear.

For near normal impacts, Hashish uses the model developed by Bitter for erosion [1], namely:

$$\delta v = \frac{m(V-V_e)^2}{2\sigma}$$

2.1.7 Sheldon and Kanhere

From experimental investigations, and analysis of the work of Goodwin et al. [78], Sheldon and Kanhere [50] developed a model of erosion based on the indentation hardness characteristic of material [79].

The work performed by an indenting sphere is:

$$= \int_0^x F dx = \int_0^x a\delta^n dx$$

where δ is the rim diameter at a penetration of x.

Geometrically, this may be expressed as:

$$2x = D-(D^2-\delta^2)^{0.5}$$

where D is the particle diameter. Equating this energy to the particle kinetic energy for normally impacting spheres, namely

$$= \frac{1}{2}\left(\frac{4}{3}\pi\left(\frac{D}{2}\right)^3\right)\rho_p V^2 \sin^2\alpha$$

yields

$$\frac{\pi}{12}D^3\rho_p V^2 = \frac{1}{2}\int_0^d \frac{a\delta^{n+1}}{(D^2-\delta^2)^{0.5}}d\delta$$

where d is the final value of δ. Substituting $\delta = D\sin\theta$ and $d = D\sin\theta_1$ we get

$$\frac{\pi}{12}\frac{\rho_p V^2}{D^{n-2}} = \frac{1}{2}\int_0^{\theta_1} a\sin^{n+1}\theta d\theta$$

Similarly, for the maximum values of x

$$\frac{2x_{max}}{D} = 1-\cos\theta_1$$

Assuming n = 2 and replacing Meyer's hardness with the Vicker's hardness (Hv) we get:

$$V\left(\frac{\rho_p}{H_v}\right)^{\frac{1}{2}} = 1.23\left(\frac{1}{3}(2-3\cos\theta_1+\cos^3\theta_1)\right)^{0.5}$$

Assuming the volume removed is equal to the full crater and noting the linear relationship between x_{max} and V we get:

$$W \approx q^3 = x^3\frac{D^3 v^3 \rho_p^{1.5}}{H_v^{1.5}} \qquad 2.32$$

Thus a model with a velocity dependency (and particle size dependency) of 3 is established. The model also provides an easy comparison between material, with the inclusion of Vickers hardness, although its exponent was not fully verified.

For high impact velocities the rigid particle assumption must be abandoned for particle deformation, in accordance with experimental observation. This gives a velocity exponent on penetration of 1.5, yielding a velocity squared relationship for erosion.

2.1.8 Jennings, Head, and Manning

Based on earlier findings by Smeltzer [27] which revealed that up to 95% of the energy is dissipated thermally, Jennings et. al. developed a model based on melting of the surface combined with removal of material bonded to previous particles [28].

Scanning electron microscopy analysis of the impacted surface confirmed the earlier work. A predictive model was then developed based on the experimental findings yielding the erosion as:

$$E = \left(\frac{K_t^{\frac{5}{2}} \quad G^{\frac{1}{3}}}{R \quad \rho_p^{\frac{1}{3}} k T_m \Delta H_m} \right) S$$

The kinetic energy transferred per unit mass is $K_T = \frac{1}{2} \frac{M(V_1^2 - V_R^2)}{M}$.

Although the model is sensible, predicting erosion proportional to kinetic energy and inversely proportional to roundness and material resistance, its usefulness is limited as the rebound velocity (V_R) cannot be calculated.

One important finding from the study is that once a certain level of kinetic energy has been reached, neither increased velocity nor particle angularity appreciably affect the erosion rate.

2.1.9 Kim and Zeng

The mechanics of brittle erosion was originally investigated by Kim and Zeng [80] from a static balance analysis based on the energy balance approach of Bitter [1].

Based on scanning electron microscopy analysis of the surface of eroded ceramic, and the observations of other researchers on the fracture damage of alumina due to charges, this model was extended to include the stress waves propagated as particles impact the surface.

This, in effect, adds an additional term to the static energy balance equation. This volume removed due to dynamic fracture is calculated from energy analyses [25]. A proportion of this energy, f_w, is then assumed to be used in fracture, the remainder being lost in internal friction. Using a crack network model to approximate the fractured region as a hemisphere constructed from cuboids equal in size to the grain size, the volume removed is given by:

$$V_f \frac{f_c f_w a\, \eta(\nu) m\, V_0^2 \sin^2\theta}{12\gamma(1-\phi)} \left(\frac{\rho}{\rho_p}\right)^{\frac{1}{2}} \left(\frac{P}{E}\right)^{\frac{3}{2}}$$

where f_c is an empirical coefficient, a is the grain size, $\eta(\upsilon)$ is a function of Poisson's ratio, γ the grain boundary fracture energy, P the dynamic hardness and E the modulus of Elasticity of the material. All other terms have their usual meaning.

Trials carried out to prove the validity of this model for near normal impacts, where deformation erosion is minimal. A good correlation was found. Similar analysis is necessary to calculate the erosion due to small angles of attack.

2.1.10 Hutchings

Based on extensive experimental findings that erosion can produce platelet type wear debris, Hutchings proposed a model of accumulated plastic deformation from multiple normal impacts leading to material removal once a "critical strain" is reached [4]. This value of ϵ_c, the critical strain, is a material property, which Hutchings calls "erosion ductility".
Random walk theory was used to predict the resultant strain after N impacts of strain $\Delta\epsilon_p$ each, as $\Delta\epsilon_p N^{1/2}$. Thus, if N_f is the number of particle impacts to cause failure we can write:

$$\Delta\epsilon_p N_f^{1/2} = \epsilon_c$$

Hutchings notes the similarity between this, and the Coffin-Manson equation for low cycle fatigue $\Delta\epsilon_p N_f^b = \frac{1}{2}\epsilon_f$ with b = 0.5 for metals in uniaxial loading. This equation has been used previously by Hitchings for ewear prediction [33].

Assuming that the material resists indentation with a constant pressure P (the quasi-static hardness), and that all the kinetic energy is used in plastic deformation, the volume of the indentation is given by [4]:

$$V = \frac{mv^2}{2P}$$

The actual volume of material plastically deformed around the indentation will be less than this. Hutchings assumes a constant α, dependent on indentation geometry, impact velocity and the target material. Stephenson reports that, from experiment, a figure of 70-80% of the total kinetic energy should be used in the first instance [81].

Thus Hutchings' total erosion is given by: $E = \frac{\alpha\rho v^2}{2PN_f}$. The average strain per impact for a sphere of radius r is approximated as $\epsilon \approx 0.2\ a/r$ where a is the final chordal radius of the indentation. Equating the initial kinetic energy to the work done in forming the indentation, Hutchings derives: $a = r\sqrt{2v}\left(\frac{2\rho_p}{2P}\right)^{\frac{1}{4}}$.

Combining the above three equations with the probability/fatigue equation yields:

$$E = 0.033\frac{\alpha\rho_m\rho_p^{\frac{1}{2}}v^3}{\epsilon_c^2 P^{\frac{3}{2}}}$$

Note the prediction of velocity dependence of three in the denominator.

Hutchings then discusses the simplifications of the model in assuming constant material properties and strain rate regardless of particle size or work-hardening effects. Also, the material properties used require erosion tests to determine their values. Never-the-less, this approach has been sucessfully used to model high temperature erosion [82]

2.1.11 Kragelsky et al

Material removal in layers by a combination of deformation wear and frictional fatigue was suggested by Kragelsky et al to predict erosive wear [3]. These mechanisms are assumed to act independently in the tangential and normal direction, respectively. Both have independent threshold values before material removal starts.

The frictional erosion rate is given by $\epsilon_t = \frac{h_t A}{n_0 n_t} N$ where h_t is the layer thickness, A the cross-sectional area of the erosed surface (the jet diameter in the case of awj cutting), n_0 the number of particles simultaneously impacting the surface, N the total number of particles, and n_t the threshold number of cycles before damage at the given operating stress. A similar equation is given for the deformation wear component.

Both N and n_0 are given by the abrasive flow rate and the interparticle spacing (in the case of awj cutting, the jet diameter and the abrasive concentration). The findings of Zolotar [33] are used to calculate the h, the depth of penetration of the particle. This is given in terms of material properties for both the cases of elastic and plastic contact. The value of material strength used for plastic deformation is that used by Bitter [1], namely a multiple of the yield strength. This multiple depends on the impact velocity, and Kragelsky also shows a dependancy on impact angle [3]. The relevant material properties, such as yield stress and elongation, are significantly affected by temperature rises occuring in the frictional fatigue mode.

The threshold values, or number of cycles required to erode a surface, are given also in terms of the material properties strength and elongation as well as the mean contact pressure.

The resulting equations for material erosion predict a velocity dependence of 2.5 for low angle, frictional fatigue, as is expected from experiment [2]. The deformation wear mode yields an exponent of 2, also as expected [1].

2.2 Cutting by abrasive water jet

2.2.1 Hashish

Hashish reported on modelling the performance of an abrasive water jet using the previously developed model of particle erosion, section 2.1.6. Figure 2.11 details the development of the abrasive water jet as it passes through the material.

Assuming that the abrasives are spread uniformly distributed over the cross-sectional area of the jet, we can write:

$$dm = \dot{m}\frac{dx}{d_j} \qquad 2.33$$

where d_j is the jet diameter.

For steady state cutting, the material traversal rate should equal the material erosion rate. As the erosion rate decreases with depth (due to wall drag and particle deflection), the curvature of the steady-state interface increases.

However, the following equation will always hold in the steady state:

$$\delta\dot{v} = dh\ u\ w \qquad 2.34$$

where w is the width of the cut at depth h, assumed equal to the jet diameter.

From an analogy with Bitter's threshold velocity [1], and experimental findings of many researchers, the erosion equation 2.30 was modified to include a threshold value for velocity, and rewritten to give:

$$\delta\dot{v} = \frac{14}{\pi}\frac{d\dot{m}}{\rho_p}\left(\frac{V\sin\alpha - V_e}{V_k}\right)^{2.5}\cot\alpha$$

Substituting equations 2.33 and 2.34 yields:

$$\frac{dh}{dx} = \frac{14m}{\pi\rho_p\mu d_j^2}\left(\frac{V\sin\alpha - V_e}{C_K}\right)^{2.5}\cot\alpha \qquad 2.35$$

At the start of the cut, h = 0, dh/dx = cot α_t. Applying these initial conditions in equation 2.35 gives α_t from:

$$\frac{(V_o \sin\alpha_t - V_e)}{C_K} = \left(\frac{14m}{\pi \rho_p \mu d_j^2}\right)^{-2/5} \qquad 2.36$$

Assuming the particle velocity remains unchanged over the shallow depth, h_c, the angle of impact and the depth of cut can be approximated from:

$$h_c = d_j \cot\alpha_t \qquad 2.37$$

Now $\cot\alpha_t = \frac{1}{\sin\alpha_t}$, thus $\sin\alpha_t$ can be calculated as:

$$\sin\alpha_t = \frac{V_e}{V_o} + \frac{1}{\left(\frac{14m}{\pi \rho_p \mu d_j^2}\right)^{2/5}\left(\frac{V_o}{C_K}\right)} \qquad 2.38$$

Combining equation 2.38 with equation 2.37 gives the equation for the depth of the cutting wear mode to be:

$$h_c = \frac{\left(\frac{V_o}{C_K}\right) d_j}{\left(\frac{\pi \rho_p \mu d_j^2}{14m}\right)^{2/5} + \left(\frac{V_e}{C_K}\right)} \qquad 2.39$$

This equation only holds true for $V_e > V_0 \sin\alpha$.

For deformation wear we have

$$\delta v = \frac{m(V - V_e)^2}{2\sigma} \qquad 2.40$$

In this case, frictional losses as the jet passes through the material will be considered, as h_d can be tens of nozzle diameters. The jet is decelerated as it penetrates through the material due to spreading effects and friction drag on the kerf wall.

Considering the equation of momentum of a control volume bounded by the jet and kerf wall:

$$\dot{m}_t v = \dot{m}_t V_0 - F_f$$

where

$$F_f = C_f A_w \frac{\rho V_0^2}{2}$$

The area of the control volume is approximately

$$A_w \approx \frac{\pi d_j h}{2}$$

Combining the above three equations yields:

$$V = V_o(1 - K_w h) \qquad 2.41$$

where $K_w = \frac{C_f}{d_j}$ C_f being the coefficient of frictional drag. The mass flow rate of abrasive is given by:

$$\dot{m}_t = \frac{\pi}{4} d_j^2 \rho_m V_0 = Constant$$

Therefore we can write

$$K_w = \frac{C_f}{d_j}$$

Substituting into equation 2.40 for deformation wear yields:

$$\delta \dot{v} = \frac{\dot{m}}{2\sigma}\left[V_0(1 - K_w h)^2 - V_e\right]^2 \qquad 2.42$$

The volume removal rate of the step, figure 2.12, at a depth h can be expressed by multiplying the penetration rate by the area of the step, A_c, which is assumed equal to the jets cross-sectional area.

$$\delta\dot{v} = A_c\frac{dh}{dt} = \frac{\pi}{4}d_j^2\frac{dh}{dt} \qquad 2.43$$

Equating equations 2.42 and 2.43 and re-arranging yields:

$$\int_{h_c}^{h_t}\frac{dh}{(1-K_{wh})^{2.5}} = \frac{Cd_j}{2.5}\left(\frac{14m}{\pi u\rho_p d_j^2}\right)^{2/5}\left(\frac{V_o}{C_K}\right)$$

Neglecting wall friction in the cutting wear mode, the limits above can be changed to 0 to h_d. This yields the depth of cut in the deformation wear mode as:

$$h_d = \frac{1}{\dfrac{\pi d_j\sigma u}{2C_1\dot{m}(V_0 - V_e)^2} + \dfrac{C_f}{d_j}\dfrac{V_0}{V_0-V_e}} \qquad 2.46$$

α_t is calculated from equation 2.36, assuming $\alpha_t = \sin\alpha_t$.

Two material properties need to be determined to use this model. These are the material stress σ and the threshold velocity V_e. The threshold velocity, that velocity below which no erosion will take place, has been calculated previously [1]. Its value depends on physical properties of both the material and the abrasive, also on the shape of the abrasive particle. In this model, however, Hashish finds this value experimentally for the material under test to best fit the data points.

For single point tools, the material strength is related to the shear stress required to cause slippage. This has a maximum theoretical value of approximately E/10. From the extensive experimental work carried out by Hashish, a value of E/14 was chosen to yield better correlation [7].

Hashish reports that C_f can be calculated from boundary layer theory, but does not expand on this. Its value lies between 0.001 and 0.005, with a value of 0.002 seeming adequate for the entrainment system under consideration cutting material up to 50 mm thick. From an analogy with pipe friction along the control volume wall, it is equal to one half of the Moody friction factor.

Hashish attempted to model these striations occurring in the deformation wear zone by the cyclic unsteady removal of steps [56]. The resulting model is only partially successful, with the effect of taper being cited as the main cause for inaccuracy.

The waviness (ie striations) of the surface is modelled from the unsteady development of the jet/material interface. The jet traversal during the time taken to cut to a depth h is calculated to yield the distance, x, travelled by the jet during the formation of one striation. The waviness created by the successive jet diameters, spaced x apart is then given by:

$$\frac{2R_w}{d_m} = 1 - \sqrt{1 - \frac{\pi^2}{4}\left(\frac{d_m(h-h_c)u}{0.5\,m_a\frac{V_a^2}{\epsilon}}\right)^2}$$

where ϵ is the specific energy for deformation wear mode, ie a fraction of Young's modulus.

As the abrasive water jet changes direction an overshoot, or undershoot, occurs due to the deflected form of the jet. This is minimised by careful selection of the acceleration and deccelertion of the jet.

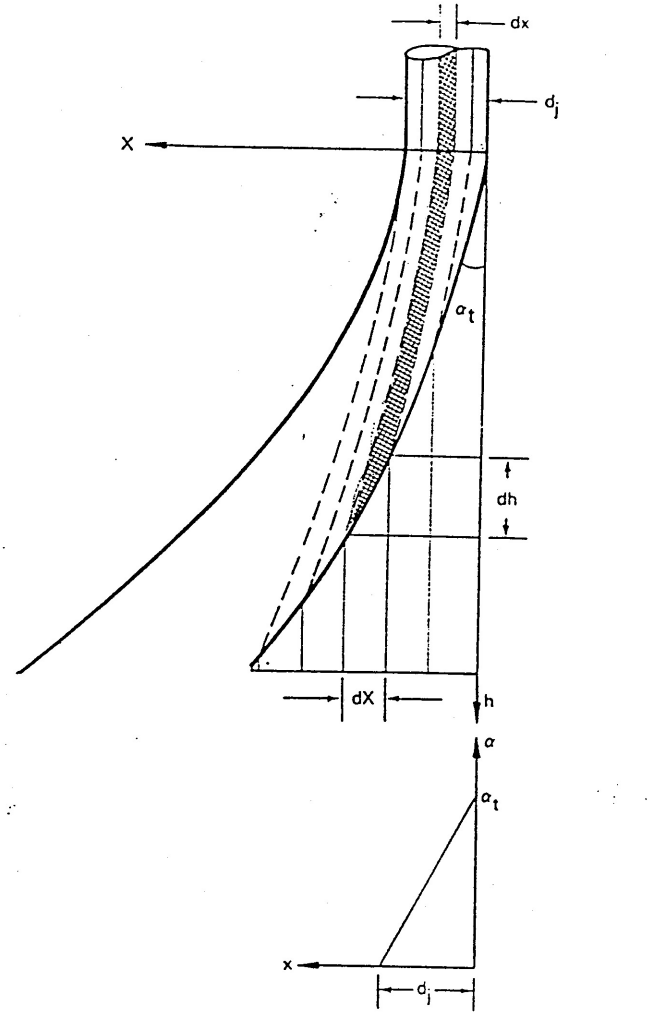

Figure 2.11 Development of the jet throught the material [7]

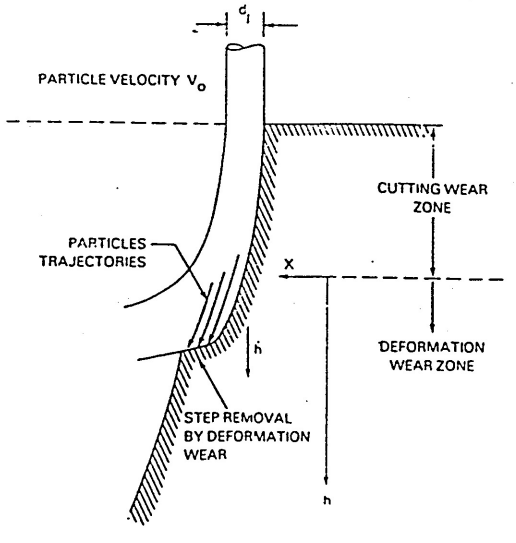

Figure 2.12 Step removal (deformation wear) [7]

2.2.2 Walters and Saunders

Walters and Saunders empirically modelled a DIAJET system cutting ductile materials by empirical means [83]. For the test parameters considered, viz. pressures from 350 to 690 bar and nozzle sizes of 1 and 2 mm internal bore, an equation was fitted to the test points yielding the following relationship:

$$AU = 83.9 d^{0.3} (600 + 3.33\, conc)(P - 110)^{-.68}$$

where AU is the abrasive usage [kg/m^2 cut surface generated]. The impetus for the study was to assess the effectiveness of different abrasive water jet cutting systems and their parameters on cutting efficiency. Of chief concern was the cut surface generated per unit of abrasive, a major requirement in the nuclear decommissing industry being minimising waste.

Abrasive feed rates of up to 25% were used at 690 bar with a 1 mm nozzle cutting stainless steel at a range of cutting speeds up to 2 m/min. The following figures show the results observed, from which the model was developed.

From figure 2.13 the relationship between abrasive usage and abrasive concentration (in percent) is:

$$AU = 600 + 3.33\, conc$$

i.e. a slight increase in abrasive usage was noted with increasing abrasive concentration. This was assumed due to the decrease in particle velocity with increasing concentration. The water usage may then be expressed as:

$$WU = \frac{60000}{conc} - 3.33\, conc - 267$$

This relationship between water usage and pressure, figure 2.14 , can be expressed as:

$$WU = 172000\ (P - 110)^{-.68}$$

Note the inclusion of a threshold pressure, below which no cutting was observed. This is identical in concept to the idea of a threshold velocity [1].

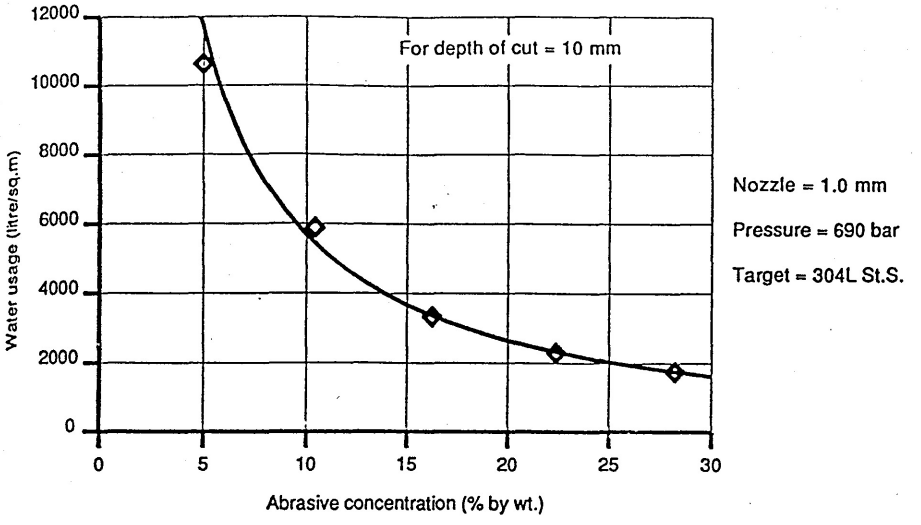

Figure 2.13 Relationship between water usage and abrasive concentration [83]

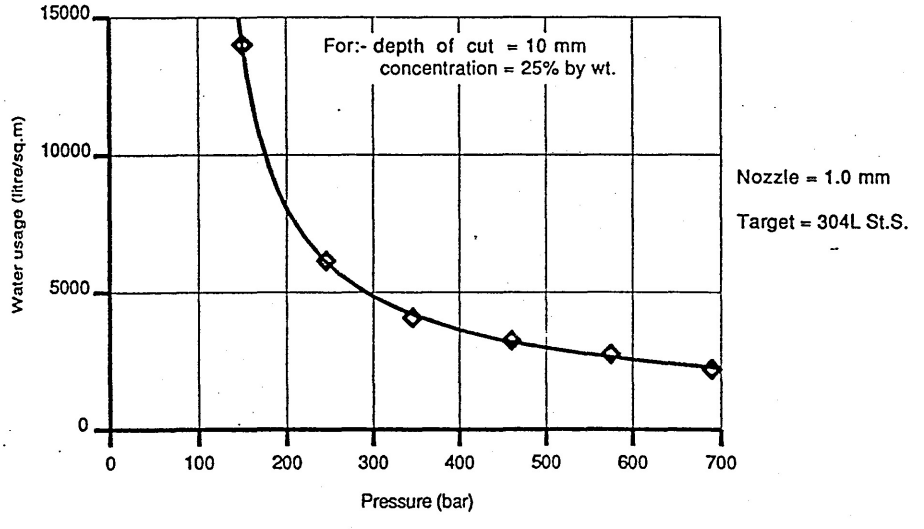

Figure 2.14 Relationship between water usage and pressure [83]

From previous studies, Saunders [54] had proposed a power law relationship between depth of cut and nozzle size all else being equal, namely $AU = 1300\, d^{.3}$ Combining the previous models gives an expression for the abrasive usage as

$$AU = 83.9\, d^{.3}\left(\frac{60000}{conc} - 3.33\, conc - 2.67\right)(P - 110)^{-.68} \qquad 2.45$$

This model provides a good experimental correlation at operating conditions clsoe to those quoted. It also confirms that the general trends predicted from the erosion models are applicable to abrasive water jet cutting. Once trial cuts are conducted on the target material at the operating parameters required, a similar empirical fit can be carried out to predict cutting results.

The above prediction applies only to the test material, 304L stainless steel. Additional experimental work is necessary to predict the cutting performance on other materials, resulting in the inclusion of an additional factor in the above equation. Comparison of these factors shows that their ratios are similar to the machinability index of material [84], generally proportional to the reciprocal of their hardness. This validates the findings of the erosion models on material dependency.

2.2.3 Abudaka

Abudaka developed a model of abrasive water jet cutting using Finnie's model for cutting wear and Bitter's model for deformation wear [58].

The model for shallow angle particle erosion, for a particle with a moment of inertia of $\frac{1}{2}mr^2$ is given by [23]:

$$\delta\dot{v} = \frac{d\dot{M}v^2}{4\sigma_p}(\sin 2\alpha - 3\sin^2\alpha)$$

As in the model proposed by Hashish [7], the steady state volume removal can be written as $\delta v = dhud_j$

The abrasives are similarly assumed spread over the entire cross-sectional area of the jet

$$dm = \left(\frac{\dot{M}}{d_j}\right) dx$$

Integrating these equations and including a factor c as the ratio of the jet diameter involved in cutting wear yields the depth of cut for the cutting wear mode as:

$$h_c = \frac{c\dot{M}v^2}{4\sigma d_j u_x}$$

where α_1 is a function of α. This function is highly dependent on the shape of the steady state cutting front, but its actual derivation is not reported.

The large impact angle erosion rate is calculated according to Bitter's model neglecting the critical velocity. Assuming a cylindrical volume of material is removed, of diameter d_j and length h_d, and ignoring the change in velocity with increasing depth yields a value for the deformation wear depth as:

$$h_d = \frac{2(1-c)\dot{M}v^2}{\pi d_j \epsilon u}$$

The factor for the percentage of effective particles used in deformation wear was chosen as the remaining fraction of particles not used during the cutting wear (1-c).

Abudaka uses the yield strength σ_y of the material in calculating the cutting wear depth. As the cut depth arising from the deformation wear mode is proportional to the reduced modulus of elasticity of the material, E/10 [1], Abudaka argues that this 'deformation' depth would be significantly smaller, and ignores it.

Brittle materials are modelled separately, as [50]

$$W = k_5 r^{a} V^{b}$$

$$where \quad a = \frac{3.6m}{m-2} \quad and \quad b = \frac{2.4m}{m-2}$$

Due to the limited validation trials reported in this reference, it is difficult to ascertain the success of this approach to modelling the cutting depth. However, another model developed with similar assumptions (as part of the BRITE programme on precision machining) has proven difficult to validate with cutting data [85].

2.3 Review of acceleration models

2.3.1 Finnie

In order to investigate the wear of pipes due to particles carried in fluids and gases, Finnie estimated the distance travelled by a single particle, introduced at rest into a gas stream, before it acquires a given percentage of the gas velocity [2]. The only force considered to act on the particle is that of frictional drag. The equation of particle motion is then:

$$\frac{4}{3}\pi r^3 \rho_p \frac{dV}{dt} = \frac{C_D}{2}\rho_a \pi r^2 (U-V)^2 \qquad 2.36$$

where r, V and ρ_p are the particle radius, velocity, and density, U and ρ_a are the fluid velocity and density, and C_D is the drag coefficient. Putting

$$K = \frac{3C_D\rho_a}{8r\rho_p}$$

and noting that dV/dt = 0 at t=0, equation 2.36 becomes:

$$-d(U-V)dT = K(U-V)^2$$

Integrating and using the initial conditions, V=0 at t=0, yields

$$\frac{V}{U} = \frac{UKt}{1+UKt}$$

or

$$\frac{1}{U-V} - \frac{1}{U} = Kt$$

Integrating again yields the distance travelled by the particle in a given time as:

$$x = \frac{1}{K}[UKt - \ln(1+UKt)]$$

Finnie concluded that, for the cases he was considering in air, the particle travelled such small distances that they attained low velocities and this, combined with indeterminate particle sizes, leads to the difficulties in correlating his model with actual erosion data.

2.3.2 Fairhurst

Fairhurst, expanded on Finnie's model of particle acceleration to calculate the exit velocity of a particle within a DIAJET nozzle [6].

Assuming an incompressible flow (actually, water has a compressibility of 3% at 700 bar, and 10% at 2000 bar) and negligible inlet velocity, Bernoulli's equation applied across the nozzle gives:

$$P = \frac{\rho_J U^2}{2} + \Delta P \qquad 2.37$$

where ρ_J is the average density of the fluid and solid, i.e.

$$\rho_J = \rho_w C_W + \rho_P C_P \qquad 2.38$$

ΔP is the pressure drop across the nozzle, and C_w and C_p is the mass concentration of the water and abrasive respectively. Assuming fully developed pipe flows the pressure drop due to wall friction may be written as:

$$\Delta P = \frac{fLU^2}{2D} \qquad 2.39$$

Equating 2.37 and 2.39 gives

$$L = \frac{D}{f}\left[\frac{2P}{\rho_J U^2} - 1\right]$$

or

$$U = \left(\frac{2P}{\rho_j \left[1 + \frac{fL}{D}\right]}\right)^{\frac{1}{2}} \qquad 2.40$$

Iterative methods must be used due to the fact that f and C_D are functions of the velocity.

2.3.3 Guo, Cheng, Liu

Guo used a simplified theory of two phase flow to model the acceleration of particle within the DIAJET nozzle [8]. The equation of motion of the particle is given by:

$$\frac{du_p}{dt} = \frac{3C_D\beta}{4\alpha d_p}(u-u_p)^2 + \frac{3\beta}{2\alpha}\frac{du}{dt} \qquad 2.41$$

where $\beta = \frac{\rho}{\rho_p}$ *and* $\alpha = 1 + \frac{\beta}{2}$

Assuming constant flow equation 2.41 can be written in the time domain to give

$$\frac{du_p}{dx} = \frac{3C_D\beta}{4\alpha d_p}\frac{(u-u_p)^2}{u_p} + \frac{3\beta}{2\alpha}\frac{du}{dx} \qquad 2.42$$

The cross-sectional area of the conical section is described by $A = \pi(R-X\tan\theta)^5$ where R is the entry radius and θ half the convergent angle.

Conservation of momentum across a volume (of uniform length) yields

$$\frac{\partial\,[\,\rho f u + \rho_P(1-f)\,u_P]\,A}{\partial x} = 0 \qquad 2.43$$

where f is the water voidage (percentage volume filled by water as opposed to abrasive).

If ϕ is the abrasive concentration, then equating ratios per unit area gives

$$\frac{fu}{(1-f)u_p} = \frac{1-\phi}{\phi}$$

Rearranging yields the volume fraction of abrasive as:

$$f = \frac{(1-\phi)u_p}{\phi u + (1-\phi)u_p} \qquad 2.44$$

To calculate the velocity of water as a function of distance, Guo applies the conservation of momentum thus accounting for the volume reduction, and increased water velocity, due to the presence of abrasive. The initial condition is X=0, $u=u_p=u_o$, $A=\pi R^2$ where u_o is the initial water velocity. The equations are then solved using the Euler numerical approximation. The results of this show that little acceleration of the particles takes place in the convergent section, whilst the water is almost fully accelerated here.

In the cylindrical section, the water velocity was assumed constant, simplifying equation 2.42 to $u_p \frac{du_p}{dx} = \frac{3C_D\beta}{4\alpha d_p}(u_w-u_p)^2$ where u_w is the previously calculated water velocity.

The solution of this is:

$$\frac{1}{1-\frac{u_p}{u_w}} + \ln\left(1-\frac{u_o}{u_w}\right) = \frac{3C_d\beta}{4\alpha}\frac{x}{d_p} + C$$

Assuming that the velocity of particles at the entrance of the cylindrical section is u_{po}. Introducing a function, called the distance function, f(u) $f(u) = \frac{1}{(1-u)} + \ln(1-u)$
Then

$$x = \frac{4\alpha}{3C_D\beta} d_p \left[f\left(\frac{u_p}{u_w}\right) - f\left(\frac{u_{po}}{u_w}\right)\right]$$

This can be used to study the effects of parameter changes within the nozzle.

2.3.4 Shimizu and Wu

Shimizu and Wu [9], in an attempt to understand better the relationship between the structure of an abrasive suspension jet, modelled the acceleration of a particle through the nozzle as follows:

$$M_A\frac{dV_A}{dt}=F_p+F_C+F_v+F_B$$

where the forces on the right hand side are due to pressure gradient, drag, virtual mass and the Basset history integral respectively. These are given as:

$$F_P=\frac{4}{3}\pi r^3\frac{dp}{dx}$$

$$F_D=\frac{1}{2}\pi r^2 C_D(V_w-V_A)|V_W-V_A|$$

$$F_B=6C_B r^2\sqrt{\pi\rho\mu}\int_0^t\frac{d(V_W-V_A)/d\tau}{\sqrt{t-\tau}}dt$$

$$F_V=\frac{2}{3}\pi r^3\rho C_V(\frac{dV_W}{dt}-\frac{dV_A}{dT})$$

This model is more comprehensive than any of the previous but, unlike Guo, the water velocity is calculated assuming no abrasive. The approximate equation of continuity, and Bernoulli's equation are applied at any cross section are:

$$D^2V_W=Constant$$

$$p_1+\frac{\rho V_{W1}^2}{2}=p_2+(1+\zeta)\frac{\rho V_{W2}^2}{2}=p_3+(1+\zeta+\lambda\frac{L_F}{D_F})\frac{\rho V_{W3}^2}{2} \qquad 2.45$$

where λ the coefficient of pipe friction, and ζ the coefficient of contraction and the subscripts 1,2,3 denote the nozzle inlet, nozzle inlet, and nozzle outlet respectively.

Solving the above equations by numerical methods yields a graph of water and abrasive variation within the nozzle, figure 2.15. The shape of the convergent section of the nozzle had little effect on the final velocity of the particles. An increase in particle velocity with decreasing particle size is also predicted.

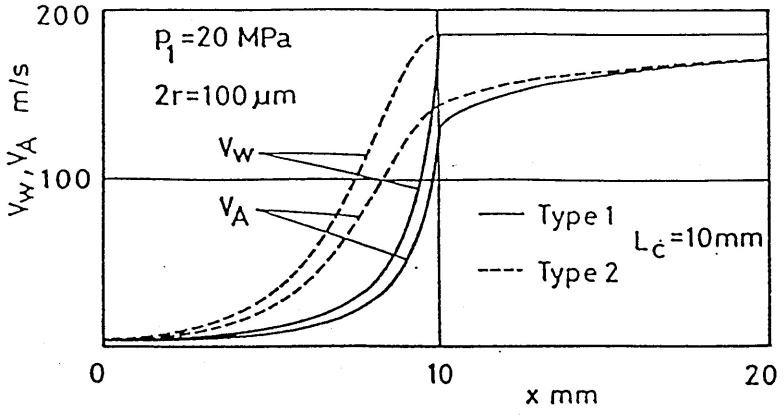

Figure 2.15 Velocity through the nozzle [9]

2.3.5 Pekarek, Lowe, and Huitt

Pekarek et al. [12] carried out a theoretical investigation into the effect of the nozzle on hydraulic notching in oilfield applications, in some of the first reported research into the application of abrasive water jets. The equation of motion of the particles was used to study both the acceleration of the abrasive within the nozzle, and the decelleration in the spreading jet.

They considered the equation of motion of the particle to be influenced by two terms only; the drag force and the virtual mass force. This yields an equation of motion similar to Guo, section 2.3.3

$$\frac{dv_p}{dx} = \frac{3C_D\rho_w v_p}{4d(\rho_p + C_m\rho_w)}\left(\frac{v_w}{v_p}-1\right)\left|\frac{v_w}{V_p}-1\right|$$

Pressure gradients are not considered in this model.

Applying continuity across the converging section of a nozzle, the velocity of the water (ignoring the area reduction due to the presence of abrasive) is:

$$V_w = \frac{V_{wo}}{1+\frac{y}{\Gamma}(1-\sqrt{1-(\nu-1)^2})}$$

where y is the semi-minor axis of the elliptical contour of the nozzle, Γ is the nozzle radius, and ν is the fractional distance through the nozzle.

Numerical methods are employed to solve the above equations for particle velocity. The results are graphed in figure 2.16. It can be seen that the particle lags the water velocity considerably.

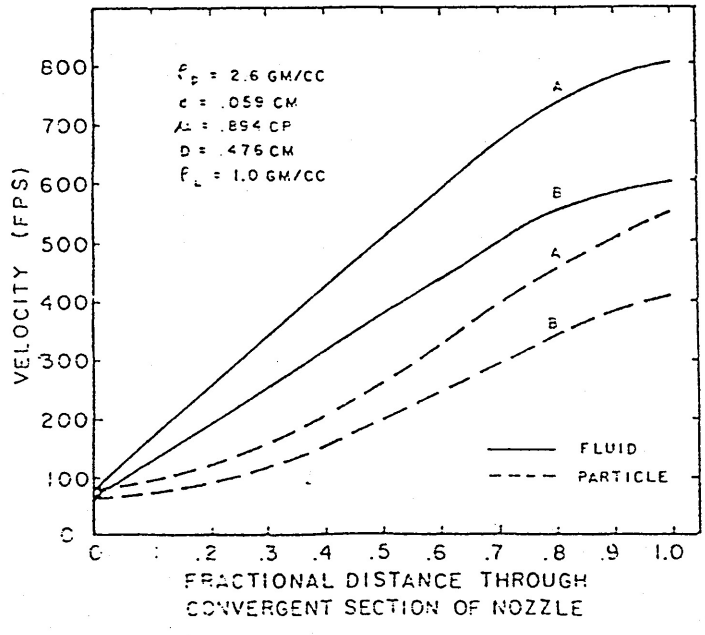

Figure 2.16 Velocity increase through the convergent section of a nozzle [12]

2.3.6 Nadeau, Stubbley, and Burns

Nadeau et al. also report investigations of the momentum transfer between the two phases occurring as a result of drag forces at the interfaces [86].

If the jet is highly turbulent then the velocity variations across the cross-sectional area can be neglected. Assume the processes within the mixing tube are locally steady.

The respective mass flow rates of abrasive is given by:

$$\dot{m}_w = (1-\alpha_a)\rho_w A v_w \qquad \text{and} \qquad \dot{m}_a = \alpha_a \rho_a A v_a$$

where α_a is the local void fraction of abrasive, V_a per unit total volume of mixture.

Conservation of mass within the nozzle is given by

$$\Sigma \dot{m} = A(\alpha_a(\rho_a v_a - \rho_{wv_w}) + \rho_w v_w) = Const$$

It can be seen that, as v increases A must decrease, also α must decrease.

Equation of motion

Assuming no particle-particle or particle-wall interaction, the equation of motion for the abrasive particle is:

$$\dot{m}_a \frac{\partial v_a}{\partial x} = B_a$$

where x is the distance along the mixing tube and B_a the interphase momentum transfer term. The corresponding equation for the water is:

$$\dot{m}_w \frac{\partial v_w}{\partial x} = -B_a - S$$

where S is the wall shear stress. For distances sufficiently down the mixing tube, the abrasive and water velocities will become equal.

Considering the initial and this final position (infinity)

$$v_{a\infty} = \frac{\dot{m}_w v_{a0} + \dot{m}_a v_{a0}}{\dot{m}_w + \dot{m}_a}$$

Interphase momentum transfer equation is modelled as [57]:

$$B_a = \frac{3}{8}\alpha_a \rho_w A \frac{C_D}{r} |v_w - v_a| (v_w - v_a)$$

where r is the effective radius of a single abrasive particle and C_D is the equilibrium drag coefficient for a uniform flow of water over a *single* sphere.

For flow over a uniform sphere, Nadeau uses the equation:

$$C_D = \frac{24}{Re} + \frac{6}{1 + \sqrt{Re}} + 0.4, \quad Re < 2.0x10^5$$
$$= 2, \quad Re > 2.0x10^5$$

where $Re = 2\rho_w r \frac{|v_w - v_a|}{\mu_w}$ is the Reynolds number of the relative motion between the water and the abrasive; and μ_w is the effective viscosity of the water.

Nadeau comments that B_a above is a simple equation, neglecting: "virtual mass" drag when the relative acceleration between the water and the abrasive becomes large. The drag coefficient of a sphere in a mixture of fluid and spheres is slightly different. In particular, the high Re number drag coefficient and the effective viscosity of water depends on the abrasive void fraction.

Figure 2.17 shows the results. The inclusion of fluid deceleration accounts for approximately 7% of the velocity decrease in the fluid, in this case.

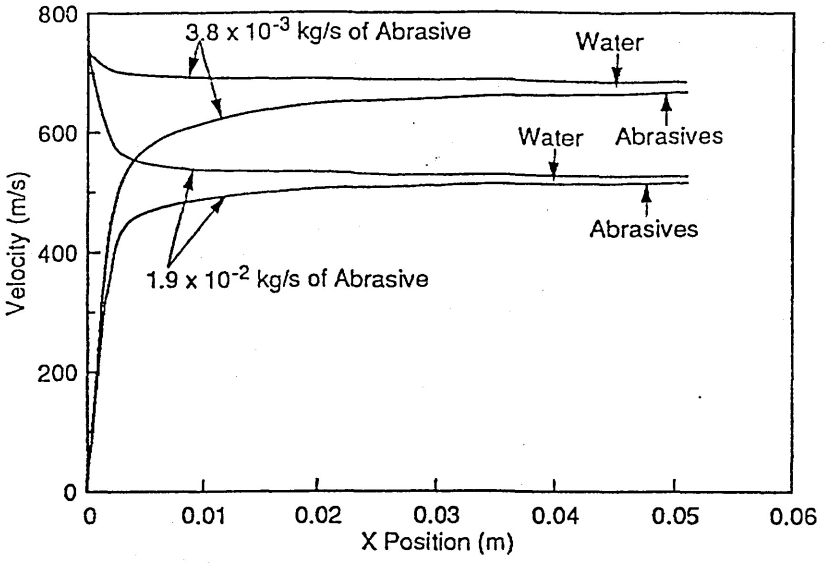

Figure 2.17 Velocity through a nozzle [86]

2.3.7 Benchaita, Griffith, and Rabinowicz

Benchaita et al. studied the erosion of copper plate by a wall jet containing abrasives [87]. The particle trajectory through the wall jet was modelled. Such a situation would arise in trying to cut a piece of material at high speed or the initial stages of piercing, resulting in a very shallow depth of cut and a wall jet. Its inclusion is because of the observations on particle jet interaction.

The flow model of the jet is divided into the three regions shown in figure 2.18 :

- an incoming parallel and uniform flow from the exit plane of the nozzle down to the position $y = y_{fs}$
- a streamlined jet flow where the component of the liquid velocity is given by the following equations:

$$U = Mx$$
$$V = -My$$

where (x,y) are the system coordinates measured from the stagnation point, and M is a flow parameter.

- a uniform and parallel outgoing flow beyond the position $x = x_{fs}$ where the velocity normal to the wall is zero.

A boundary layer starting at the stagnation point is given by:

$$\delta_e \approx 2.4\sqrt{\frac{\nu_1}{M}}$$

M is dependent on the jet velocity, the nozzle diameter, and the stand-off distance. Particle sizes less than this boundary layer thickness will suffer deceleration effects.

The equations of motion for a particle in a two dimensional impinging jet are given by:

$$m_p\ddot{x} = \frac{C_D}{2}\rho_w A_p(U-\dot{x})[(U-\dot{x})^2 + (V-\dot{y})^2]^{.5}$$

$$m_p\ddot{y} = \frac{C_D}{2}\rho_w A_p(V-\dot{y})[(U-\dot{x})^2 + (V-\dot{y})^2]^{.5} - \frac{\pi}{6}d_m^3(\rho_p-\rho_w)g$$

where A_p is the projected area of the particle.

Including forces for the particle/material interaction and the virtual mass term, Benchaita derives a model of particle erosion versus distance from the centre of impact of the jet.

The most important finding of the study is the effect of the deflecting jet on different particle sizes. A plot of particle trajectory versus size is shown below, figure 2.19. For the 20 mm diameter jet considered, particles below 200 microns do not even interact with the target. In this case the boundary layer thickness is calculated as 120 microns. For a plane wall jet, the boundary layer thickness is approximately 0.014x, where x is the distance from initial contact with the surface [88]. For a depth of 10 mm this yields a boundary layer thickness of 140 microns. Thus with increasing depth, smaller particles will be less influential in material erosion as they are washed away from the surface by the deflecting jet.

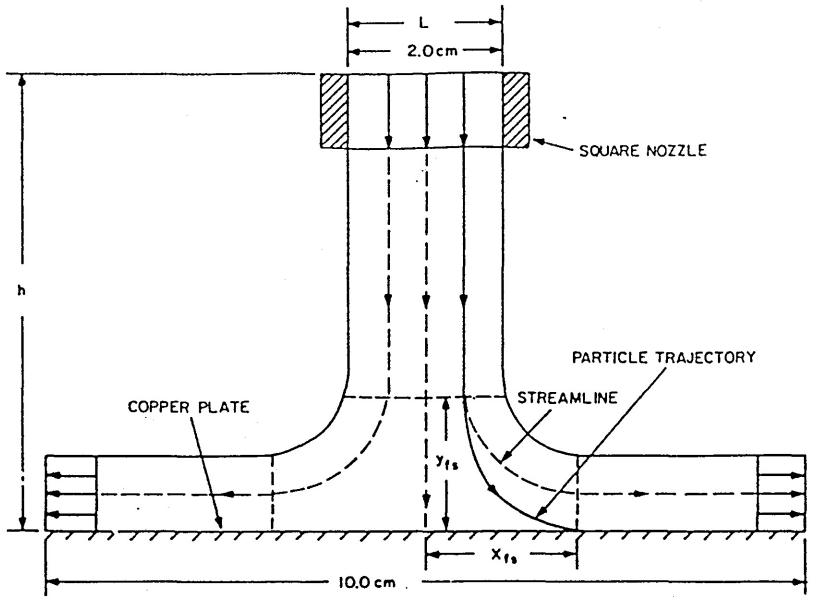

Figure 2.18 Impinging abrasive water jet [87]

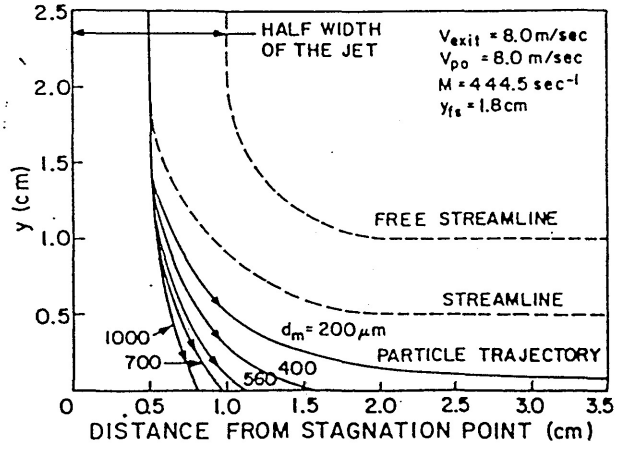

Figure 2.19 Particle trajectory in an awj [87]

CHAPTER 3 - MODEL OF ABRASIVE WATER JET CUTTING

The following model of abrasive water jet cutting of materials is developed from the premise that both cutting wear and deformation wear take place, similar to that of Hashish [7]. This, in turn, has been based on the pioneering work carried out by Bitter on erosive wear by solid particle impact, augmented by an improved model of cutting wear [51].

The process of abrasive water jet cutting is assumed to be a combination of steady wear due to particle impacts at shallow angles (causing cutting wear, where a particle gouges out some material) and unsteady wear by particle impacts at large angles (deformation wear, as a result of particles causing work-hardening and subsequent fracture of the material). Figure 3.1 depicts the abrasive water jet cutting of material. The unsteady deformation wear can be seen in action towards the bottom of the material, eroding material in a series of steps.

The model is being developed primarily for ductile materials, but should be valid for brittle materials. In this case, only deformation wear will occur. It is possible that small particles can cause some cutting wear in brittle materials [22]. This would then cause a loss of accuracy dependent on the abrasive being used.

The influence of the system will be included by calculating the particle exit velocity. Previously, velocity was incorporated by assuming a simple relationship dependent on specific density of the abrasive and the mass loading (concentration). This approximation is [89]:

$$V_0 = C_{vs} V_j \frac{s+r}{s(1+r)} \qquad 3.1$$

where V_0 is the particle velocity, C_{vs} is the coefficient of velocity for the slurry mixture, V_j is the water velocity, s is the ratio of abrasive to water densities, and r is the mass loading ratio by weight. However, from the work carried out on developing a model of particle acceleration (section 3.2) the particle velocity is more accurately given as the theoretical velocity of a two-phase mixture through the nozzle.

The cutting effect due to the stagnating water jet will be ignored. Although this is sufficient to cut materials such as rock and stone, aided by cavitation effects, its contribution relative to the abrasive particles has been shown to be negligible [7].

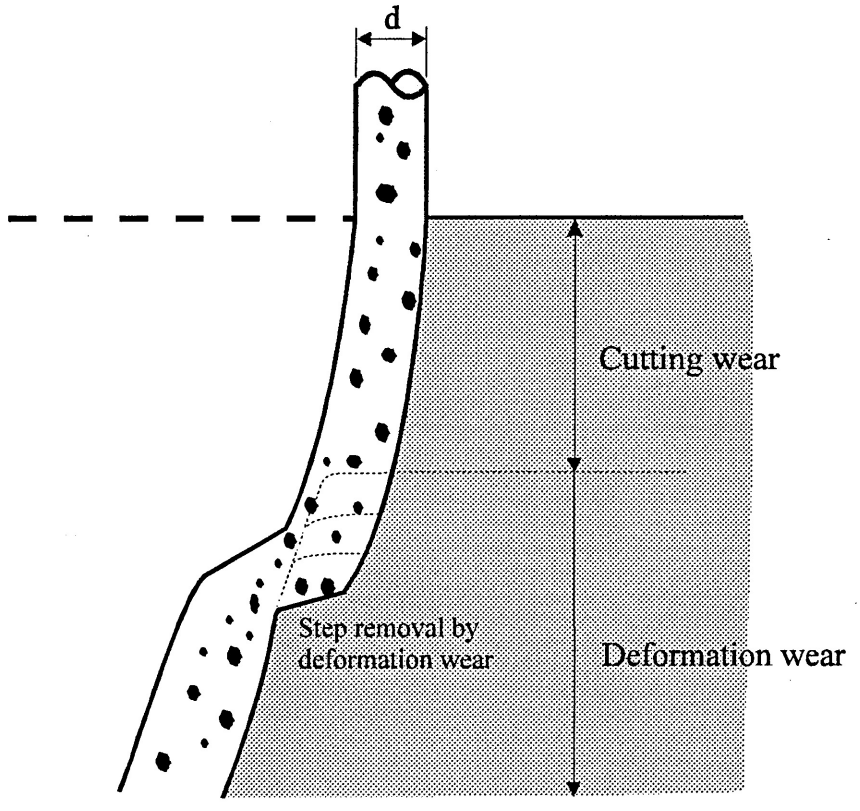

Figure 3.1 Abrasive water jet cutting

3.1 Cutting wear

Cutting wear, as discussed in section 1.3, is similar in nature to the action of a single grain in a grinding wheel, or a v-point cutting tool. The process is one of shallow particle impacts gouging out material.

The model chosen here is that of Hashish [7], modified to include the threshold velocity. Section 1.3 details the development of the model. Hashish improved on the original model of Finnie and McFadden by taking into account particle shape during the cutting process, (section 2.1.6). Figure 3.2 depicts the erosion process.

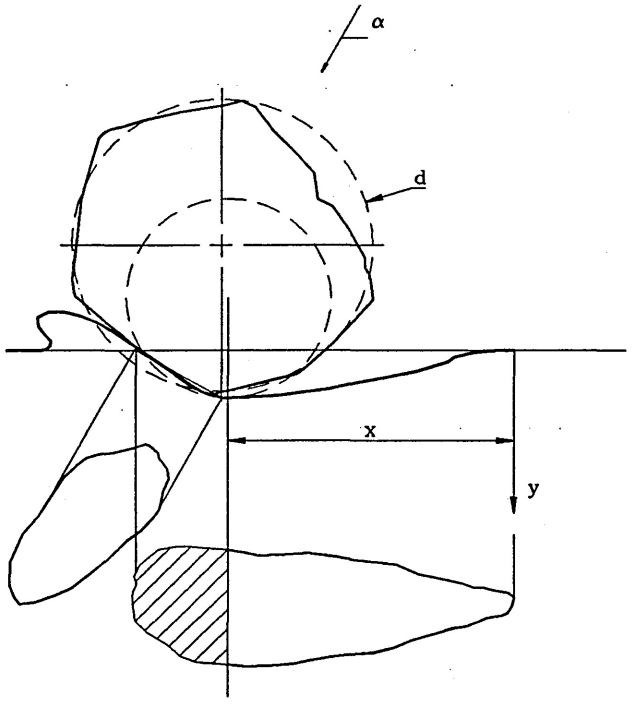

Figure 3.2 Erosion by shallow particle impact

The resulting model predicts the volume erosion of material for shallow angle of impacts to be [51]:

$$\delta v = \frac{7}{\pi}\frac{m}{\rho_p}\left(\frac{V}{C_k}\right)^{2.5}\sin 2\alpha\sqrt{\sin\alpha} \qquad 3.2$$

where

$$C_K = \sqrt{3\sigma\frac{R_f^{.6}}{\rho_p}} \qquad 3.3$$

C_K is the characteristic velocity. This is dependent on the abrasive particle shape and density as well as the material strength. The predictions of this model yield an erosion dependency on velocity of 2.5, which agrees with most experimental findings for low angle impacts [25].

By analogy with the equation for deformation wear [1], the velocity effective in removing material is the surplus over the required threshold velocity to initiate shear. Including this threshold velocity V_e and noting that the particles' velocity relative to the surface is $V\sin\alpha$, that $\sin 2\alpha \approx 2\sin\alpha$ and $\cot\alpha \approx 1/\sin\alpha$ for small angles, the equation for cutting wear becomes:

$$\delta v = \frac{14}{\pi}\frac{m}{\rho_p}\left(\frac{V\sin\alpha - V_e}{C_k}\right)^{2.5}\cot 2\alpha \qquad 3.4$$

Assuming that the abrasives are uniformly distributed over the cross-sectional area of the jet, we can write:

$$dm = \dot{m}\frac{dx}{d} \qquad 3.5$$

where d is the jet diameter (figure 3.1).

For the steady state cutting during this wear mode the material erosion rate will equal the volume of material removed to the depth dh, $\delta\dot{v} = dh\ u\ w$ where w is the width of the cut at depth h, assumed equal to the jet diameter. Incorporating these factors into equation 3.3 above yields:

$$\frac{dh}{dx} = \frac{14m}{\pi\rho_p u d^2}\left(\frac{V\sin\alpha - V_e}{C_K}\right)^{2.5}\cot\alpha \qquad 3.6$$

From the initial condition that α (= dh/dt) = α_t at h = 0, α_t may be calculated assuming $\sin\alpha \approx \alpha$, yielding:

$$\sin\alpha_t = \frac{V_e}{V_o} + \frac{1}{\left(\frac{14m}{\pi\rho_p u d^2}\right)^{2/5}\left(\frac{V_o}{C_K}\right)} \qquad 3.7$$

From visualisation studies, the cutting wear depth is relatively small and therefore the decrease in particle velocity due to frictional drag may be ignored [51].

The development of the cutting face during cutting wear is a very complex matter. This is complicated by the changing flow pattern as the cutting front develops. Although visualisation trials have shown the steady state shape to be parabolic [90], this does not ease the complexity, as the particle trajectory within the deflected jet is unknown.

Assuming a linear relationship for the change in impact angle over the dimeter of the jet. Thus $\alpha = \alpha_t\left(1 - \frac{x}{Cd}\right)$, where C is a fraction to account for the case when the cutting mode terminates with only partial involvement of the jet, figure 3.3. C will be strongly dependent on α_t, the impact angle at the top of the cut surface, and α_0, the transition angle between cutting wear and deformation wear. When the angle at the top of the cut is very small, C is 1. When $\alpha = \alpha_0$, C will be zero. The simplest case is to consider C to vary linearly between these two values, yielding:

$$C = 1 - \frac{\alpha_t}{\alpha_0}, \quad \alpha_t > \alpha_0 \qquad 3.8$$

The value for the transition angle has been determined as [91]:

$$\tan\alpha_0\sqrt{\sin\alpha_0} = \frac{3\pi R_f^{0.6}}{14\gamma}\sqrt{\frac{C_K}{V_0}} \qquad 3.9$$

where $\gamma = 1 + mr^2/I$, I being the moment of inertia of the particle.

From the assumption that the particles are uniformly distributed over the area of the jet, the percentage of the particles participating in cutting wear will be proportional to the percentage area in the chord of width C (the proportion of the jet diameter assumed involved in cutting wear). Thus, the mass of abrasive contained within the area contained within a chord of width Cd is (figure 3.3):

$$A_c = \frac{1}{2\pi}(\theta - \sin\theta)$$

where $\theta = 2\,acos\,(1 - 2C)$

Based on the fact that the cutting wear depth is quite small, the impact angle will not vary significantly over this depth. This is verified by the typical values given for cutting wear mode [2]. Therefore, it is reasonable to assume that the cutting wear depth is approximately given by the opposite side of a right angle triangle, whose adjacent side is the length of jet involved in the cutting wear (Cd) and whose hypotenuse is subtended from the adjacent by the angle α_t. Thus:

$$h_c = C\,d\,\cot\alpha_t \qquad 3.10$$

Combining the above equations gives the equation for the depth of the cutting wear mode to be:

$$h_c = \frac{(\frac{V_e}{C_K})Cd}{(\frac{\pi\rho_p u d^2}{14A_c m})^{2/5}\cdot(\frac{V_e}{C_K})} \qquad 3.11$$

This equation only holds true for $V_e < V_0 \sin\alpha$ i.e. assuming that the particle has sufficient velocity (energy) to cause permanent deformation of the material.

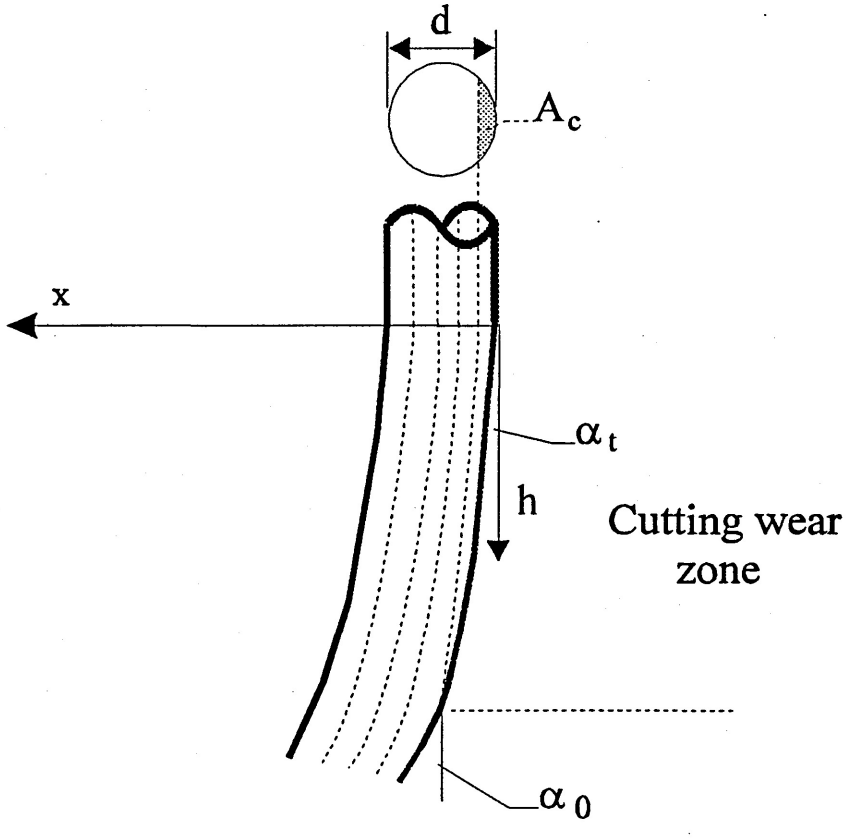

Figure 3.3 Cutting wear parameters

3.2 Deformation wear

For near normal impacts, the equation proposed by Bitter [1] will be used, namely:

$$\delta v = \frac{m(V-V_e)^2}{2\sigma} \qquad 3.12$$

In this case, the depth of cut is sufficiently large for the velocity decrease due to drag to be significant. However, the assumption of a non-divergent jet will be retained.

Considering an idealised, cylindrical, control volume bounded by the jet/ kerf wall interface, and the jet entry and exit in the deformation cutting zone this value can be determined from the conventional friction force.

The momentum equation for the control volume is: $\dot{m}v = \dot{m}v_0 - F_f$ where the frictional drag is written as $F_f = C_f A_w \frac{\rho v_0^2}{2}$. The area of contact is approximately π d h and thus

$$F_f = \frac{C_f \pi}{2} dh \rho v_0^2 \qquad 3.13$$

This value of frictional drag is equal to the product of the pressure loss due to friction and the projected area, namely $F_f = \Delta p \frac{\pi d^2}{4}$

Equating both yields: $C_f = \frac{\Delta p d}{h \rho v_0^2}$ i.e. C_f is the piping loss frictional drag. For the case of a 69 MPa DIAJET system with a 0.4 mm nozzle a Reynolds number of 10^5 is calcuated. Modelling the kerf wall as a smooth pipe then gives a value of C_f of 0.016. For a 0.53 mm nozzle the value is 0.017.

Noting that F_f can be rewritten as $\frac{C_f \dot{m}}{d}$ and the particle velocity through the deformation depth is given as: $V = V_0(1 + \frac{C_f}{d})$

For the deformation cutting, one can assume that all the particles make a contribution, ie that the proportion of particles taking part in the cutting wear mode ($A_c M$) have been re-

entrained and accelerated to the velocity of the jet. This assumption requires that the depth of the deformation wear zone is much greater than the particle size, allowing sufficient distance for the particles to be re-accelerated.

Incorporating this velocity decrease of the particles due to wall drag, the volume of material removed can be written as:

$$\delta v = \frac{\dot{m}}{2\sigma}\left(V_0(1-\frac{C_f}{d}h)-V_e\right)^2$$
$$= \frac{\dot{m}}{2\sigma}(V_0-V_e)^2(1-\frac{C_f}{d}q\,h)^2$$
$$\text{where} \quad q = \frac{V_0}{V_0-V_e}$$

The volume removal rate at the step at a depth h is then the product of the step area (assumed equal to the cross-sectional area of the jet) and the penetration rate:

$$\delta\dot{v} = A_c\frac{dh}{dt} = \frac{\pi}{4}d^2\frac{dh}{dt} \qquad 3.14$$

Equation 3.12 can be combined with 3.14, re-arranged and integrated to calculate the deformation wear depth. As frictional drag was ignored for the cutting wear zone, the velocity at the start of the deformation wear zone is assumed to be V_0, and the limits of integration on the left hand side can be 0 to h_d rather than h_c to h_t, the latter being the total depth of cut. This integral is:

$$\int_0^{h_d}\frac{dh}{(1-\frac{C_f}{d}q\,h)^2} = \frac{2\dot{m}(V_0-V_e)^2}{\pi\sigma d^2}\int_0^t dt \qquad 3.15$$

The upper limit of integration on the right-hand-side of 3.15 is the time of cutting, which in this instance will be equal to u/d_j. Integrating yields the deformation wear zone depth as:

$$h_d = \frac{1}{\frac{\pi d\sigma u}{2\dot{m}(V_0-V_e)^2}+\frac{C_f V_0}{d(V_0-V_e)}} \qquad 3.16$$

3.3 Threshold particle velocity

From studies of the elastic impact of spheres on flat surfaces, Hertz [72] calculated the maximum contact force, and radius of projection to yield an average surface pressure of:

$$P_{av} = \frac{F_{max}}{\pi r_e^2} = \frac{2}{3}\left[\frac{40}{\pi^4}\rho_p\left(\frac{1-\nu_1^2}{E_1}+\frac{1-\nu_2^2}{E_2}\right)^{-4}\right]^{0.2} v^{0.4}$$

This average pressure is, according to Hertz, two-thirds the maximum surface pressure. Therefore the elastic limit is reached when the average pressure reaches two-thirds of the stationary elastic yield strength of the material σ_y. Putting this information into the above equations yields a minimum particle velocity to cause plastic deformation of a flat surface of:

$$V_{el} = \frac{\pi^2}{2\sqrt{10}}\frac{\sigma_y^{2.5}}{\rho_p^{0.5}}\left[\frac{1-\nu_1^2}{E_1}+\frac{1-\nu_2^2}{E_2}\right]^2 \qquad 3.17$$

The significance of this value is the existence of a particle velocity (and hence operating pressure) below which no erosion (or cutting in this case) can occur. This fits in well with the experimental findings [54] that a minimum pressure is necessary before any cutting of mild steel could commence. The actual value chosen for material strength is discussed in the following section.

3.4 Material properties

One problem that has arisen in all the mathematical models of abrasive water jet cutting (and erosive wear) encountered is the ability to incorporate material properties to distinguish between materials.

Cutting wear, as described by Finnie [2], involves a process similar to metal cutting by single point tools. Material considerations for cutting wear arise from the calculation of the characteristic velocity, equation 3.14, and the threshold velocity in equation 3.17 above.

The value of material stress pertaining to the cutting of annealed metals has been experimentally determined as inversely proportional to the Vickers Hardness of the material [91]. Any previous work-hardening was found not to affect the erosion rate due to the high strains produced by the particle impacts. This inverse relationship with material hardness was separately confirmed for face-centered cubic steels, such as the austenitic steels 304L, and mild steel used during these cutting trials. However, body centered tetragonal (martensitic) and hexagonal metals do not exhibit the same behaviour [92]. 17-4 PH is a martensitic stainless steel which, although almost twice as strong as 304L, is as easy to machine by conventional methods such as turning.

For deformation wear, the threshold velocity, as calculated by Bitter, is that which just causes plastic deformation. This value of threshold velocity is proportional to between 1.5 and 3.2 times the stationary value of yield strength [1]. This stationary yield strength is taken as the yield strength at which the erosion process has become steady, i.e. workhardening and material removal taking place at a steady rate. Simplistically, this will be the ultimate tensile strength, as the material yield strength can only be increased to this value through work-hardening.

The experimentally determined ratio of cutting performance has been shown to be similar to the inverse ratio of tensile strengths of ductile material [93]. A relationship between cutting performance and tensile strength has also been noted from a comparison of the table of performance coefficients [94] and the table of machinability numbers quoted by Kim [84]. In addition, experimental evidence suggests the harness of a material is proportional to the tensile strength rather than the yield strength [95].

Therefore a single value of threshold velocity, applicable to both wear modes, can be used. This value will be 3.2 times the tensile strength, the maximum value quoted by Bitter and similar to the approximation for an ideally plastic material of $H_v = 3\ \sigma$.

The equation for threshold velocity was calculated assuming only elastic deformation. The remaining energy (velocity) is expended in both deforming the material plastically, during the work-hardening stage, and fracturing the material. Using the tensile strength in calculating the threshold velocity, above, is equivalent to calculating the energy required to fully work-harden the material. The remaining particle energy (V - Ve) is then used for fracture alone, and hence the model should be more accurate than if the yield strength had been used.

The actual material removal mechanism in deformation wear is the fracturing of the surface previously work-hardened by particle impacts. The material property governing the fracture of the material is the reduced modulus of elasticity of the material [1]. The theoretical value of this property is proportional to the Young's modulus of elasticity. The constant of proportionality depends on type of fracture ooccurring.

Fracture is the separation, or fragmentation, of a solid body into two or more parts under the action of stress. The process of fracture can be considered to be made up of two components, crack initiation and crack propagation. For the purposes of this study, fractures can be classified into two general categories, ductile fracture and brittle fracture. A ductile fracture is characterised by appreciable plastic deformation prior to and during propagation of the crack. An appreciable amount of gross deformation is present at the fracture surfaces. Brittle fracture in metals is characterised by a rapid rate of crack propagation, with no gross deformation and very little microdeformation. It is akin to cleavage in ionic crystals [96].

Brittle fracture of material is the breaking of ionic bonds, and is characterised by little or no plastic deformation. From considering the energy required to completely separate these bonds, Griffith [97] calculated the theoretical maximum stress as:

$$\sigma_{max} = \frac{E}{10} \qquad 3.18$$

Ductile fracture involves the plastic deformation of the material, and is thus related to the shear deformation properties of the material. It is effectively the sliding of layers of atoms over each other. The theoretical maximum shear strength of the material can be shown to be [98]:

$$\tau_{max} = \frac{1}{2\pi} G$$

where G is the shear modulus of the material. This theoretical maximum value is reduced in practice due to increased resistance to dislocation travel caused by strain hardening effects increasing the strength as dislocation bundling together, precipitation hardening, and fine grains having increased grain boundary area.

For metals in general, the following relationship between Shear and Youngs modulus holds:

$$G \approx \frac{3}{8} E$$

thus

$$\sigma_{max} = \frac{E}{16.8} \qquad 3.19$$

Although the surfaces cut by an abrasive water jet show no real sign of plastic deformation, very soft materials can exhibit a burr on the bottom of the cut surface. In considering the fracture mechanism in these materials, it may be necessary to apply the value for ductile fractures.

3.5 System effects - calculation of particle velocity

Models and experimental results of erosion and abrasive water jet cutting have shown the critical dependence of these areas on the particle velocity as discussed in section 2.3. However, existing work seems to suggest that short parallel sections of standard DIAJET nozzles (~ 10 diameters) would allow the particles to achieve only 80% of the water velocity [8,12].

Multiphase flow is the simultaneous flow of several phases (states of matter, solid liquid or gaseous). In order to solve the motion of one phase relative to the other it is necessary to

use a separated flow model, allowing different properties (velocity etc.) for each phase. The majority of the models consider only the Stokensian drag force in deriving the particle velocity. In addition, one finds that the conservation of mass is not treated correctly for the mixture as a whole.

A review of two phase flow phenomena revealed more detailed forms of the interphase forces, mentioned in section 1.6. These, in general, come from simplifications applied to the Navier-Stokes equations for a single particle and often incorporate experimental parameters to account for multiple particle and wall effects.

However, in considering the practical situation of multiple particles and wall effects, the over-all flow can be modelled analytically by homogenous methods, treating the phases as a sort of pseudo-fluid. This leads to a modified value of viscosity and density, for instance.

One such equation will be used here [65]. The derivation of the equation of motion, based on the analysis by Maxey and Riley, is given in appendix B. The derivation comprises solutions to the Navier-Stokes equation for the forces caused by the insertion of the single particle in the flow field, as well as the forces arising from the undisturbed flow field. The forces arising out of this equation are discussed below. The complete equation of motion for the particle is given as:

$$
\begin{aligned}
m_p \frac{dV_i}{dt} &= (m_p - m_F) g_i + m_f \left. \frac{Du_i}{Dt} \right|_{Y(t)} \\
&- \frac{1}{2} m_f \frac{d}{dt} \left[V_i(t) - u_i[Y(t),t] - \frac{1}{10} a^2 \nabla^2 u_i \Big|_{Y(t)} \right] \\
&- 6\pi a \mu \left[V_i(t) - u_i[Y(t),t] - \frac{1}{6} a^2 \nabla^2 u_i \Big|_{Y(t)} \right] \\
&- 6\pi a^2 \mu \int_0^t d\tau \left(\frac{d/d\tau \left(V_i(\tau) - u_i[Y(\tau),\tau] - \frac{1}{6} a^2 \nabla^2 u_i |_Y(t) \right)}{\sqrt{\pi \nu (t-\tau)}} \right)
\end{aligned}
\qquad 3.20
$$

3.5.1 Description of the forces arising

Buoyancy.

The first term on the right-hand-side of equation (3.20) is simply the buoyancy force. In the following numerical evaluation this will be ignored.

Undisturbed flow force.

The second term accounts for the undisturbed flow. From the simplified Navier-Stokes , $\rho\frac{DV}{Dt} = \rho g - \nabla p + \mu\nabla^2 V$ and combining the second part of the fourth term above, we can

rewrite these terms to give these accelerations as:

$$-\frac{1}{\rho_p}\frac{dp}{dx} + \frac{7}{3}\frac{\mu}{\rho_p}\nabla^2 u_t^F$$

Apparent mass.

When a particle is accelerated relative to a surrounding fluid it sets up a two dimensional flow around it which posses kinetic energy. Therefore work must be supplied to move the particle, in addition to that which is required to accelerate it alone. This shows up as an additional force on the particle.

The sphere behaves as if it possessed an additional "apparent mass" equal to one-half of the fluid which it displaces [99]. Bodies of different shapes have different values of apparent mass, ranging from 0.045 to 0.5

Allowing for the effect of other particle, Zuber suggested the apparent mass term be modified by the factor $\frac{1+2\alpha}{1-\alpha}$ where α is the volume fraction of particles present [100].

This relative force will act to reduce the velocity lag. In effect, this will shorten the required length of nozzle for optimum velocity. In addition, this term will have greatest effect in the entrance section, where the values of acceleration are the greatest.

Stokes drag.

The fourth term is the familiar Stokes drag force, normally predominant at low values of Reynolds number. The second part of this force arises from the inclusion of velocity gradients in the flow field by the presence of the particle itself.

The Basset force.

When a particle is accelerated relative to a fluid it establishes not only a potential flow field, but also a viscous flow field. Since viscous effects, such as boundary layer growth, are governed by diffusion equations, the instantaneous flow field is thus a function of the entire previous history of the particle motion. This gives rise to the Basset force, again augmented by a component for the non-uniformity of the flow field.

3.5.2 Continuity equations

Applying conservation of momentum across a volume (of uniform length) yields

$$\frac{\partial \left[\rho f u + \rho_P (1-f)\, u_p \right] A}{\partial x} = 0 \qquad 3.21$$

where f is the water voidage (percentage volume filled by water as opposed to abrasive). If ϕ is the abrasive concentration, then the voidage fraction is related to it by

$$\frac{fu}{(1-f)u_p} = \frac{1-\phi}{\phi} \qquad 3.22$$

Rearranging yields the volume fraction of abrasive as:

$$f = \frac{(1-\phi)u_p}{\phi u + (1-\phi)u_p} \qquad 3.23$$

Assuming the initial conditions at the convergent section of the nozzle are X=0, $u=u_{p0}=u_o$, $A=\pi R^2$ where u_o is the initial water velocity and R the entrance radius.

The water velocity in the convergent section is then given by:

$$u = \frac{\pi R^2 u_0 (1-\phi) u_p}{R - x \tan\theta} \qquad 3.25$$

Equation 3.25 can then be differentiated to give the required water acceleration.

If the particle velocity is taken as that calculated for the previous position, then the water acceleration can be calculated without recourse to another differential equation consisting of Bernoullis equation, the particle reaction forces, wall drag and the effect of the vena-contacta.

In the parallel section of the nozzle, the water deceleration is calculated from the wall drag and particle reaction forces. From a study of laminar pipe flow the conditions in the nozzle would yield a percentage pressure drop in the parallel section equal to the co-efficient of friction per diameter length (about 1.5% total pressure). For the turbulent conditions here this value would be much greater. Thus a rapid velocity decrease from this opposing force alone is to be expected.

3.5.3 Practical considerations

By modelling the multi-phase flow analytically by homogenous methods, the whole flow is treated as a sort of pseudo-fluid. This gives rise to apparent, or bulk, values for the properties of the mixture. Of chief concern here are the density and viscosity of the mixture. The velocity through a nozzle is calculated, from Bernoullis equation as $V_w = C_v \sqrt{\frac{2P}{\rho_w}}$. For the mixture, the apparent viscosity of the fluid is given by $\rho_m = (1 - \phi)\rho_w + \phi\rho_a$ where ϕ is the volume fraction of abrasive present.

The effect of the presence of additional particles and wall effects arise due to the inability of the solid (boundary/particle) to take part in the deformation of the flow field induced by the motion of a single particle. This influence, i.e. resistance to motion, appears as a change in viscosity, which then becomes a function of the concentration.

The effect of suspended rigid particles on the apparent viscosity, μ, of a two-phase mixture was first derived by Einstein as [101]:

$$\mu_m = \mu_w(1+2.5\alpha)$$

for low concentrations by volume i.e. $\alpha<0.05$.

3.6 Prediction of abrasive particle velocity

The abrasive particle velocity is predicted from the differential equation 3.20. In order to solve this numerical methods must be used. In this case a fourth-order Runge-Kutta numerical approximation with adaptive step-size was used, and the resulting procedure was programmed using Turbo-Pascal for Windows. A summary of the procedure is given below:

1. A procedure is written to return the derivative dy/dx at a given x and y. This procedure uses equations 3.20 and the derivative of equation 3.25 to calculate the velocities for the water velocity and particle velocity respectively.
2. The initial values of water and abrasive velocity, as well as parameters such as nozzle geometry, are assigned to variables.
3. A driver routine is called to calculate the velocity at small increments along the length of the nozzle starting from the inlet, with the initial values.
4. This routine calls the fourth-order Runge-Kutta method to advance the solution over one increment, h. This is achieved by numerical approximation using the procedure from step 1, above. This initial step size is chosen to be greater than the particle diameter.
5. The values obtained are compared with those at the previous calculation point. If the difference is too large the increment size is reduced and the procedure repeated.
6. The values of velocity calculated, along with their position within the nozzle, is stored in a matrix for plotting or further processing if required.

In this case only the final value, i.e. the exit velocity is of interest. However, it is useful to examine the rise in particle velocity to see the effect of varying inlet geometries for instance.

3.7 Abrasive water jet prediction procedure

The depth of cut can be calculated as follows:

1. Calculate the abrasive particle velocity. This can be calculated by using the mathematical model of the previous section. An adequate approximation, however, is given by approximating the particle velocity to the theoretical water velocity from Bernoullis equation $V_0 = C_v\sqrt{\frac{2P}{\rho_m}}$ where $\rho_m = (1 - \phi)\rho_w + \phi\rho_a$. C_v for the nozzles considered here is usually taken as 0.9.

2. Calculate the material threshold velocity $V_{el} = \frac{\pi^2}{2\sqrt{10}}\frac{(3.2\sigma_{ult})^{2.5}}{\rho_p^{0.5}}\left[\frac{1-\nu_1^2}{E_1} + \frac{1-\nu_2^2}{E_2}\right]^2$

3. The characteristic velocity is given by $C_K = \sqrt{\frac{9.6\ \sigma_{ult} R_f^{0.6}}{\rho_p}}$

4. Calculate the intermediate value $\gamma = 1 + \frac{m r^2}{I}$, where I is the moment of inertia of the particle. For most abrasives γ will be between 3 and 4.

5. The initial impact angle is calculated from $\alpha_t \approx \frac{V_e}{V_0} + \frac{1}{(\frac{14m}{\pi\rho_p u d^2})^{2/5}(\frac{V_0}{C_K})}$

6. The transition angle is given by $\alpha_0 \approx \left[\frac{3\pi R_f^{0.6}}{14\gamma}\sqrt{\frac{C_K}{V_0}}\right]^{\frac{2}{3}}$

7. C, the fraction of the jet diameter involved in the cutting wear mode, is assumed to vary linearly between the initial and the transition impact angles $C = 1 - \frac{\alpha_t}{\alpha_0}, \quad \alpha_t > \alpha_0$

8. This gives the fraction of abrasives involved in cutting wear, i.e. the fractional mass of abrasive contained within the area contained within a chord of width Cd as $A_c = \frac{1}{2\pi}(\theta - \sin\theta)$ where $\theta = 2\,a\cos(1 - 2C)$.

9. The depth of the cutting wear mode is then given by:

$$h_c = \frac{(\frac{V_o}{C_K})Cd}{(\frac{\pi\rho_p\mu d^2}{14A_c m})^{2/5} + (\frac{V_e}{C_K})}$$

This equation only holds true for $V_e < V_0 \sin\alpha$

10. The Reynolds number for the jet is calculated from $Re = \frac{V_0 d}{\nu}$ and this gives the co-efficient of friction C_f from a Moody diagram, assuming the cut path is similar to a hydraulically smooth pipe.

11. The deformation wear depth is then given by:

$$h_d = \frac{1}{\frac{\pi d\sigma u}{2\dot{m}(V_0 - V_e)^2} + \frac{C_f V_0}{d(V_0 - V_e)}}$$

The material stress here is the reduced modulus of the material E/10 corresponding to brittle fracture occuring during deformation wear.

This equation is only valid as long as $V_0 > V_e$. The above model has been programmed into the software package MATHCAD to easily compute the predictions. A sample calculation is shown in Appendix C.

CHAPTER 4 - EXPERIMENTAL PROCEDURES

4.1 Introduction

The experimental work requires assessment of the cutting system performance as well as validation of the model. The primary objective is to validate the mathematical model for cutting performance prediction. This requires not only determining that the assumptions used in developing the model are correct, but also in showing the applicability of the model for a variety of operating conditions.

One major assumption is that the performance is independent of particle size. This can be proven experimentally by carrying out a series of cutting trials with abrasive particle sizes less than 100 μm. Erosion theory suggests that particles less than this value will be ineffective in material removal [22]. However, mathematical validation is complicated by the need to calculate accurately the particle exit velocity, which will vary with particle size. Here the model must prove that the abrasive particles are being incorporated correctly.

Laser Doppler anemometry was employed to attempt to measure the exit velocity of the particle leaving the nozzle. Abrasive water jet cutting trials at different water velocities (i.e. pressures), abrasive particle sizes, concentrations, and densities will also increase confidence in the model of particle velocity by measuring the average discharge rates from the nozzle as well as the inferred effect of erosive power of the particle.

4.2 Abrasive water jet parameters - measurement and control

The actual validation of the mechanism of abrasive water jet cutting model can be verified by testing different materials of different thicknesses at known cutting speeds. This will validate the material and abrasive properties used within the model and the interaction of the two different cutting modes. Another trend to look out for is the shape of the cutting depth versus cutting speed curve; the model developed infers the dominance of the deformation wear mode in determining its shape. Testing two different steels will verify that the correct material properties are being used. Previous models predict similar cutting performance for all steels with similar Young's modulus and elastic yield strength.

Although a large database of cutting results exists at BHR Group for cutting with abrasive water jets, most of this information was obtained from cutting systems using nozzles of 1.0 mm and larger. As the nozzle sizes in this study were less than 0.6 mm it was necessary to devise a complete test programme to verify the model independently. In addition, the systems used to generate the previous cutting data were crude compared to the cutting systems available today, and abrasive flow rates were not as accurately controlled or known as with existing systems.

A summary of the operating parameters of abrasive water jet cutting is given below, and discussed individually in the following sections:

Varying pressure	Effect of particle velocity on cutting performance, effect of abrasive flow rate
Varying cutting speed	Effect of cutting speed on depth of cut
Varying material	Effect of material properties
Different abrasive	Effect of density on particle velocity, effect of particle shape, effect of particle size, effect of abrasive flow rate
Different sieve size	Effect of particle size
Different nozzle diameter	Effect of particle size, effect of abrasive flow rate

4.2.1 Pressure (water velocity)

The operating pressure of the system determines the pressure drop, and hence the maximum theoretical water velocity obtainable for any given system (from Bernoulli's law). The pressure is not constant (see following section on characteristics of pumps used during this project), and hence neither is the velocity. Due to the abrasive environment downstream of the pressure vessel it is normal practice to measure the pressure on entry to the suspension system. The velocity in the pipework and hoses is deliberately low to reduce wear rates, and hence the only significant difference between this measured value and that accross the nozzle is due to the 1 MPa dropped accross the orifice to discharge abrasive.

To check further the pressure during abrasive flow rate calibrations, the volume of water is also measured, giving a further check on the average velocity of the fluid.

4.2.2 Traverse speed

The cutting trials were carried out on a 2-dimensional profiling table. DC servo motors drive a high precision ball screw actuator via a zero backlash reduction gear train. The servo motors are fitted with incremental encoder feedback to achieve a positional accuracy of 0.01 mm. The software allows control of the velocity to within 0.01 mm/min [102]. A photograph of the cutting table is shown in figure 4.1.

Initial linear cutting trials were carried out with a 0.4 mm diameter nozzle. A series of cutting trials were carried out to determine the fastest possible cutting speed for a particular thickness of material. Six cutting speeds were chosen based on previous work and preliminary predictions from the mathematical model. These speeds were refined until the speed which just cut through the material was reached. This proved to be a time consuming and costly way of determining cutting speeds.

This initial test work was carried out as part of the BRITE project running concurrently with my Ph.D. The linear cutting trials were used to define base cutting speeds for each combination of material and thickness. Further cutting trials were carried out at fixed percentages of this speed, as well as at different abrasive flow rates. A standard test shape was cut consisting of a series of radii and internal and external angles in addition to linear segments. The samples produced were then measured for machining tolerances in the form of surface roughness, edge tape, and overshoot. Although a comprehensive experimental test procedure was carried out to generate these data, stored in a database developed using 'Paradox', the results are not directly applicable to the research reported here and thus have been excluded.

In order to carry out the remaining trials as quickly as possible it was decided to carry out just six cutting speeds, chosen so as not to cut through the thickness of the particular material. As before, a straight line was divided into six segments, each programmed for a different traverse speed. The result of this procedure is to produce six slots of varying depth, dependent on the cutting speed. The deflection of the jet when cutting the second or a subsequent slot will cause some erosion of the preceeding slot. Given the inaccuracies caused by inhomogeneity of the material, as well as varying flow parameters, this compromise seemed acceptable. The tests were repeated three times at the higher pressure to provide an average reading.

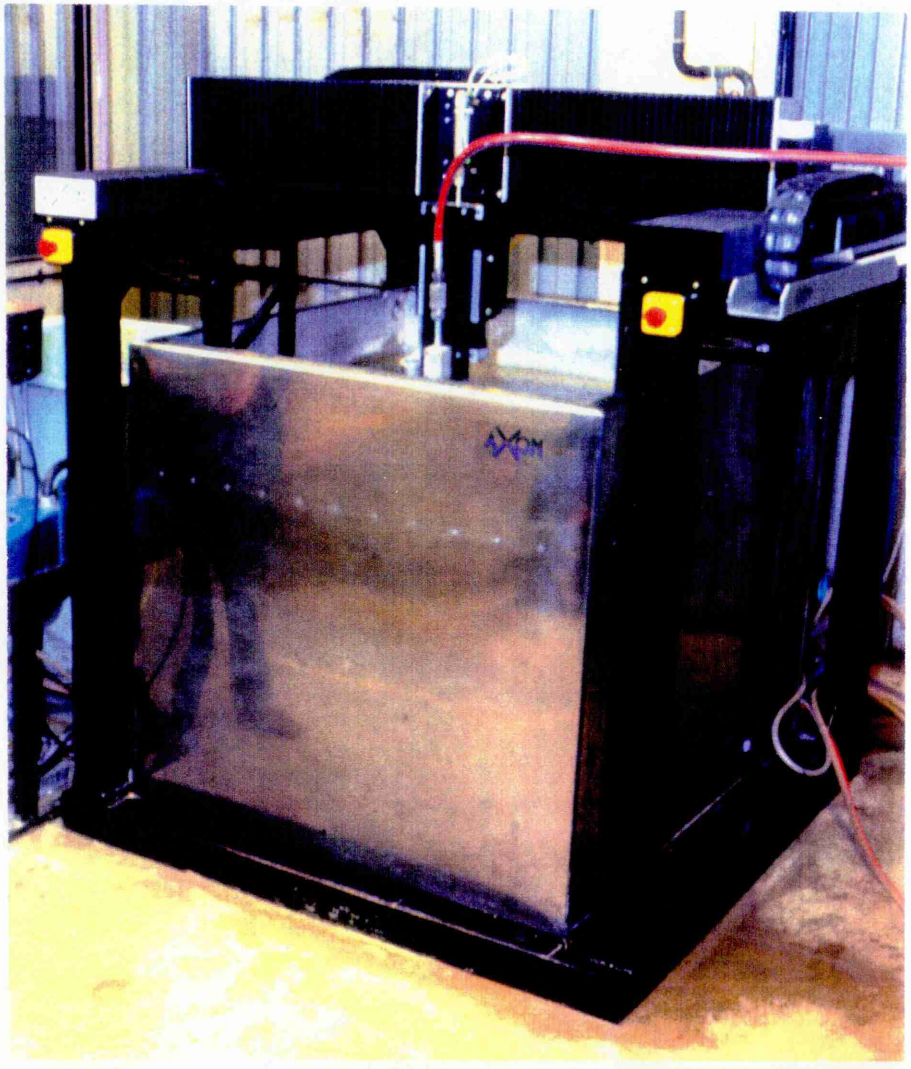

Figure 4.1 AWJ cutting table

4.2.3 Material properties

The proposed model of cutting of ductile materials comprises of two mechanisms of erosive wear, namely cutting wear and deformation wear. The two mechanisms deal with material shearing and deformation (with subsequent fracture) respectively, with two potentially different fracture types. The selected materials will provide analysis of material properties relevant to abrasive water jet cutting. The first choice is of a very ductile material that tends to burr. Aluminium was chosen for this. Additionaly brass was chosen as a ductile material which work-hardens appreciably. From the analysis by Bitter, it is supposed that the degree of work-hardening pre-existing in the material is irrelevant to the actual cutting rate [1]. A list of the material tested, as well as their relevant properties, is given below:

Material	Designation	Yield strength MN/m^2	Ultimate tensile strength MN/m^2	Young's modulus GN/m^2
Brass	CZ108 h-h	125	355	124
Aluminium		40	200	69
Mild steel	AISI 1	207	400	210
Stainless stl	304L	207	544	210
Titanium	TA10	870	1020	116
Marble	white	-	79 (comp)	81

Table 4.1 Material properties

4.2.4 Abrasive material properties

The abrasive material plays an important part in determining both velocity and cutting rate. In the first place, the particle density, shape and size dictate how well it is accelerated over the length of the nozzle chosen. In the second part, the same material properties determine how well the particle will remove material. In addition, it may be necessry to consider the hardness of the material relative to the target material, as well as the existing state of the particles (for example, are they already badly crack-ridden and likely to fracture easily on impact). A table of abrasive material properties is given in section 2.7.

4.2.5 Depth of cut

The depth of the kerf was measured by comparing the penetration depth of a 0.3 mm feeler blade against a rule, graduated in 0.5 mm increments. As the material is not cut fully through, the bottom of the cut is very uneven, varying by approximately ± 0.5 mm. The minimum cut depth was measured by the above method, yielding an error of less than the measurement accuracy. For the purposes of these tests this level of accuracy was considered sufficient.

4.3 Pumping equipment

A number of high pressure pumps was utilised during this project. Their selection was dictated by the availability of pumps at BHR Group as well as recommendations from the test work carried out.

Initially a reciprocating piston (plunger) pump was used. This consists of a motor driving a crankshaft to which three are attached. Although any number of pistons could be used three pistons are the norm, and the pump is generally called a triplex pump. Three pistons are adequate for the pressure pulsation levels required for cutting and cleaning. The pistons may either be radial or axial, and both types of pumps have been used throughout this project.

The initial in-line triplex pump was a Hammelmann pump driven by a fixed speed AC electric motor. Thus the delivery flow rate of 54 l/min at 69 MPa was fixed by the 1450 RPM motor speed. As the full flow was not required, the surplus was dumped via a hydraulically operated unloader (pressure control) valve that regulates the pressure by bleeding off excess flow. As over 90% of the flow was being dumped during these trials, the flow was subsequently directly dumped through another nozzle/orifice.

Triplex pumps, such as the ones used for these trials, have been until recently limited to 69 MPa operating pressure; however, these pumps can now be supplied with operating pressures up to 230 MPa.

To explore the possibility of cutting at higher pressure than the Hammelmann pump could generate, the system was connected to an intensifier pumping system capable of generating 300 MPa. These pumps consist of a low pressure hydraulic (up to 35 MPa) cylinder driving a high pressure cylinder. The area ratio between the pistons gives the required pressure from standard oil hydraulics. Typical operating pressures for commercially available systems is 350 - 400 MPa. To achieve a constant flow two intensifiers are usually used. The standard configuration is to connect these via a double acting hydraulic cylinder to save on component cost, but this setup generates large flow and pressure ripples as each intensifier becomes pressurised. These ripples are caused by the compressibility of the water (almost 10% at 350 MPa). Generally an accumulator is inserted in the delivery line to damp out these fluctuations. Due to the compressibility of the water and accumulator shell at these pressures, and the dangers of highly compressed gas, these accumulators are little more than a miniature vessel, with no internal parts.

A better method of operation consists of two separate, single acting intensifier units. The off-line intensifier, once recharged with water, can be partly stroked to compensate for the compressibility of the water, and therefore give a smoother transition at change over. The independent, single acting intensifier system was used for these trials. Due to reliability problems with these pumps, very few tests were carried out above 69 MPa in any case.

As the performance of the 0.4 mm nozzle DIAJET cutting systems compared almost identically with 250 MPa entrainment systems, this system was chosen as a new product for BHR Group. In order to develop this further, a 69 MPa triplex pump more suited to the flow conditions was sourced. Unlike the Hammelmann pump this was an axial design, delivering 6.7 l/min at 69 MPa. Initially the excess flow was again dumped via the relief valve, but valve failure due to cavitation damage dictated that a variable speed DC thyristor drive was used to deliver the exact flow-rate required Although this is more advantageous due to the problems in sourcing a reliable low flow unloading valve, as well as the power savings, practical considerations of running a continuous system may require an availability of excess flow during re-pressurisation sequences on production systems.

The prototype system used for the majority of the trials used the smaller triplex pump driven by an AC motor and inverter, with pressure providing the feedback for closed loop control of the motor. This pump is shown in figure 4.2. The high pressure trials carried out towards the end of this research used a different double intensifier pump, capable of generating 5 l/min at 250 MPa.

4.4 Abrasive water jet system

A single vessel, manual system was chosen. This was based on the standard DIAJET design, but included modifications suggested by staff at BHR Group to overcome problems encountered in the past. The circuit is described by component below. Figure 4.3 shows a photograph of the system used for the cutting trials. Figure 4.4 is a schematic of the circuit originally devised for the BRITE programme and used throughout these tests.

4.4.1 Abrasive metering control.

Most of the flow from the pump goes directly to the nozzle, by-passing the vessel. Some flow, however, is diverted through a pressure vessel containing the required abrasive. The amount of diverted flow controls the percentage of abrasive discharged. From trials carried out at BHR Group it has been found that approximately 1 kilo of abrasive is discharged from the vessel for every litre of water injected for typical abrasives used for cutting (with specific gravities between 2.6 and 4 - sand and copper slag). This corresponds to a mixture delivered at a concentration of almost 60% by weight of abrasive i.e. packing fraction of the abrasive. Based on these observations, the abrasive flow rate can be assumed to be the bulk weight of wet abrasive displaced from the vessel.

The flow diversion is achieved by placing a restriction in the main flow line and then dividing the flow upstream of this restriction. The discharge from the vessel rejoins the main flow downstream of the restriction. This restriction creates a pressure drop, balanced by an additional check valve in the vessel line and the pressure drop across the abrasive. The inclusion of the additional check-valve allows consistent flow regulation regardless of the amount of abrasive (and hence pressure drop) in the vessel.

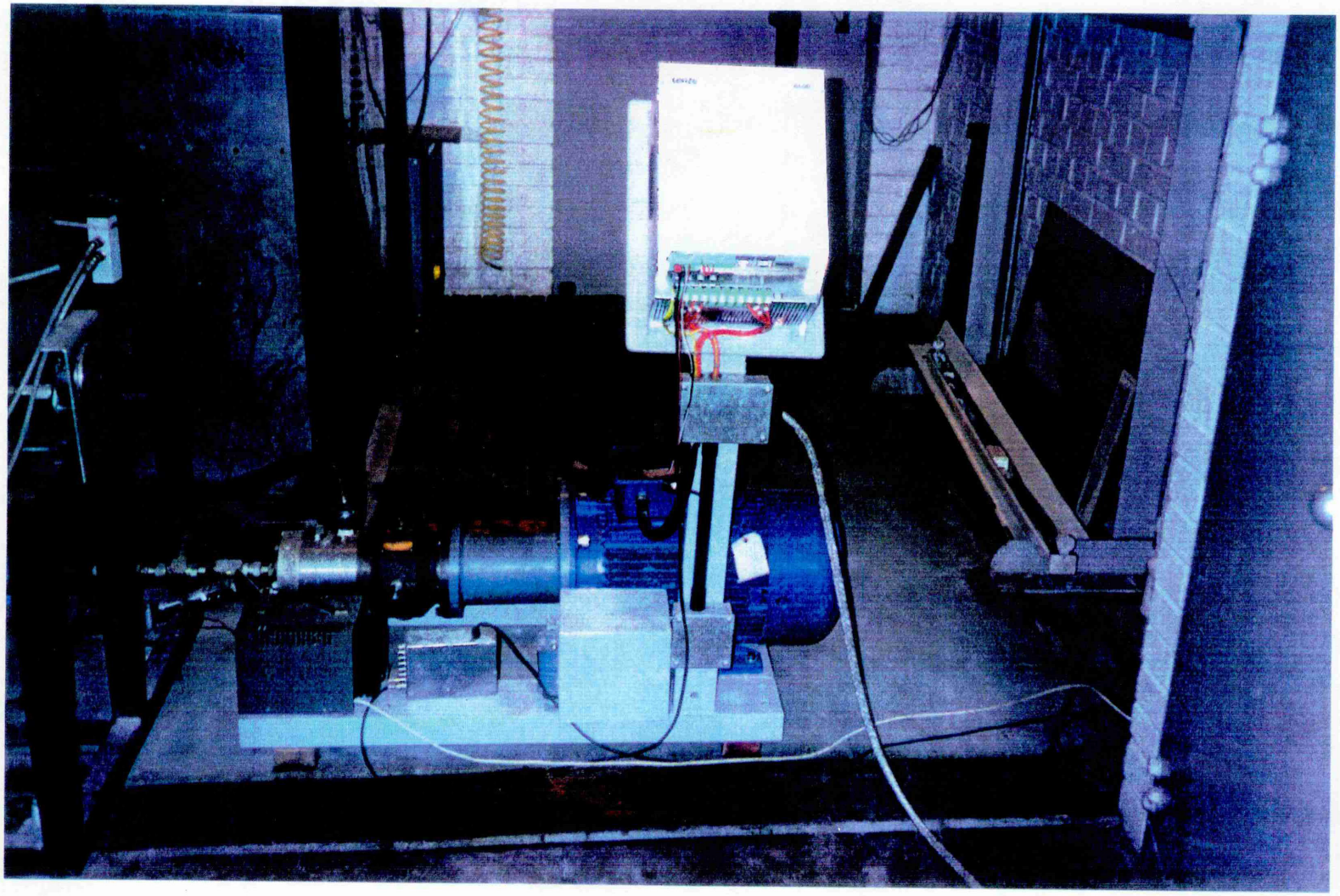

Figure 4.2 High pressure, low flow, pump with AC inverter drive

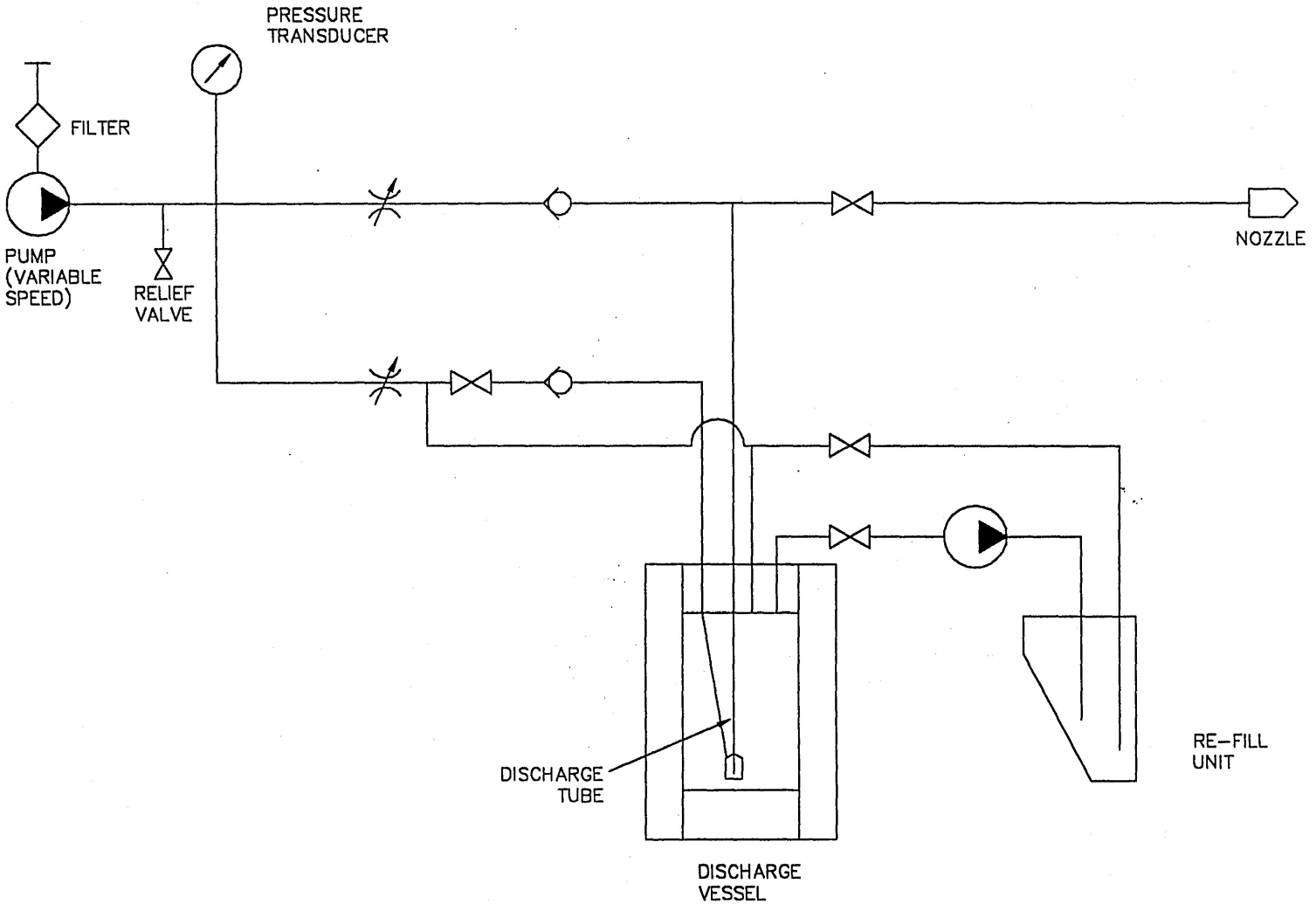

Figure 4.3 DIAJET cutting system

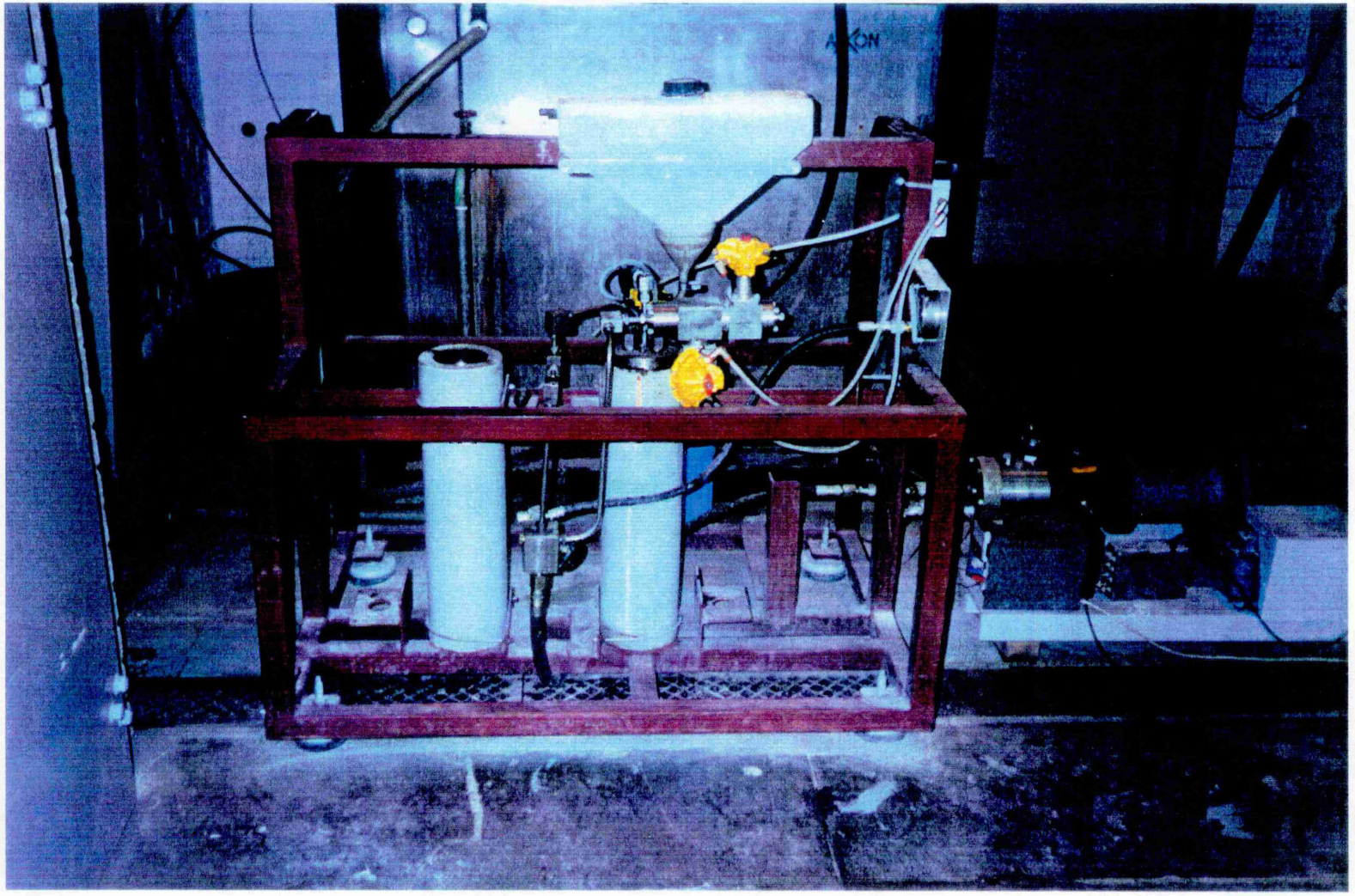

Figure 4.4 DIAJET circuit

In earlier DIAJET designs the restriction consisted of a check-valve, which had the dual function of isolating the pump from abrasive in case of a system failure. Although this was successful with the larger nozzle, higher flow systems, problems occurred with chattering of the check-valve once the flow was reduced for the lower pressure and smaller nozzle tests.

The design was changed so that two restrictions, in the form of short orifices, were placed in either line. The obvious advantage of this is a fixed ratio of flows and therefore a constant abrasive concentration despite varying conditions such as flow or pressure. In both designs, if a blockage occurs in the vessel, the pressure drop across the main flow increases due to the extra flow providing additional effort to unblock the system.

Pressure drops of around 1 MPa have been traditionally used in DIAJET systems and was used here. However, in some system/abrasive configurations, 10 MPa has been required to discharge the abrasive successfully.

Assuming the orifices are short, the total velocity head will be lost, i.e. the pressure drop across the orifices will be $\delta p = \frac{\rho u^2}{2}$. Thus for a percentage of flow, c, diverted through the vessel, the ratio of orifice diameters can be calculated as:

$$\frac{\rho u_1^2}{2} = \frac{\rho u_2^2}{2}$$

$$i.e. \frac{4\rho c Q}{\pi d_1^2} = \frac{4\rho(1-c)Q}{\pi d_2^2}$$

$$\frac{d_1}{d_2} = \sqrt{\frac{c}{1-c}}$$

For a pressure drop of 1 MPa across the orifice $d_1 = \sqrt{\frac{cQ}{11.1}}$

4.4.2 Abrasive discharge device

In traditional DIAJET designs, the flow to the vessel would enter at the top, and discharge from the bottom, via a patented discharge device. However, the finer abrasives demanded in this machine have been previously found to cause blockages when connected in such a way, and so some design changes are necessary.

The problem appeared to be the increased pressure drop across the bed of fine particles, hindering water flowing down through the bed. The highly concentrated flow would then block the discharge device. The solution to this problem of lack of flow through the 'bed' was to channel some clean water close to the discharge inlet at the bottom of the vessel. Such an idea had been used in the past when carrying out brief trials at 200 MPa, but because of the restricted diameter of the then available vessel and the limitation of one port in the vessel, this fluidising flow and the discharging mixture were channelled through sharp-cornered annuli, increasing the risk of failure.

For this system, trials were carried out in perspex to develop a device capable of meeting the above requirements with the added condition that as much as the bed as possible should be fluidised.

Trials were carried out using the standard discharge device within the vessel (as in traditional DIAJET designs), then using the annular device described above, and finally using a more straight-forward annular system. This device is actually part of the original DIAJET patent as one method of discharging grit from hoppers, but has not been used since the original investigations [16]. This design channelled the total top-up flow into the bottom of the vessel through a swirl device situated around the discharge tube.

For simplicity of build the discharge was channelled back up through the bed via high pressure tubing and the swirl flow piped down through the bed. This device seemed to work exceptionally well within the perspex vessel. An upward flow of water at the inner vessel wall could be seen, aiding downward movement of the abrasive.

For the remainder of the trials the prototype system reverted back to annular tubes extending from the top of the vessel. Here, the main flow passed down through the outer annulus and mixed with the discharging slurry, the total flow then exiting via the inner annulus. From trials carried out this system provided as consistent an abrasive flow as the swirl device, but could be easily removed for inspection or repair. In addition, the slurry concentration was everywhere kept to a minimum reducing blockage problems [103].

4.4.3 Piping requirements

Conventional DIAJET systems (34 - 69 MPa) had always been designed for relatively large nozzles (2 - 3 mm diameters) and therefore large slurry flows. Hydraulic hose was used to connect components, suitably rated for water hydraulics. As this rig was designed to test components for a high pressure DIAJET, at up to 200 MPa, the components selected were high pressure tubing and fittings. Standard 9/16 inch 'Autoclave' tubing and components were used as these were available, and no problems seemed to occur [104].

9/16th Autoclave pipes were chosen for the system, including the discharge tube within the vessel. This tube had a bore of 4.58 mm. Operation of the circuit at pressure was not consistent, with constant blockages occurring. These were solved by replacing the high pressure tubing used for the discharge tube with medium pressure pipe, thus increasing the internal bore to 7.9 mm. This seemed to solve the problem, and cutting trials began.

The rig was then rebuilt using 3/8 inch components and tubing (3.18 mm internal bore) after duning occurred in the pipe work. This is the slow deposition of material in the pipes where the velocity is less than the critical transport velocity [105]. Once again, the final prototype, designed for 69 MPa, used standard hydraulic pipework and hoses, though the inner bores were as stated above.

4.4.4 Abrasive containing vessels

The abrasive containing vessels used for low pressure (69 MPa) suspension jet systems are usually hydraulic accumulator shells. The advantage of this is their availability and price.

The above vessels, when new, have hydraulically smooth walls. This is essential to allow the abrasive to move down en-mass in the vessel easily and thus avoid bridging or rat-holing.

These phenomena did occur in an earlier vessel used for the trials. The walls were badly pitted and corroded. Here the problem was solved by further splitting the vessel flow between top-up (as above) and the swirl device mentioned in the previous section.

The higher pressure tests were carried out using pressure vessels based on intensifier pump and isostatic pressing technology. These vessels need dedicated designs, not least because standard oil hydraulics uses a safety factor of 4:1 while water hydraulics is generally only 1.5:1. Thus the specially designed vessel will be smaller and cheaper to manufacture. The vessels used were of a duplex design, the inner vessel being autofrettaged to increase its fatigue life. In addition, a separation intensification system was built into the base to allow rapid, independent pressurisation of each vessel.

4.4.5 Nozzle

The final part of the cutting system is the nozzle. It is here that the potential energy of the high pressure water is converted to the kinetic energy of a high velocity jet. It is here also that the inter-phase forces accelerate the abrasive particle to velocities approaching the water velocity. The design of the nozzle dictates the water velocity, from the discharge coefficient associated with that particular design.

The majority of the acceleration of the mixture takes place in the initial, convergent, section of the nozzle. However, a parallel section is necessary to accelerate the abrasive fully. This section also acts to stabilise the jet by reducing the turbulent boundary layer. For turbulent flows, it takes approximately 30 diameters to reach fully developed flow [88].

The nozzle length chosen will be a compromise between efficiency and nozzle life. Too short a nozzle may cause a rapidly diverging jet and has less material to erode thus decreasing life but is more efficient. For the flows under consideration, the power loss per

diameter length is approximately 1.5% based on the co-efficient of friction at the wall. Longer nozzles provide more time for the particles to accelerate up to full velocity and increase life, but also decrease the co-efficient of velocity for the nozzle and thus decrease the absolute cutting performance. The findings of this study will be applied to finding optimum nozzles for cutting efficiency as well as the optimum compromise between performance and life. This must also include the cost implications of producing longer bores, as the majority of the cost is capital cost and set-up time rather than machining time.

The nozzle also determines the properties of the emergent jet, and the theories of plain water jet nozzles can be used here to aid in the design. At higher pressures, the jet tends to diverge more rapidly, and thus the stand off distance, between the nozzle exit and the surface of the target material, will be a critical factor in these systems. In practice the distance can be reduced to the level of inaccuracy of the motion controlling actuator. However, with the risk of wear due to splash back when piercing or kerfing, a practical limitation of 2 - 5 nozzle diameters stand off is normal, depending on the actual nozzle design. The actual stand-off for these trials was measured at 2 mm for all trials. As with the cutting wear mode, section 3.3, the velocity decrease will be ignored during this stand-off distance. The nozzles used during this project are shown in figure 4.5, with figure 4.6 showing a test shape being cut by the abrasive water jet.

4.5 System calibration

The abrasive concentration was initially inferred by placing a turbine flowmeter in the swirl line. This was calibrated by catching the sand over a one minute interval. It was found that the rule of thumb of 1 kilo of abrasive per litre of water held true for the silica based abrasive used during these trials. Figure 4.7 shows the calibration curve for the initial research system.

Subsequent rebuilds of the system did not have the flowmeter as wear problems occurred during the initial trials. However, by using orifii to create the restrictions the abrasive flow could be set and controlled more consistently, as the calibrations show.

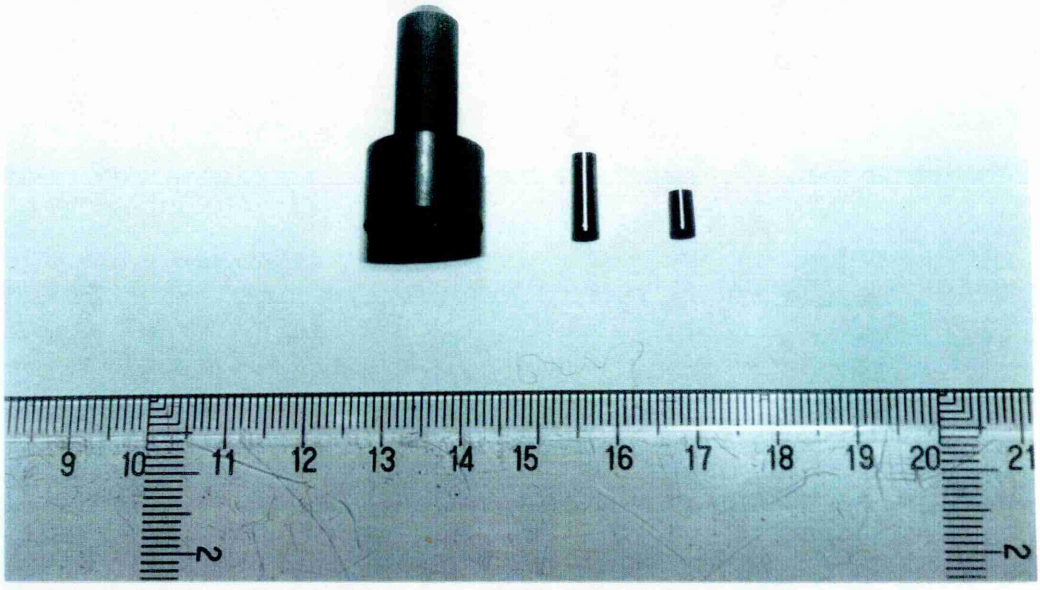

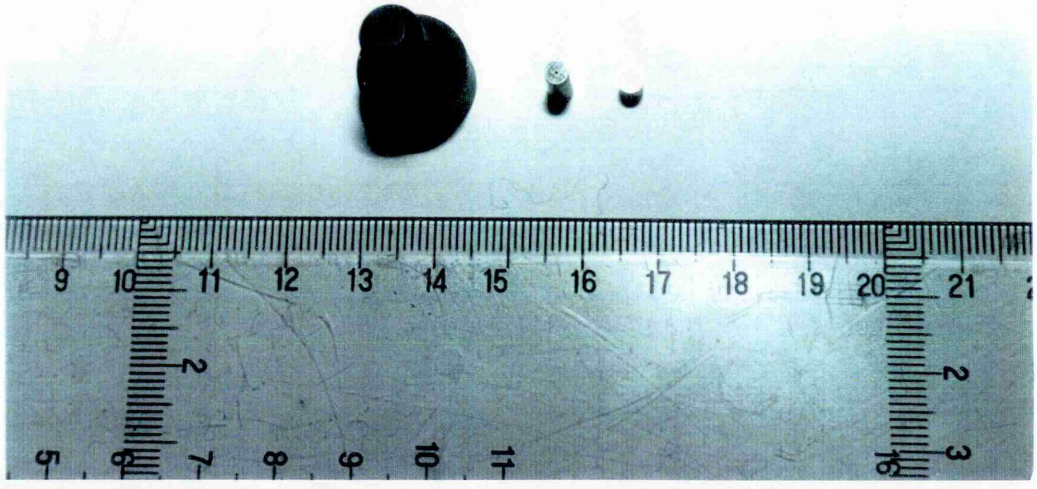

Figure 4.5 DIAJET nozzles

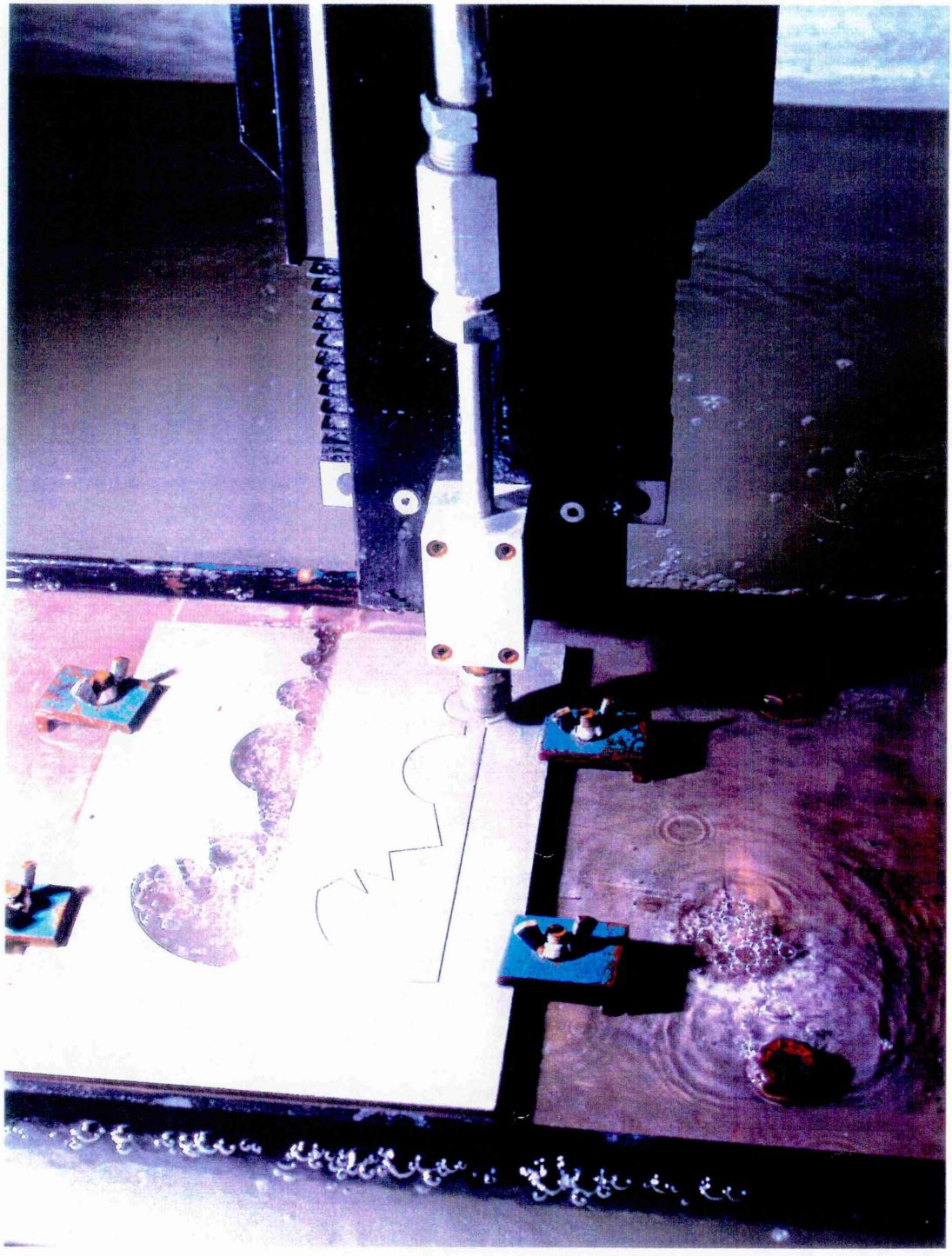

Figure 4.6 DIAJET abrasive water jet cutting

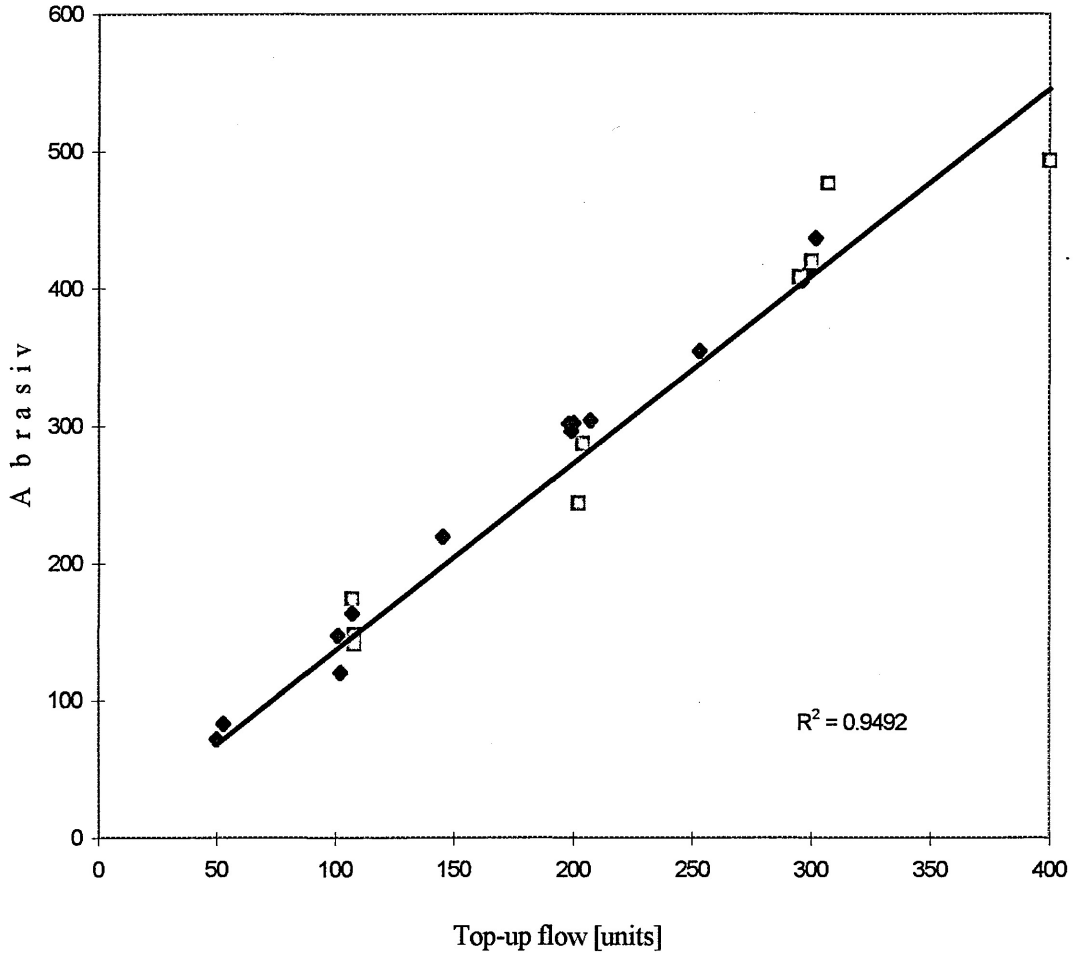

Figure 4.7 DIAJETabrasive discharge calibration

The machine was next used to carry out trials with even finer grit - sieved to 100 microns. The abrasive was a silica sand, and only about 25% of it passed through the sieve giving a skewed size distribution. This size of abrasive is just above what is classed a flour. The abrasive was briefly used with the 0.4 mm nozzle cutting 304L stainless steel. No appreciable performance drop was noted [106].

Trials with a 0.2 mm nozzle gave initial problems, thought to be flow related (the flow and thus pipe velocities were down by a factor of 4), but the problem appeared to be sieving problems with oversized grit blocking the nozzle. This 0.2 mm system was operated at pressures of up to 250 MPa, yielding some of the smallest-width cuts carried out to date with an abrasive water jet. The basis of these trials was in proving the technologies superior running costs to traditional methods of precision machining, such as diamond tipped saw blades [106]. The lower running cost of the DIAJET would allow repayment of the capital cost of the machine within 3-4 months!

Once the flow meter had been removed from the system, the concentration was checked by catching the abrasive being discharged from the machine. The values measured were consistent between flows and flow rates, although they did not agree exactly with the orifice sizing, suggesting a significant pressure drop somewhere in the system.

4.6 Laser Doppler Anemometry

Laser Doppler Anemometry is a process where small particles, assumed to be moving at the fluid velocity, pass through a probe volume to provide a source of scattered light with a frequency characteristic of the particle velocity. This non-intrusive technique was considered ideal given the small measuring volume (0.4 mm diameter jet), high velocities and the abrasive environment The stability and linearity of optical electro-magnetic waves yield measurements that are impervious to changing variables such as pressure fluctuations. The optics' configuration determine the actual velocity measured. The basic idea is the timing of light scattering from a particle over a known number of interference fringes within the measuring volume.

A doppler anemometry system will consist of several pieces of equipment, including the following: 1) laser, 2) transmitting optics, 3) receiving optics, 4) photo detector, 5) signal processor, 6) data acquisition and processing device (computer), and a frequency shifter for flow reversals. There are three types of scattered light collection: backscatter, forward scatter, or off-axis.

These experiments used forward scatter light collection. This method requires the collecting optics be aligned precisely on the optical axis. Figure 4.8 depicts the setup, where the receiving optics would be positioned off-axis to receive the scattered light, u. Figure 4.9 shows a photograph of the optics in position either side of the abrasive water jet.

A Hughes 15 mW Helium-Neon laser was used for the experiments, producing a beam of light 1.2 mm diameter with a wavelength of 632.9 E-9 m. At all cross-sections the intensity of this beam has a Gaussian distribution. At a point known as the beam waist, the cross-section has its smallest value. The polarised laser beam enters a beam splitter, which separates the beam into two parallel beams each 1/2 the original beam's intensity, by the use of a partial mirror, and fully reflective surfaces. The beam splitter used here creates a 59 mm beam spacing. After the beam splitter the two parallel beams pass through the focusing lens, which redirects the beams, and causes them to converge at the focal point of the lens. By varying the beam waist adjuster this point, known as the probe volume, contains the beams intersecting at their waist.

Within this volume, an interference pattern is set up by the two beams. This is generally Gaussian in distribution. By positioning this probe volume within the abrasive water jet, particles passing through this volume cause further modulation of the signal, according to their velocity. The frequency measured, known as the doppler frequency, is the frequency of the interference of the two doppler shifted scattered light waves, and this interference frequency is equal to the difference in the frequencies of the two doppler shifted light waves.

The relationship between the doppler interference frequency and particle velocity is given by:

$$f_D = \frac{2}{\lambda}\sin(\frac{\theta}{2})|V_x|$$

where f_D is the frequency of interference of the doppler signals, $|V_x|$ is the absolute value of the particle velocity within the probe volume, θ is the included angle of intersection between the beams (lens include angle), and λ is the wavelength of the laser light (632.8 e-9 m). The fringe spacing d_f can be calculated from $d_f = \frac{\lambda}{2\sin\frac{\theta}{2}}$.

The scattered light passes through the collecting optics and on to a photomultiplier where the light signal becomes an electrical signal. Some signal processing equipment conditions the signals before transmission to the computer. A simple calibration was carried out by measuring the velocity of the water jet with mains pressure alone. The contaminants in the mains water act as seeds for the velocity measurement.

The lda system was then used to measure the velocity of the water jet with no abrasive and with abrasive. The pressure was held at 10 MPa and then increased in 10 MPa steps to provide enough data points for validation of the method and the model.

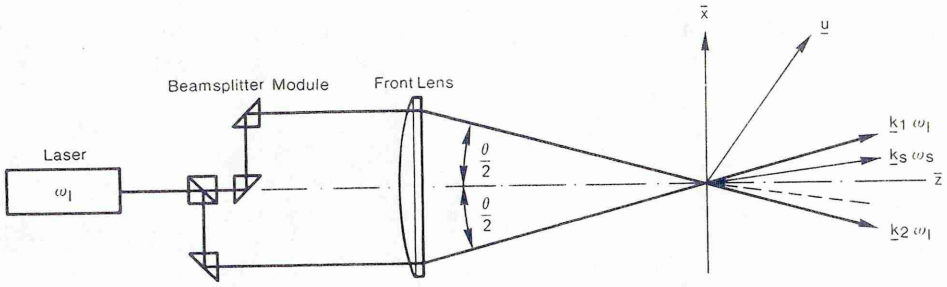

Figure 4.8 Laser Doppler anemometry - vector diagram

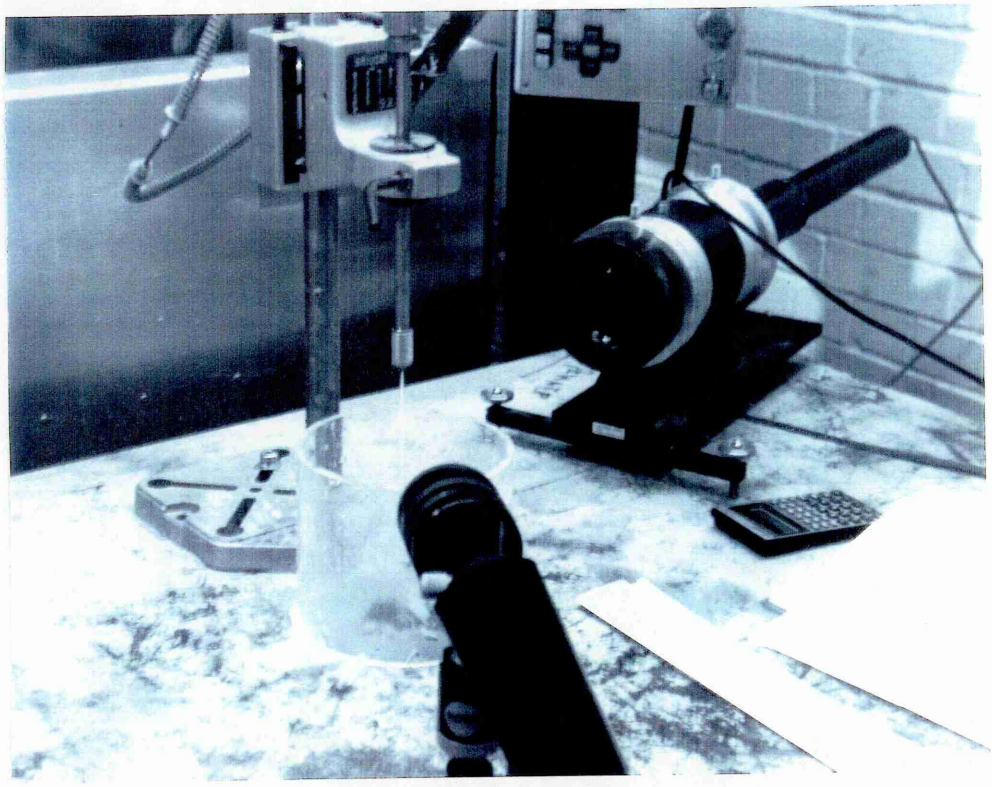

Figure 4.9 LDA experimental setup

CHAPTER 5 - RESULTS AND DISCUSSION

5.1 Preliminary experimental results

An initial search of cutting trials previously carried out at BHR Group was undertaken to identify the experimental parameters important in the cutting process, and compare this with the theoretical predictions. This work was found to be inconsistent, in that the results quoted varied by up to 300% for seemingly identical parameters. In order to eliminate these uncertainties, only test results carried out during this project are reported here for validation purposes.

A preliminary series of trials was carried out on aluminium, brass and titanium. Four thicknesses of each material (two for titanium) were cut at increasing speeds until the limit cutting speed for that thickness was reached.

The operating parameters were:

Pressure 69 MPa pressure, nozzle 0.4 mm diameter, 60° inlet angle, 4 mm long

Abrasive Olivine AFS120 sieved to 250 microns with a flow rate of 80 gm/min

The results of these trials are given in the table below:

Pressure: 69 MPa	Measured abrasive flow rate: 80 gm/min			
Aluminium				
Material thickness	5mm	10mm	20mm	30mm
Speed [mm/min]	350	155	50	28
Brass				
Material thickness	5.6mm	9.5mm	19.05mm	31.8mm
Speed [mm/min]	270	114	42	20
Titanium				
Material thickness	2mm	5mm		
Speed [mm/min]	400	140		

The cutting results are shown in the figure 5.1, with the predictions from the model of cutting depth. For the model, 1 MPa was assumed to be dropped accross the system orifii, yielding a 68 MPa cutting pressure, i.e. pressure drop accross the nozzle.

Figure 5.1 69 MPa, 0.4 mm nozzle 80 gm/min olivine 80

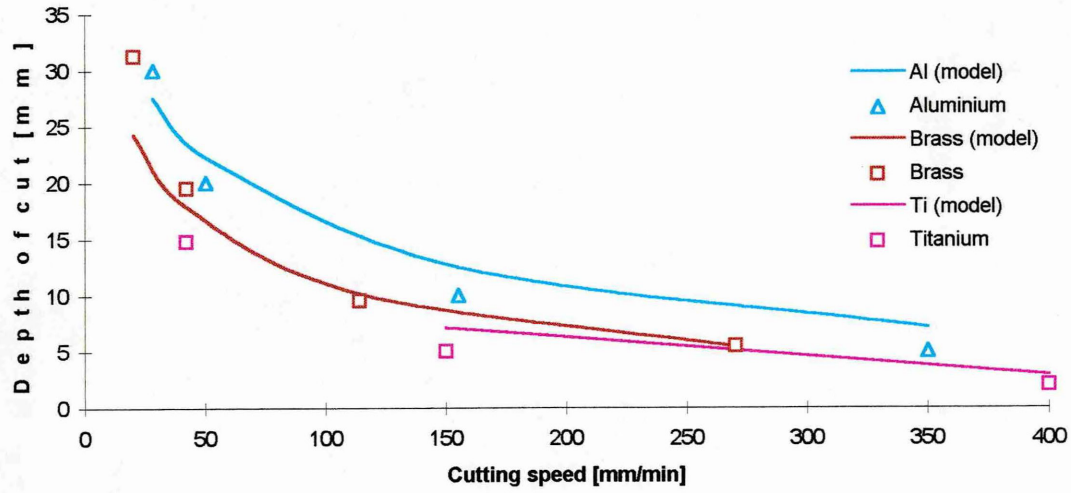

Further trials carried out on mild steel with both 0.4 and 0.2 mm nozzles are in good agreement with the model [106]. As the abrasive used for part of these trials was sieved to 100 μm with similar performance to the larger sizes, this suggests that there is no noticeable degradation in cutting performance with decreasing particle size.

5.2 Cutting trials

5.2.1 Brass CZ108 half-hard

Nozzle diameter of 0.53 mm, 60° inlet angle, 8 mm parallel length.

Abrasive Olivine AFS 80, sieved to 250 μm.

Original thickness of material 31.8 mm (1¼").

A main orifice of 1.5 mm, and a jet pump orifice of 0.5 mm yielded a theoretical abrasive flow of 10% or 450 gm/min at 68 MPa, measured 300 gm/min.

Brass	Figure 5.2			Olivine AFS 80, sieved < 250 µm		
Operating pressure [MPa]				69		
Measure abrasive flow rate [gm/min]				540		
	Cut speed [mm/min]					
Pressure	30	60	90	120	150	180
69 MPa	thru'	thru'	27	21.5	20	17.5
69 MPa	thru'	thru'	26	22	18.5	-
Operating pressure [MPa]				69	50	40
Measure abrasive concentration [gm/min]				300	250	230
	Cut speed [mm/min]					
Pressure	100	150	210	270	360	450
69 MPa	17.5	15	12	9	7	5
69 MPa	17.5	15	12	9	6.5	5.25
69 MPa	17.5	14.5	11	8	7	5
50 MPa	15	10	8	6	4.5	3.25
40 MPa	11.5	9	7	5	3.5	2.5

Repeat trials, abrasive flow rate measured 160 gm/min at 69 MPa.

Brass	Figure 5.3			Olivine AFS 80 sieved < 250 µm		
Operating pressure [MPa]				69	50	40
Measured abrasive flow rate [gm/min]				160	136	122
	Cut speed [mm/min]					
Pressure	100	150	210	270	360	450
69 MPa	15	12	10	8	6	4.5
50 MPa	15	11	9	6	5	4
40 MPa	9	7	6	5	4.5	3.5

Replaced main orifice with 1.2 mm to give higher concentration

Brass	Figure 5.4			Olivine AFS 80 sieved < 250 µm		
Operating pressure [MPa]				69	50	
Measured abrasive flow rate [gm/min]				350	275	
	Cut speed [mm/min]					
Pressure	100	150	210	270	360	450
69 MPa	20	15	10.5	8.5	6	4
50 MPa	16	12.5	8	5	4	3

Trials using silica 90 sieved to less than 100 microns

Brass	Figure 5.5			Silica 90 sieved < 100 µm		
Operating pressure [MPa]				69	50	
Measured abrasive flow rate [gm/min]				300	250	
	Cut speed [mm/min]					
Pressure	100	150	210	270	360	450
69 MPa	14.5	11	8	6.5	5	3
50 MPa	10	8	5	4	1.5	

Trials using 1.5 mm orifice and garnet as abrasive

Brass	Figure 5.6			GMA Garnet #80 sieved 250 µm		
Operating pressure [MPa]				69	50	40
Measured abrasive flow rate [gm/min]				168	143	128
	Cut speed [mm/min]					
Pressure	100	150	210	270	360	450
69 MPa	14	9.5	7	4		
50 MPa	8	6	5	3	2.5	2
40 MPa	7	5	3	2.5	2	1.5

Brass		Figure 5.7		GMA Garnet #80 sieved < 250 µm		
Operating pressure [MPa]				69	50	
Measured abrasive flow rate [gm/min]				385	325	
			Cut speed [mm/min]			
Pressure	100	150	210	270	360	450
69 MPa	25	20	15.5	12	10	7.5
50 MPa	19	16	11.5	9	7	5

5.2.2 Aluminium

Aluminium		Figure 5.8		Olivine AFS 80 sieved < 250 µm		
Operating pressure [MPa]				69	50	40
Measured abrasive flow rate [gm/min]				300	250	230
			Cut speed [mm/min]			
Pressure	40	70	150	250	350	450
69 MPa	30.5	22	18.5	17.5	14	11
69 MPa	30	23	19	17	14	10.5
69 MPa	30	23	19	18	15	11
50 MPa	20	18	14.5	10	9.5	8
40 MPa	18	16.5	11	10	8	6

Trials using 1.5 mm orifice and garnet as abrasive

Aluminium		Figure 5.9		Olivine AFS 80sieved < 250 µm		
Operating pressure [MPa]				69	50	
Measured abrasive flow rate [gm/min]				385	325	
			Cutting speed [mm/min]			
Pressure	100	150	210	270	360	450
69 MPa	30	26	22.5	18	13.5	10
50 MPa	24	18	14.5	12	10	

Aluminium		Figure 5.10		Silica 90 sieved < 100 μm		
Operating pressure [MPa]				69 MPa	50 MPa	
Measured abrasive flow rate [gm/min]				300	250	
	Cutting speed [mm/min]					
Pressure	100	150	210	270	360	450
69 MPa	22.5	18	15.5	11.5	9.5	8
69 MPa	26.5	19	15.5	11.5	9.5	8

5.2.3 Stainless steel 304L

304L		Figure 5.11		Olivine AFS 80 sieved < 250μm		
Operating pressure [MPa]				69	50	40
Measured arasive flow rate [gm/mig]				300	250	230
	Cut speed [mm/min]					
Pressure	40	70	150	250	350	450
69 MPa	15	11.5	8	5.5	4.5	2
69 MPa	15	11.5	8.5	6	4.5	2
50 MPa	9	7	4.5	3	2.5	1.5
40 MPa	8	6	4	2.5	-	-

5.2.4 Mild steel

Mild steel		Figure 5.12		Olivine AFS 80 sieved < 250 μm		
Operating pressure [MPa]				69	50	40
Measured abrasive flow rate [gm/min]				160	136	122
	Cutting speed [mm/min]					
Pressure	100	150	210	270	360	450
69 MPa	11	9	7.5	6	4.5	3
69 MPa	11	9	7.5	6	4.5	3
50 MPa	8.5	6	5	4	3.5	2
40 MPa	6	5	3.5	2	1.5	1

5.2.5 Marble

Marble		Figure 5.13		Olivine AFS 80 sieved < 250 μm		
Operating pressure [MPa]				69	50	40
Measured abrasive flow rate [gm/min]				300	250	230
	Cutting speed [mm/min]					
Pressure	800	1000	1200	1400	1600	1800
69 MPa	20	15	13	10.5	9	8
69 MPa	20	15	13	10.5	9	8
50 MPa	12	10.5	10	9	8	7
40 MPa	11	10	9.5	8.5	7.5	5.5

5.2.6 Correlation of the abrasive water jet cutting model

The following figures, 5.2 to 5.13 show the cutting results, above, plotted against the predictions of the mathematical model. All predictions show the correct trend for decreasing cut depth with increasing cutting speed, and the correct relative cut depth versus pressure.

However, over half of the sets of trials carried out do not fit the mathematical model for the measured abrasive concentration. For instance, figure 5.2 shows the results of two separate sets of cutting results at 68 MPa. The first set (red and yellow traces) fit the model for 2.3% abrasive by volume perfectly. When the trials were repeated at a later date, shown by the purple trace, the cutting performance was reduced for an identically measured abrasive discharge rate.

Other trials, e.g. figure 5.3, yield a lower value for the measured abrasive discharge rate. The model, at this lower abrasive concentration, provides an excellent fit to the experiments. Still other sets of trials yielding the expected 2.3% by volume abrasive discharge yielded a high degree of correlation, figure 5.12.

No explanation from the experimental procedure readily explains the inconsistencies. The sets of trials were carried out with a full pressure vessel each time, and the abrasive discharge measured randomly throughout the trial.

The results suggest that the system discharge rate is not constant, but varies between two, steady, values. All the poorly fitting results yield excellent correlation when the abrasive flowrate is assumed to be 60% of that measured. A similar discrepancy has been noted by others using the cutting system since [107]. At present, no other system is available to carry out further checks on the suitability of the mathematical model.

An abrasive concentration meter, based on ultrasonic attenuation through the slurry, is being developed at BHR Group [83]. This in-line device will allow constant monitoring, or actual measurement, of the abrasive discharge during the cutting process.

Figure 5.2 0.53 mm nozzle, 2.3% by vol olivine 80 on brass

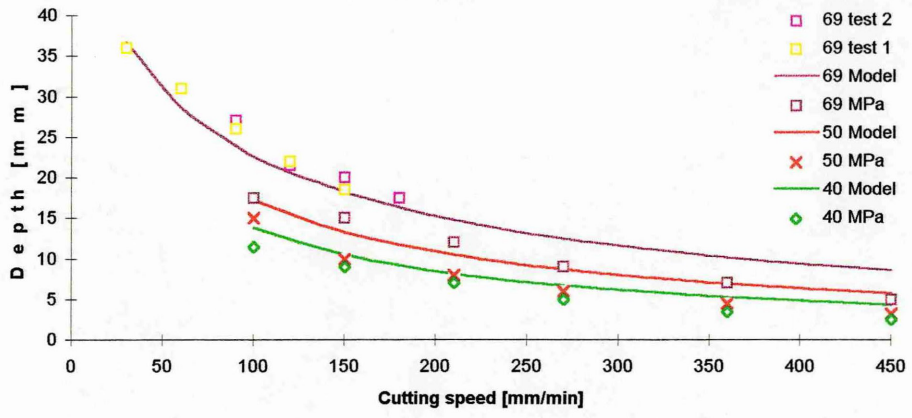

Figure 5.3 0.53 mm nozzle 1.2% by vol olivine 80 on brass

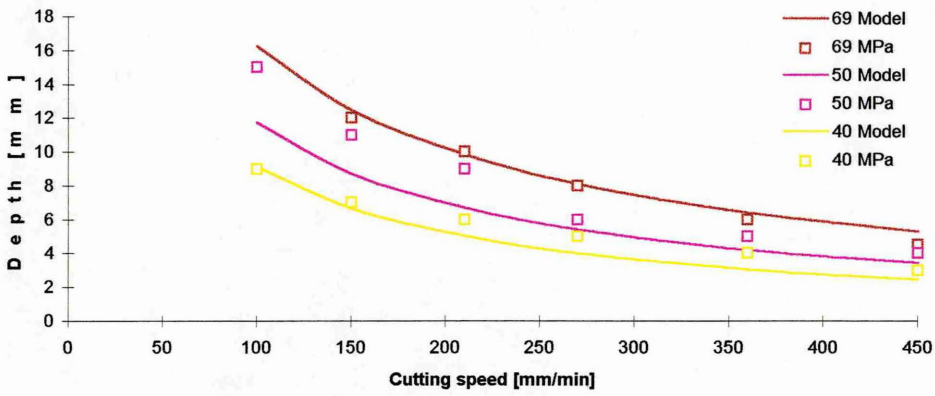

Figure 5.4 0.53 mm nozzle 3.4% by vol olivine 80 on brass

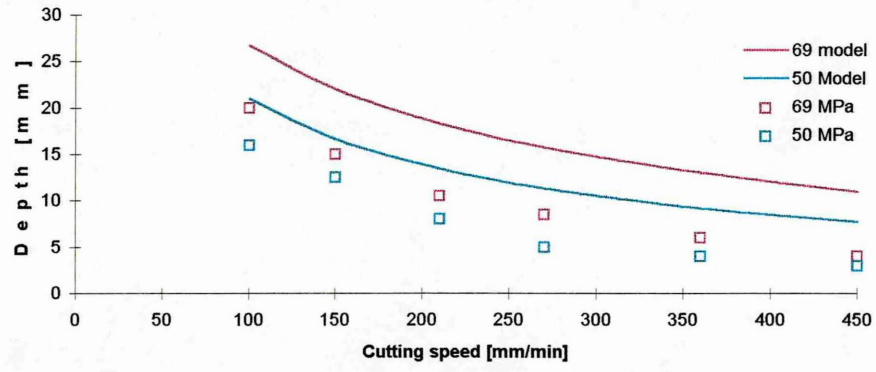

Figure 5.5 0.53 mm nozzle 2.3% by vol 100 micron silica 90 on brass

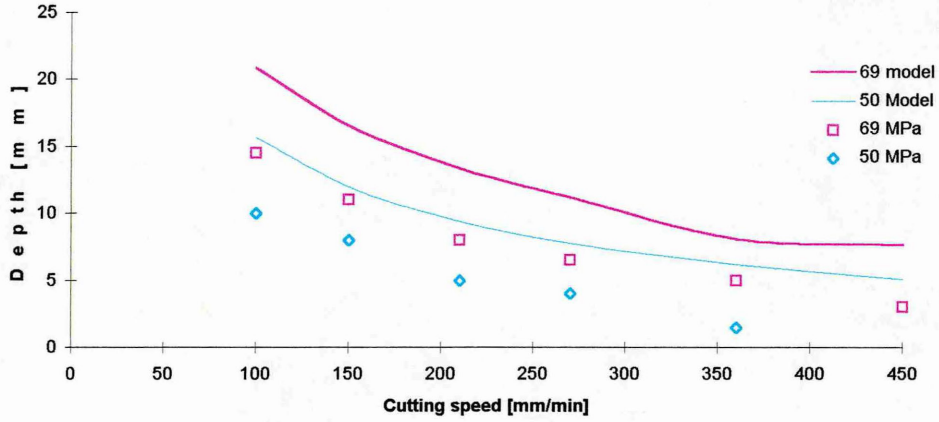

Figure 5.6 0.53 mm nozzle 1% by vol garnet on brass

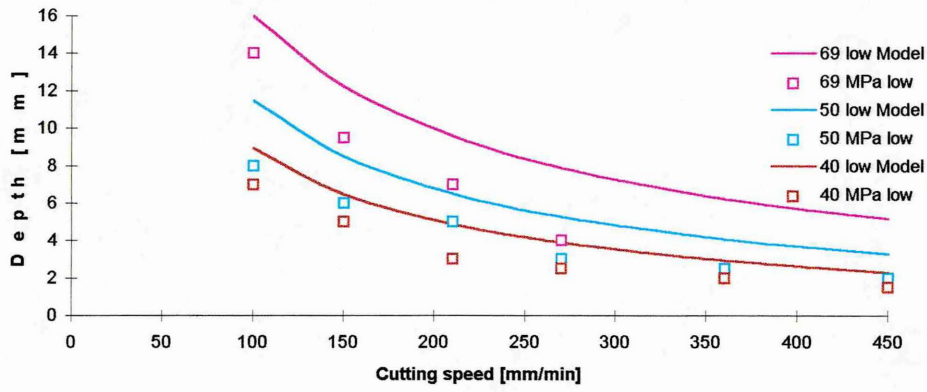

Figure 5.7 0.53 mm nozzle 2.3% by vol garnet on brass

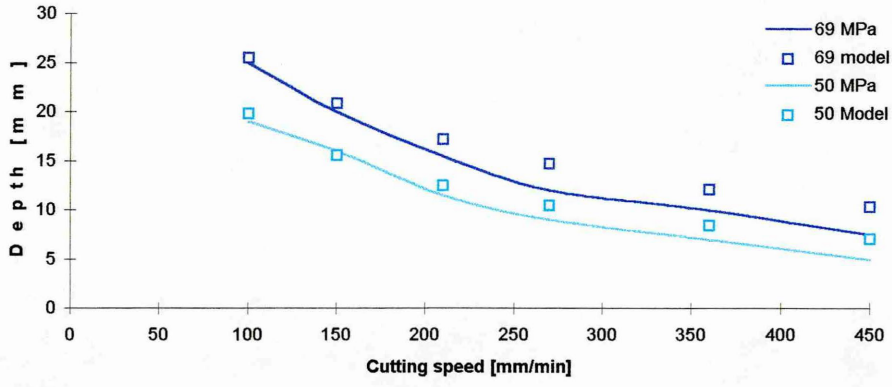

Figure 5.8 0.53 mm nozzle, 2.3% by vol olivine 80 on aluminium

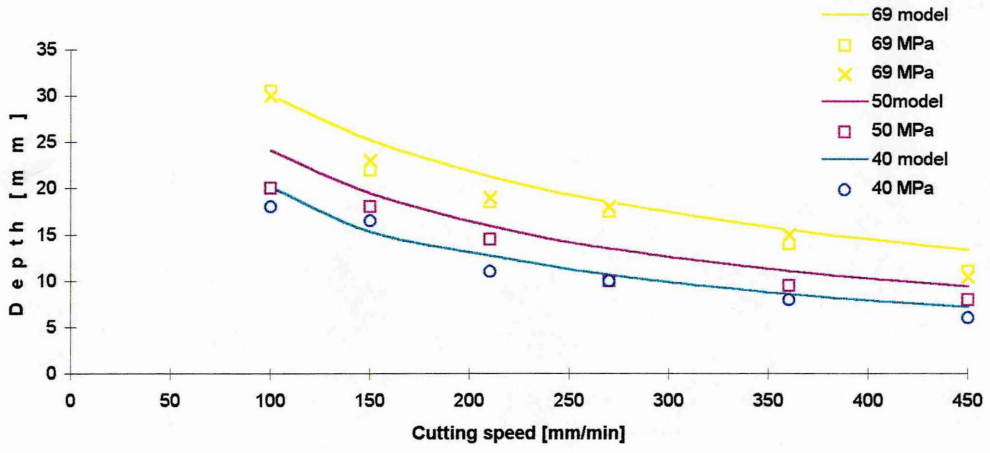

Figure 5.9 0.53 mm nozzle 2.3% by vol garnet on aluminium

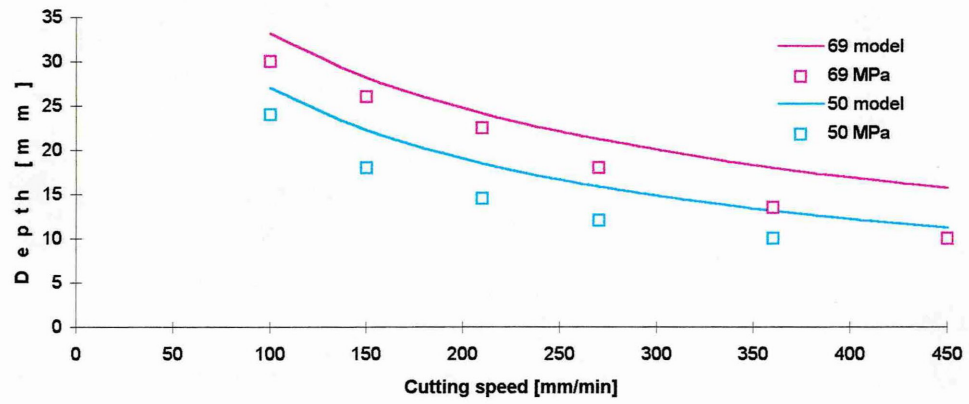

Figure 5.10 0.53 mm nozzle 2.3% by vol 100 micron silica 90 on aluminium

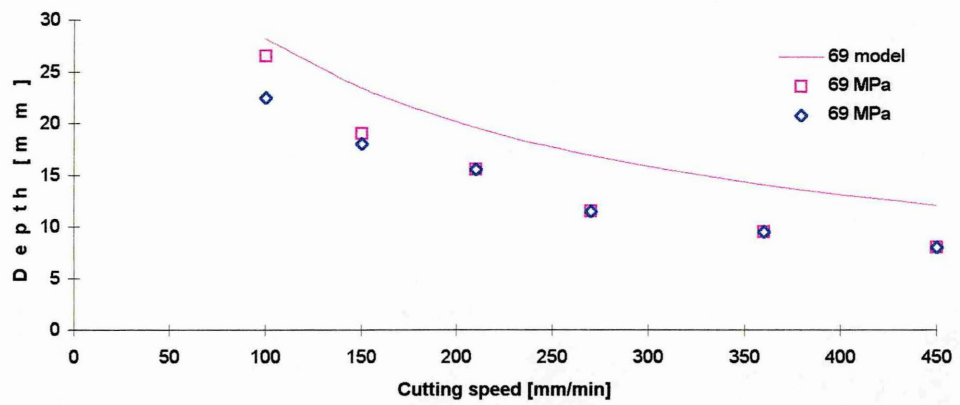

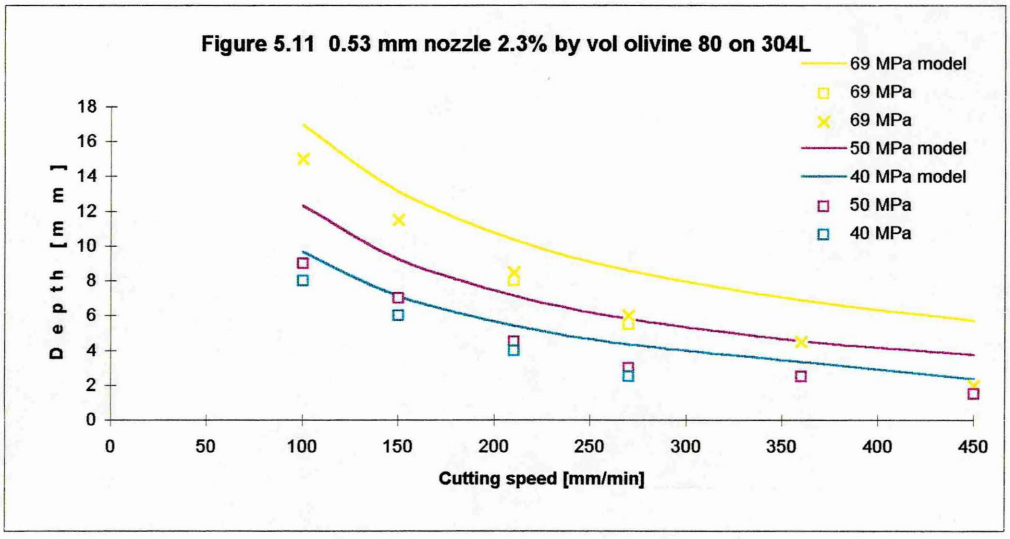

Figure 5.11 0.53 mm nozzle 2.3% by vol olivine 80 on 304L

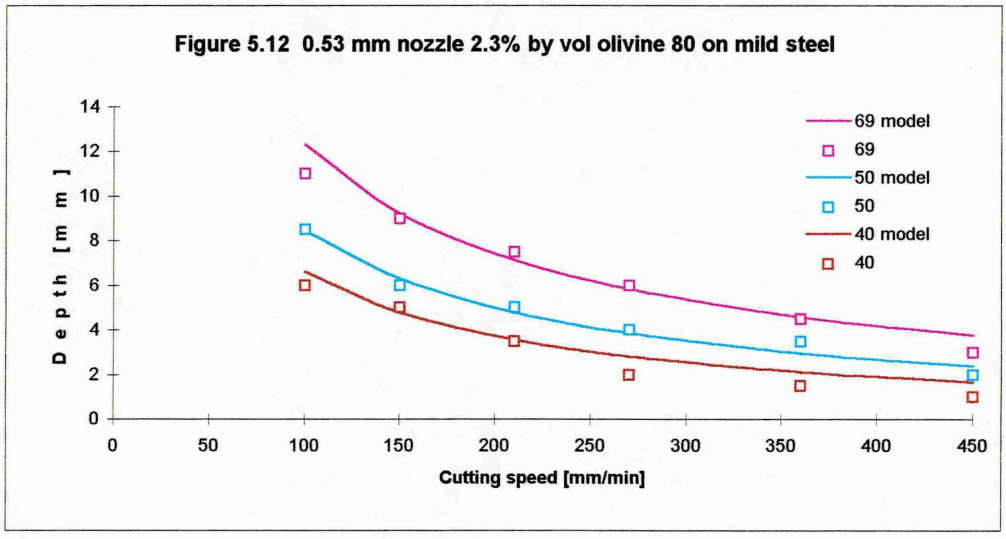

Figure 5.12 0.53 mm nozzle 2.3% by vol olivine 80 on mild steel

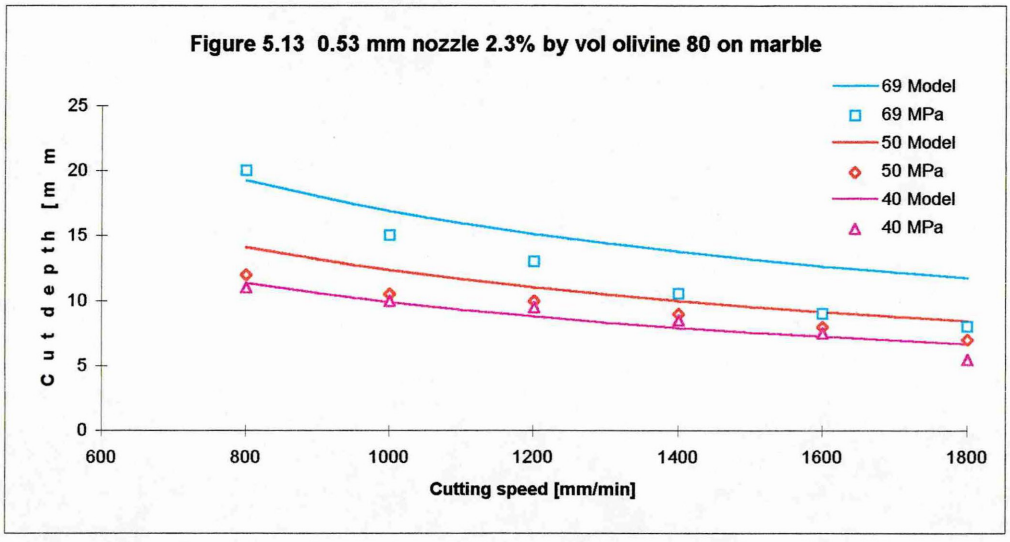

Figure 5.13 0.53 mm nozzle 2.3% by vol olivine 80 on marble

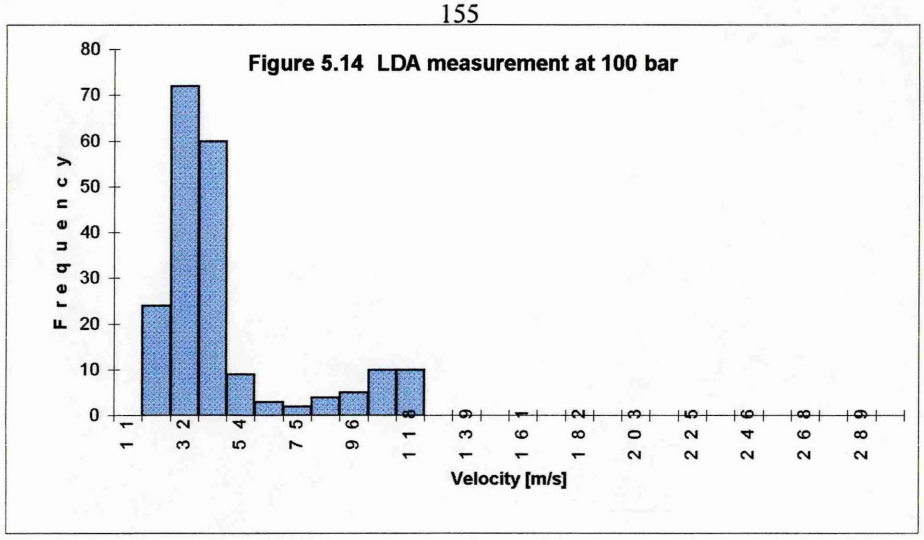
Figure 5.14 LDA measurement at 100 bar
Frequency
Velocity [m/s]
0
10
20
30
40
50
60
70
80
11
32
54
75
96
118
139
161
182
203
225
246
268
289

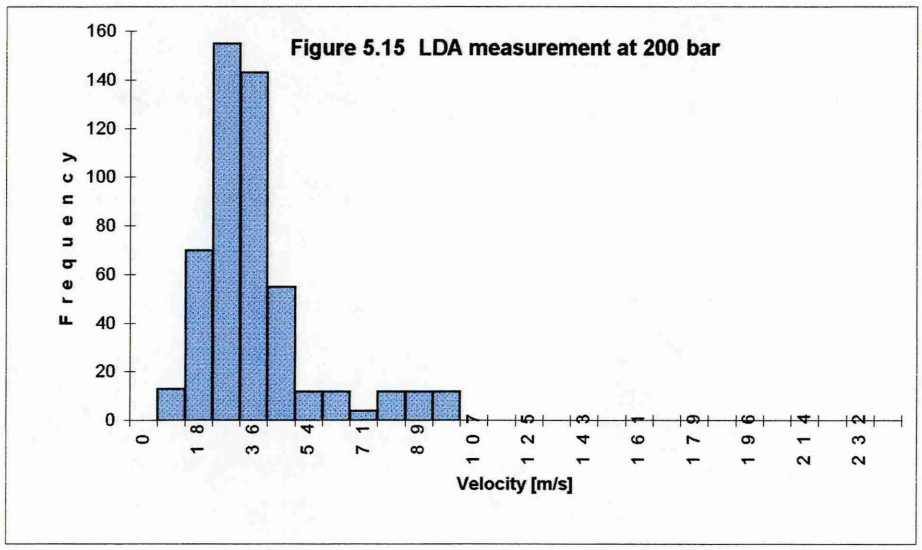
Figure 5.15 LDA measurement at 200 bar
Frequency
Velocity [m/s]
0
20
40
60
80
100
120
140
160
0
18
36
54
71
89
107
125
143
161
179
196
214
232

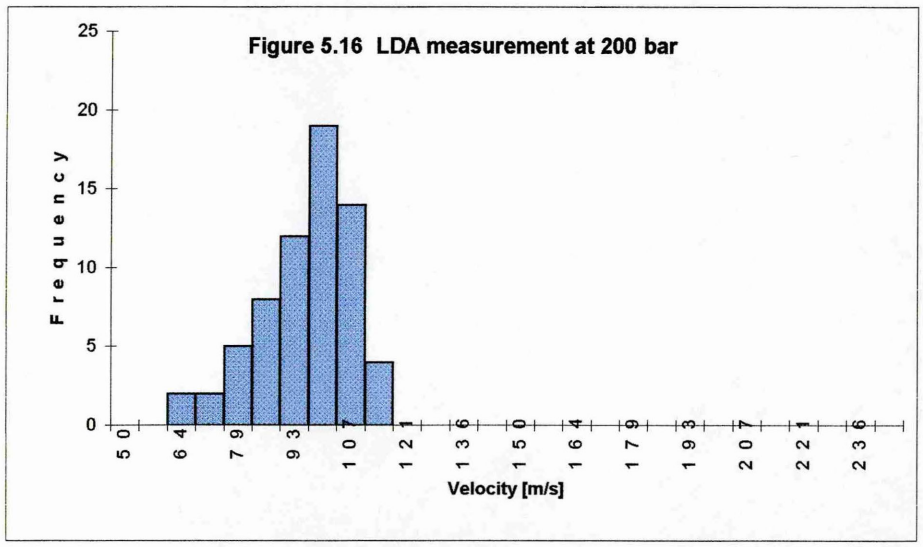
Figure 5.16 LDA measurement at 200 bar
Frequency
Velocity [m/s]
0
5
10
15
20
25
50
64
79
93
107
121
136
150
164
179
193
207
221
236

5.3 Particle exit velocity

Attempts to measure the particle exit velocity, by laser Doppler anemometry have proved unsuccessful. Figures 5.14 to 5.15 show the results of the measurements taken. It can be seen that, despite varying the pressure and hence the exit velocity, an average value of velocity just under 36 m/s was obtained. An almost identical value was measured for 30 and 40 MPa also. When measurements were taken excluding measurements below 50 m/s, the results were still erroneous, not varying much from 100 m/s but with no clear mean (figure 5.17). One possibility for the erroneous measurements is the possibility of interference from standing waves on the surface of the jet. A similar anomaly was reported during velocity measurement of an entrainment jet [108]. Although the values of velocity obtained for a water jet were correct, the same velocity was measured for all pressures once abrasive was introduced into the jet.

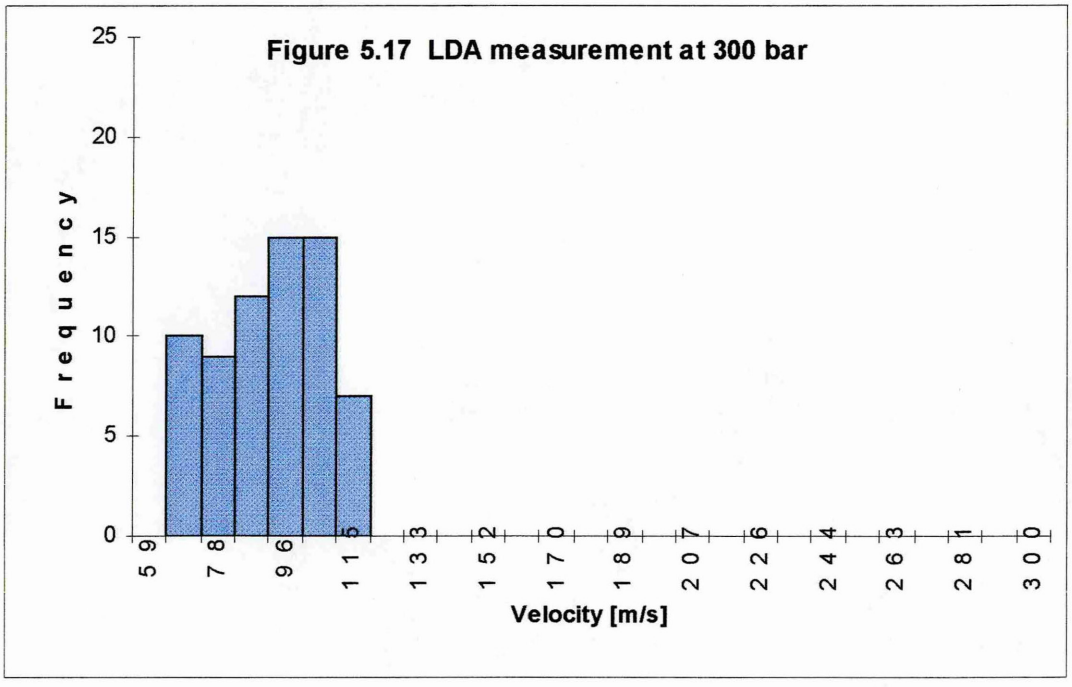

However, it has been possible to measure the average flow rate of the water and abrasive during tests to calibrate the flowmeter and check the abrasive discharge rate (section 3.4.5). For the 0.53 mm nozzle used here, the theoretical water velocity for 69 MPa is 4.2 l/min, and with 1 kg/min of olivine the water flow rate is reduced to 3.6 l/min.

Allowing for the volume of the water, this corresponds to a reduction of around 5%. This is similar to that predicted from the velocity of the mixture. These measurements are very crude, and it is quite difficult to guarantee that all the abrasive and water has been caught due to the danger of the high velocity jet.

What the model has shown, however, is that the majority of the particle acceleration occurs within the convergent section of the nozzle, the converse of what has been previously reported [8]. For the majority of suspension jet nozzles, it is sufficient to calculate the exit velocity based on the theoretical velocity of the mixture, using Bernoulli's equation. Figure 5.18 shows the results of the calculation of particle velocity within the nozzle. It can be seen that the maximum velocity (the theoretical slurry velocity) is achieved in all cases by 2 mm parallel section, or about 5 diameters length.

The implications of these findings is that, for more efficient systems, the parallel sections of nozzles can be made shorter, not longer, than the 10 diameters length currently chosen. However, this may not produce an economical design in all cases, as nozzle life will be reduced. In addition, as per the analysis of pure water jets (section 2.7) the short nozzle may diverge rapidly on exit.

The remaining system effect to be considered is the amount of damage caused by the accelerating process. Entrainment systems have been shown to cause substantial damage, with particle size reductions of nearly 80%. Suspension jets, on the other hand, cause much less damage at around 20% reduction [85]. The significance of this depends on the particles now being too small to erode effectively.

The experiments to validate the complete cutting model can then be simplified, with a high degree of confidence, into the model of the mechanisms of material removal using the slurry velocity discussed above.

Figure 5.18 Particle velocity through nozzle

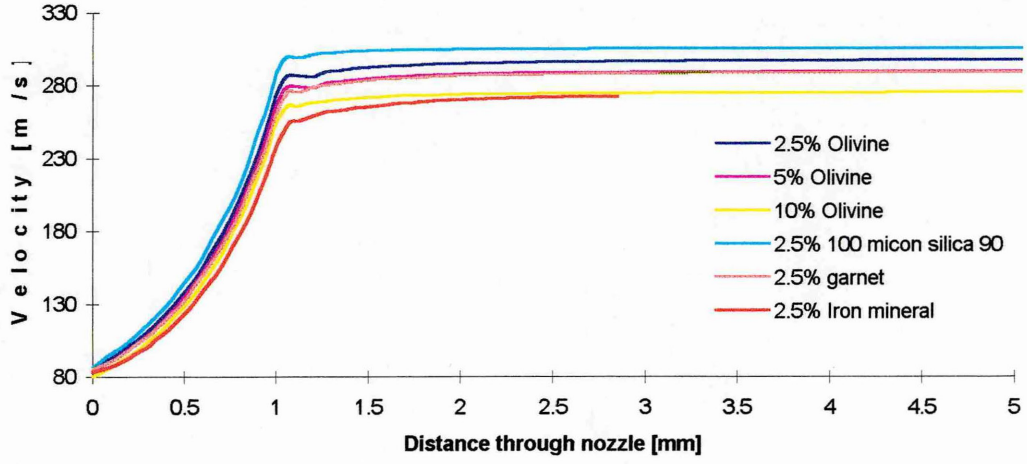

5.4 Discussion

From the results of the literature search, backed up by preliminary cutting trials, the primary mechanism of erosive wear occuring in AWJ cutting was deemed to be deformation wear. From the resulting model this is definitely seen to be the case, figure 5.19. Here, the cutting wear depth is visually much smaller. It can clearly be seen that the shape of the curve is dictated by the deformation wear, with the depth if cut due to cutting wear being almost constant.

In practice, the depth of cut should be greater than predicted at lower cutting speeds, as the assumption used to calculated h_c, the cutting wear depth, is inaccurate for thicknesses significantly larger than the nozzle diameter. This is slightly compensated for by not considering the deceleration during this mode.

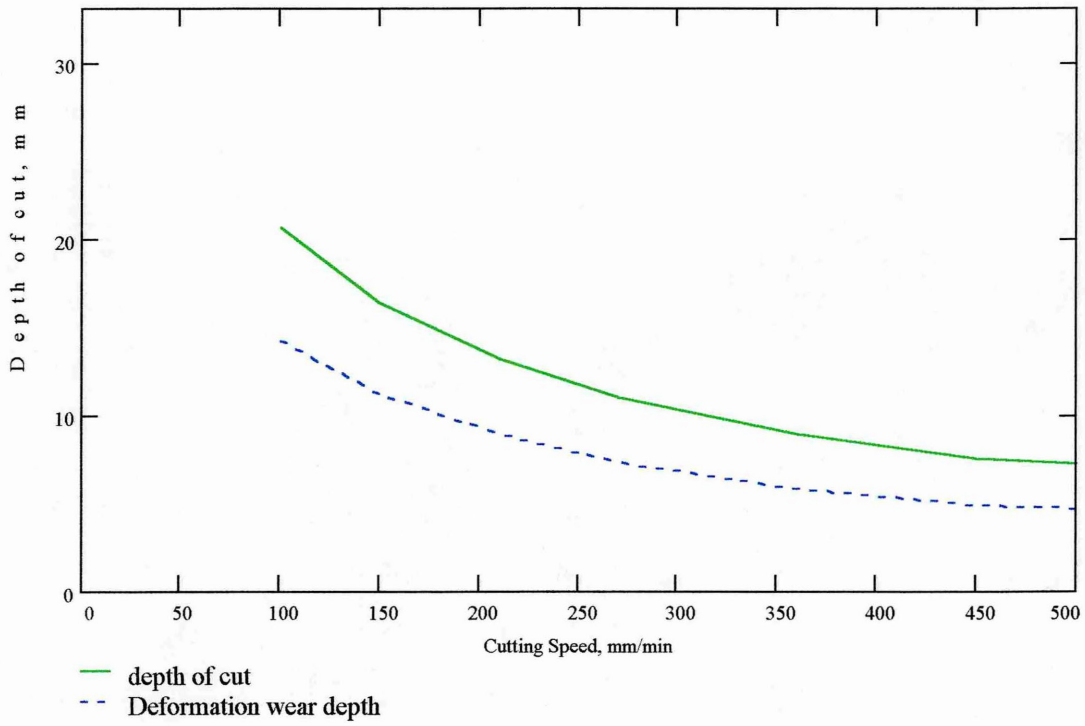

Figure 5.19 Cut depth for brass, 0.53 mm, 2.3% by vol olivine 80

Many models encountered over the period of this project assume the opposite. In fact some models consider cutting wear alone to be responsible for ductile material erosion. Abudaka reasons that the reduced modulus is large relative to the material strength so that one can validly ignore the deformation mode [58]. Latif also considers cutting wear alone, attempting to predict the required cutting speed to achieve a good level of surface finish and not the maximum cutting depth [85].

The reasoning stems from the assumption that only deformation wear mode produces striations. As quite a large depth of the cut surface is striation free, cutting wear must be significant. However, as striations are evident in the cutting of brittle materials, with almost universal agreement of crack growth as the erosion mechanism, this assumption cannot be valid, and even for predicting speeds for a "good" level of surface finish they will be conservative. For straight line cuts, 50% of the maximum parting speed is adequate to give a good cut quality (surface finish of around Ra = 8 μm).

It is impossible to quantitatively determine the contribution of each mode as the change from one mode to the other is not observed on the cut surface because at intermediate angles both modes are in operation. In additon, once the cut surface is generated, over 10 million particles per second from the abrasive jet polish the surface. This jet also causes continuing damage to wear debris, making any analysis from them difficult also.

However, at the faster speeds, yielding rougher surfaces, evidnece of brittle fracture can be seen. SEM analysis of the cut surface of brass is shown in figure 5.20 below. Intergranular cracking can be seen, justifying the assumption of deformation wear mode.

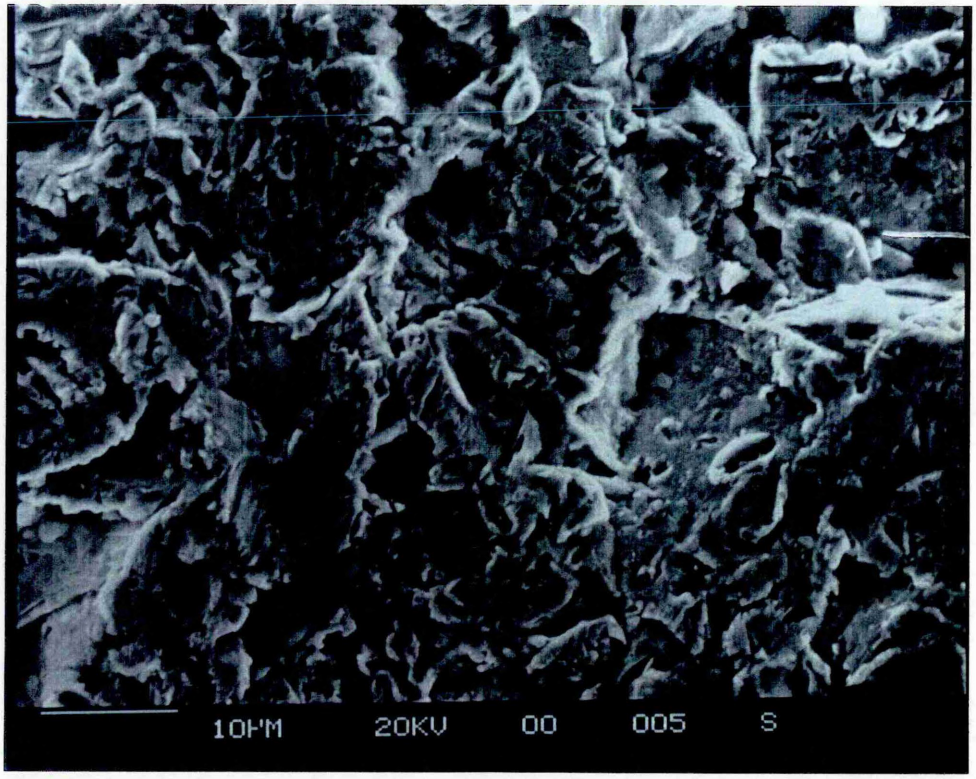

Figure 5.20 SEM analysis of AWJ cut surface

Deformation wear is an unsteady process, unlike cutting wear. Thus a time dependency enters the equation, and it is this that causes the regular "flicking" of the abrasive jet which may be witnessed as it leaves the material. This "flicking" is seen even at low speeds in comparison to the maximum cutting speed for that thickness of material, and this qualitative fact, with the visualisation trials of Hashish [51], validates the assumption of a small cutting wear zone. This then leads to being able to ignore the deceleration of the jet through this cutting mode.

In addition, the spreading and deceleration of the jet is ignored in the stand-off distance, i.e. the distance between the nozzle exit and the material surface. For the case of precision machining, this distance will be limited to about two jet diameters and thus it is a valid assumption.

Other applications, such as off-shore cutting with a less precise actuator, and possibly requiring multipass cutting, resulting in much greater stand-off distances might have to consider these effects. This would be achieved by using the model of particle acceleration derived for the nozzle, but with appropriate boundary conditions to account for the flow regime outside the nozzle. In such situations, however, optimisation of the cutting speed is not required as the actual cutting operation represents only a small fraction of the job.

Figures 5.5 and 5.10 show the performance of sub-100 μm particles of silica on brass and aluminium respectively. Considering the silica sand has a specific gravity of 2.8 as opposed to olivine's 3.3, 20% more olivine (by weight) was used resulting in approximately 20% more cut depth. Therefore, reduced particle sizes are not ineffective at cutting. Rather, considering the smaller nozzle sizes that can be used, they are more efficient in terms of cut surface generated per unit of abrasive as the kerf width is less. In addition, small particles are accelerated quicker, to higher velocities (figure 5.18). Additional trials, with 0.4 mm and 0.2 mm nozzles at both 69 and 250 MPa have yielded cutting speeds on 12 mm thick steels similar to those predicted by the model [107].

All material tested has been modelled as deformation wear occurring by brittle fracture, thus being proportional to E/10. A comparison of the relative cutting performacne of materials and their static material properties shows that, for 'pure', un-alloyed materials the cutting performance is indeed similar to the ratio of Youngs modulus, figure 5.21. For materials with similar values of E, e.g. mild steel and 304L, further classification based on ultimate yield strength predicts cutting performance in approximately the correct ratios. However, as figures 5.21 to 5.23 show, no one material property is adequate in explaining cutting performance.

The results on other steels are not in such good agreement. The martensitic steel 17-4PH, although having almost twice the tensile strength as 304L, is no more difficult to machine by conventional methods, and yet its hardness is also two or three times as great. Its ductility is also relatively low, negating the use of this material property as a gauge of cutting performance. This material is also known to be easily machinable. Machinability, however, is not a single measurable property of a material, and attempts to represent the relative machinability of various materials in terms of physical properties are only partially successful.

Conditions of the material which may determine machinability are: composition, heat treatment and microstructure. The measurable mechanical properties of hardness, tensile strength and ductility give some indication of the machining properties to be expected, but cannot distinguish between, say, the machinability of a free-cutting mild steel and of an austenitic stainless steel having somewhat similar mechanical test properties.

Some significant facts relating to the machinability are given below:

a) Hardness. Steels up to 300 HB do not present great machining difficulties unless large amounts of alloying materials are present. Some materials, notably manganese steels (manganese contents 12-14%) and alloys of the nimonic series, have pronounced work-hardening properties which influence machinability. Indentation

hardness tests may give values below 200 HB, which does not suggest any difficulty will be encountered when machining.

Chip formation, however, involves "working" of the material and hardness might therefore increase considerably during cutting from this cause. The machinability of plain carbon steels, for instance, falls steadily as the carbon content rises.

b) Micro-structure. Banded structures, such as occurs with layers of pearlite and ferrite, do not machine well. Fine grained materials also have an increased resistance to machining. High-carbon steels may be machined at greater metal-removal rates if annealed or spheroidised; the resulting surface finish is not very good, however.

c) Composition. High-nickel-chrome alloy steels are hard to machine due to their toughness, a combination of high strength with relatively high ductility. Under such conditions, the amount of work to be done on the material necessary to cause plastic shear resulting in chips must be large. The 18/8 type of austenitic stainless steel is difficult to machine because the originally ductile material can transform to the harder martensite under applied cutting stresses. For such conditions the cutting edge of a conventional cutting tool is kept beneath the surface of the material. Rubbing, without producing a chip, may so work harden the surface that it is almost impossible to get a tool to penetrate the hard skin formed.

d) Free machining properties. Inclusions of a weaker insoluble material, such as manganese sulphide in a mild steel, considerably increase machinability both in regard to metal removal rates and the resulting surface finish. The inclusions give rise to local weaknesses which, under the cutting forces, increase stress concentration and thus cause failure at the lower force values. Such inclusions cause a small reduction of mechanical properties only and the free machining steels are of a considerable economic importance in bar turning on automatic lathes.

Figure 5.21 Variation of cut depth with Youngs modulus

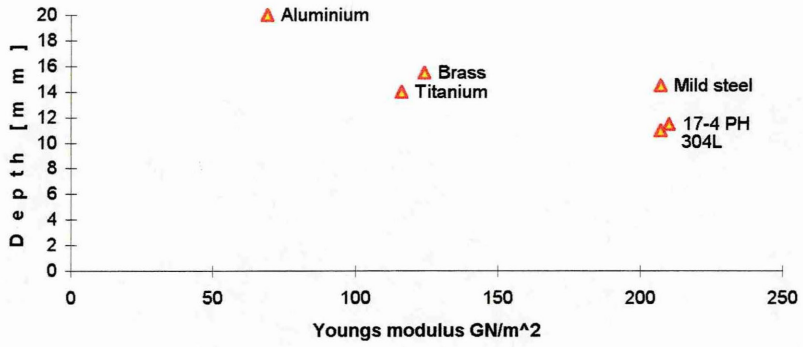

Figure 5.22 Variation of cut depth with yield strength

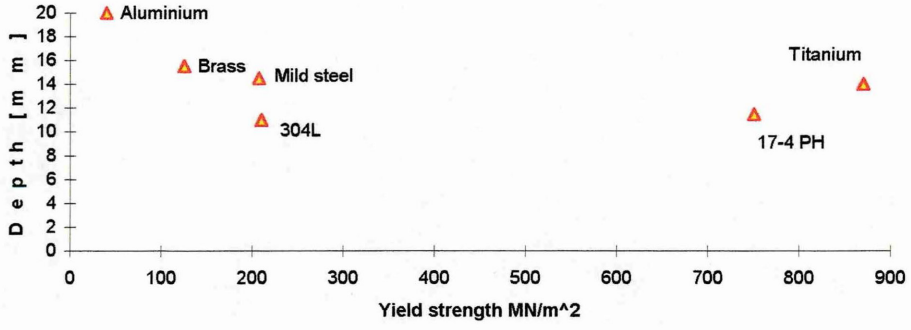

Figure 5.23 Variation of cut depth with ultimate strength

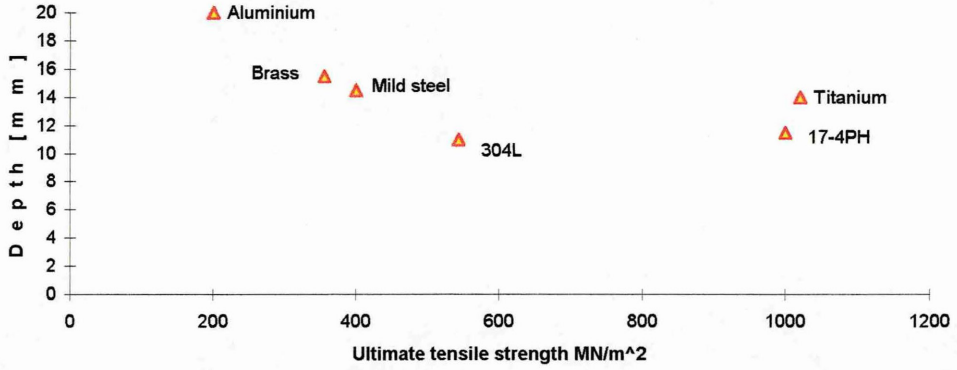

Numerous manganese sulphide inclusions occur in steels having higher than normal amounts of sulphur (0.2% in place of 0.04%) to which manganese of about five times this amount is necessary to prevent the formation of the very weakening ferrous sulphide at the grain boundaries. The introduction of small amounts of lead, 0.15-0.35% in steels, 1-3% in brasses and bronzes, is effective in improving machinability for similar reasons.

A similar comparison of material properties to erosion rates has been carried out by Sundararajan [110]. Again the conclusions were that quasi-static material properties are of little use in quantifying the relative erosion resistence of a material.

It is apparent that dynamic material properties must be employed to assess the erosion or machinability of materials. This area has received much attention recently due to the interest in high temperature erosion-corrosion of materials, for instance for turbine blades [81-82, 110, 111]. The significant variation in material properties with temperature alone require investigation of dynamic values. The majority of the models employed in this area are based on material fatigue [4, 81, 110]. The concept of plastic deformation of a top layer of the material is common to all models, and similar to Bitters deformation mode as used here [1]. Thus the findings should be relevant to the mechanisms described here.

Even without an accurate value of cutting performance for all material, which can be gained after just one test cut, the model is still proving useful in its original objective of assisting the analysis and development of cutting systems. Figures 5.25 to 5.26 show the effect of varying pressure and abrasive flow rate on cutting performance. It can be seen that an increase in pressure does not correspond to a similar increase in cut depth, all else being equal.

A similar less-than-unity trend is seen when abrasive flow rate is increased, figure 5.25. However, by monitoring the cut speed required to obtain the same cut depth, the performance increase is almost unity, figure 5.26. The fact that it is slighlty less than unity is due to the higher density of particles reducing the suspension velocity, thus each particle

is less efficient. The implications of changes in operating conditions are more readily seen by examining the cut surface area generated, i.e. the product of the cut speed and the depth of cut. As can be seen in the sample analysis of appendix C, a threshold condition exists. Such analysis can be used to optimise operations such as milling and etching, by carrying out multiple passes at the optimum operating conditions.

To date, the model has been used successfully to predict cutting performance for systems operating at pressures of up to 250 MPa, with nozzle sizes down to 0.2 mm. This work has secured funding to build a research system to carry out cutting trials at these operating conditions. Both system and model are being used in parallel to develop manipulation stratagies.f

The model will be incorporated into an existing database of cutting results and used to provide predictions for cutting times, and thus costs, for abrasive water jet systems in the jobbing shop market. In addition, the performance predictions reduce the amount of trials necessary before quality cuts can be produced.

Figure 5.24 Variation of cut depth with pressure at 100 mm/min and 100 gm/min olivine

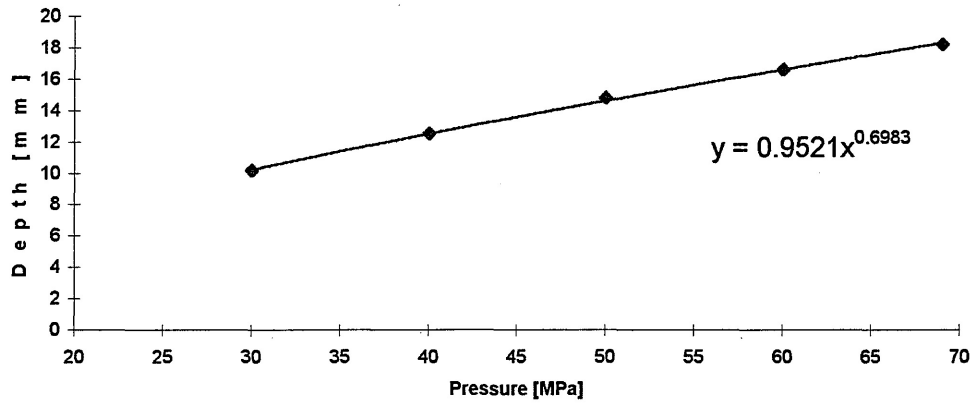

Figure 5.25 Variation of cut depth with abrasive flow rate for 69 MPA and 100 mm/min

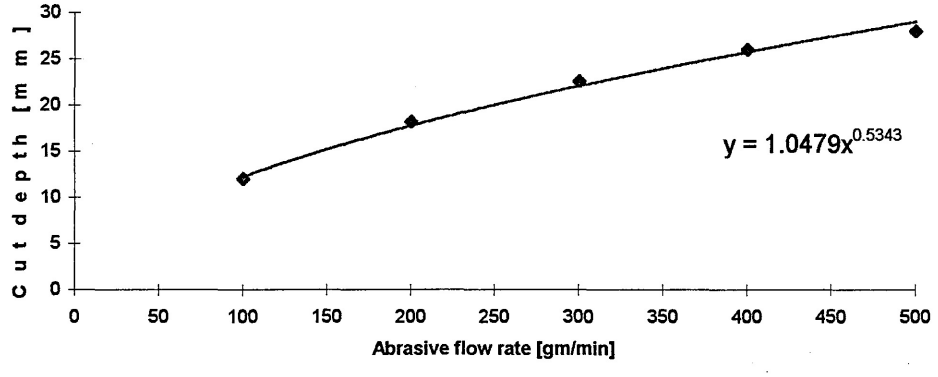

Figure 5.26 Variation of cut speed with abrasive flow rate for 69 MPa and 12 mm depth

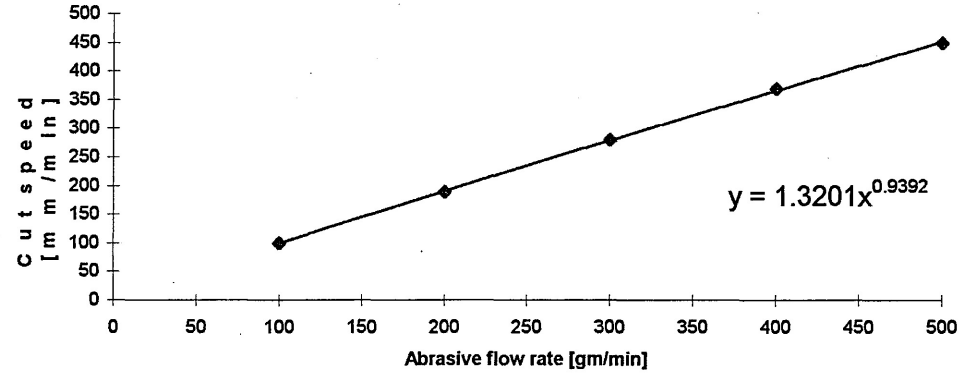

CHAPTER 6 - CONCLUSIONS AND RECOMMENDATIONS

1. Abrasive water jet cutting of ductile material consists of erosion by solid particle impact. Two main modes of erosive wear occur, distinguished by the angle of attack of the particle and the material.

2. For particle impacts at angles less than 20° a mechanism of micro-machining similar to single point cutting tools takes place. This involves the shearing of material and its value is dependent on the tensile strength of the material.

3. At larger impact angles, up to normal (90°) the material is subject to deformation wear. This is the work-hardening of the surface with subsequent fracture. The fracture mechanism is crack growth by brittle fracture. Brittle fracture is caused by tensile failure and has a theoretical value of E/10.

4. Only a fraction of the particles are involved in the cutting wear mode. This fraction depends on material properties. These particles are assumed to be reaccelerated within the jet, thus all particles contribute to the deformation wear mode.

5. A threshold velocity exists below which no erosion can take place. This value is dependent on the tensile stress of the material, as proposed by Bitter [1].

6. A mathematical model of suspension jet awj cutting has been derived from the theory of erosive wear.

7. This model has been verified against a range of cutting conditions. Dynamic material properties need to be investigated for accurate prediciton of all materials.

8 Sub 100 μm abrasive particles have been successfully used to cut material, with no noticeable performance drop.

9. Over the relatively short distance of the abrasive water jet nozzle, the high pressure water produces a near-supersonic jet giving rise to forces on the abrasive particle far greater than the traditional Stokes drag force.

10. The inertial forces accelerate the particles close to the water velocity by the end of the convergent section of a typical abrasive water jet nozzle. Shorter (5 diameter) parallel sections are adequate, if they give an acceptable wear life.

11. The particle exit velocity can be approximated by the ideal slurry velocity as given by Bernoulli's equation.

12. For further validation of the model, a means of continually monitoring the abrasive discharge rate is necessary.

BIBLIOGRAPHY

1. Sarker A D. 1976. Wear of materials. Pergammon press, Oxford.
2. "Cutting by sand-water jets from a fluidised bed". In; *Proceedings of the 10th International conference on jet cutting and cleaning technlogy* pp 24 -251, Cambridge.
3. You Ming-qing. et. al. (1993). "Study on a direct injection abrasive jet system". In: *7th American Water Jet Conference*, 28-31 August, 1993, Seattle, Washington, 295-305.

REFERENCES

1 Bitter J. G. A. (1963). "A study of erosion phenomena". Wear, vol. 6, pp. 5-21, 169-190.

2 Finnie I. (1958). The mechanism of erosion of ductile metals. In: *ASME proceedings of the 3rd National Congress of Applied Mechanics*, New York, pp. 527-532.

3 Kragelsy I.V. et al. (1985). "Theory of material wear by solid particle impact - a review". Tribology International. vol 18, no. 1, pp. 3-11.

4 Hutchings I.M. (1981). "A model for the erosion of metals by spherical particles at noraml incidence". Wear Vol. 70 no. 3, pp. 269-282.

5 Tilly G.P. (1973). "A two stage mechanism for ductile erosion". Wear, vol. 23, pp. 87-96.

6 Fairhurst R M, "Abrasive water jet cutting", MSc Thesis, Cranfield Institute of Technology, 1982.

7 Hashish M. (1989). "A model for abrasive waterjet (AWJ) machining", Journal of Engineering Materials and Technology, vol. 111, April 1989, pp. 154-162.

8 Guo C. et. al. (1993). Mathematical modelling of the accelerating process of particles in DIA-JET. In: *7th American Water Jet Conference*, 28-31 August, 1993, Seattle, Washington, pp. 287-293.

9 Shimizu S. and Z. Wu. (1994). Erosion due to premixed abrasive water jet. In: *12th International Conference on Jet cutting Technology*, Rouen, France, 25-27 October 1994, pp. 3-15.

10 Norwood J. A. (1984). New adaptions and applications for waterknife cutting. In: *7th International Symposium on jet cutting technology*, Ottawa, Canada, 26th-28th June 1984, pp. 369-389.

11 Bury L. et. al. (1974). Steam boosted water jet cleaning at 300 bar.In: *Proc. 2nd Int. Symp. on Jet Cutting Technology*, Cambridge, Apr 2-4 1974, F1-F10.

12 Pekarek J. L. et. al. (1963). "Hydraulic jetting - some theoretical and experimental results". Society of Petroleum Engineers Journal. pp. 101-112.

13 Brown R. (1981). *Jet Cutting Technology - a review and bibliography*. BHRA Fluid Engineering, Cranfield.

14 Higginbotham R. (1988). *Jet Cutting and Cleaning Bibliography*. Elsevier Applied Science Publishers.

15 Wakefield A. W. (1989). *An introduction to the jet pump*. A W Wakefield, Stanford, 4th edition.

16 Patent no WO 86/06311. Abrasive Fluid Flow.

17 Hollinger R. H. et. al. (1989). "Precision cutting with a low pressure, coherent abrasive suspension jet". In: *Proc. 5th American Water Jet Conf. Toronto*, Canada.

18 ASTM: G40-83. Standard terminology relating toerosion and wear. Philadelphia.

19 De Haller P. (1939). `Erosion und Kavitations-erosion'. In: Bitter, J. G. A. (1963). "A study of erosion phenomena - part I". Wear, Vol. 6, pp. 5-21.

20 Wellinger R. (1949). In: Bitter, J. G. A. (1963). "A study of erosion phenomena - part I". Wear, Vol. 6, pp. 5-21.

21 Wellinger K. and H. Uetz. (1957). Wear, vol. 7, pp. 225-231.

22 Holtey H. (1939). In: Bitter, J. G. A. (1963). "A study of erosion phenomena - part I". Wear, Vol. 6, pp. 5-21.

23 Finnie I. (1960). `Erosion of surfaces by solid particles'. Wear, Vol. 3, 87-103.

24 Winter R.E. and I.M. Hutchings. (1974). Wear, vol. 29, pp. 181-194.

25 Hutchings I.M. (1979). Mechanisms of the erosion of metals by solid particles. In: *Erosion: Prevention and useful applications*, 24th-26th October 1977, Vail, Colorado, pp. 59-74.

26 Maji J. and Sheldon, G.L. (1979). Mechanisms of erosion a ductile material by solid particles. In: *Erosion: Prevention and useful applications*, 24th-26th October 1977, Vail, Colorado, pp. 136-146.

27 Smeltzer G.E. et. al.. (1970). J. Basic Eng. ASME Trans, vol. 92, pp. 639-654.

28 Jennings W.H., W.J. Head, and C.R Manning Jr. (1976). ` A mechanistic model for the prediction of ductile erosion'. Wear, vol. 40, pp. 93-112.

29 Winter R.E. and Hutchings, I.M. (1975). Wear, vol. 34, pp. 141-148.

30 Bellman R, A. Levy. (1981). Wear of Materials, ASME, New York, pp 564-576.

31 Levy A. V. (1983). In: *Proceedings 6th International Conference on Erosion by Liquid ans Solid Impact*, Cambridge, September 1983.

32 Kragelsky I.V. (1968). *Friction and Wear.* Moscow. pp. 285-293.

33 Zolotar A.I. (1979) In: Kragelsy I.V. et al. (1985). "Theory of material wear by solid particle impact - a review". Tribology International. vol 18, no. 1, pp. 3-11.

34 Cousens A. K., and I.M. Hutchings. (1983). Wear of materials, ASME, New York, pp. 382-389.

35 Edington J. W. and I. G. Wright. (1978) Wear, Vol. 48, pp 131-14 and 145-155.

36 Rickerby D. G. and N. H. MacMillan. (1979) In: *Proc. 5th Int. Conf. on Erosin by Solid and Liquid Impact*, Cambridge, September 1979.

37 Rickerby D. G. and N. H. MacMillan. (1980). Wear, Vol. 60, pp. 369-382.

38 Rickerby D. G. and N. H. MacMillan. (1981). Wear of Materials, ASME, New York, pp. 548-563.

39 Hutchings I. M. (1979). In: *Proc. 5th Int Conf on Erosin by Solid and Liquid Impact*, Cambridge, September 1979.

40 Shewmon P. G. (1979). In: *Proc. 5th Int .Conf. on Erosin by Solid and Liquid Impact*, Cambridge, September 1979.

41 Sink N. C. (1978). The Response of Metal Single Crystals to Solid Particle Impact, M.S. Thesis, Pensylvania State University.

42 Evans A.G, and T.R. Wilshaw. (1976). Quasi-static solid particle damage in brittle solids, 1. Observations, analysis and implications. Acta Metallica, Vol. 24, 939-956.

43 Evans A. G., and T. R. Wilshaw. (1977). Dynamic solid particle damage in brittle materials. Journal of Material Science, Vol. 12, pp. 97-116.

44 Hertz H. (1896). On the contact of elastic solids. In: Evans, A. G. , and T. R. Wilshaw. Journal of Material Science, Vol. 12, pp 97-116

45 Sheldon G. L. and I. Finnie. (1966). "On the ductile behaviour of normally brittle materials during erosive cutting", Journal of Engineering for Industry. Volume 88, 1966, pp. 387-392.

46 Sargent G. A. et al. (1977). Erosion: Prevention and Useful Application, ASTM STP 664.

47 Evans A. G. (1979). Erosion, Vol. 16, Academic Press, New York, pp. 1-65.

48 Budinski K. G., and H. Chin. (1983). Wear of Materials, ASME, New York, pp. 311-324.

49 Misra A., and I. Finnie. (1981). Wear, Vol. 65, pp. 359-373.

50 Sheldon G. L., and A. Kanhere. (1972). An investigation of impingement erosion using single particles. Wear, Vol. 21, pp. 195-209.

51 Hashish M. (1984). "A modelling study of metal cutting with abrasive water jets". Journal of Engineering Materials and Technology, vol. 106, pp.88-100.

52 Gulden M. E. (1977). Erosion: Prevention and Useful Application, ASTM STP 664, 1977.

53 Miller D. S., E. Claffey, T. Grove. (1996). *Technology package for abrasive waterjet machining*. HMSO.

54 Saunders D. H. (1989). *Invesigation of Diajet abrasive jet cutting for size reduction and decommissioning*. BHRA, Cranfield.

55 Capello E. et al. (1994). On the characteristics of surfaces obtained by abrasive water jet machining. In: *12th International Conference on Jet cutting Technology*, Rouen, France, 25-27 October 1994, pp. 3-15.

56 Hashish M. (1993). On the modelling of surface waviness produced by abrasive waterjets, In: *Jet cutting technology - proceedings of the 11th conference*, pp.171-5.

57 White F. M. (1991). *Viscous Fluid Flow*. McGraw-Hill, New York.

58 Abudaka (1989). Development of a high pressure abrasive waterjet cutting system. Doctoral Dissertation,London University, 1989.

59 Massey B. S. (1984). *Mechanics of Fluids*. 5th Edition. Van Nostrand Reinhold (UK) Co. Ltd.

60 Newton I. (1687). *Principa*. In: *McCormack P. D. and L Crane. (1973). Physical Fluid Dynaics. Academic Press.*

61 Stokes G. G. (1851). On the effect of the internal friction of fluids on pendulums. Mathematical and Physical Papers, Vol. 3, no 1.

62 Oseen C. W. (1927). *Hydrodynamik*. Leipzig. In: Tchen C. M. (1947).

63 Tchen C. M. (1947). *Mean value and correlation problems connected with the motion of small particles suspended in a turbulent flow*. Doctoral Disertation. Delft.

64 Basset A. B. (1888). *A Treatsie on Hydrodynamics, Vol. 2*. Deighton, Bell and Co. Cambridge.

65 Maxey M. R. and J. J. Riley (1983). "Equation of motion for a small rigid sphere in a nonuniform flow". Phys Fluids. Vol. 26, no 4, pp. 883-889.

66 Coulson J. M.and J. F. Richardson. (1977). *Chemical Engineering, Volume 1*, 3rd edition. Oxford. Pergamon.

67 Rittenhouse G. (1943) J. Sedimentary Pertrology. vol. 13, no. 2, pp. 75-81

68 Bond R. K. (1957). Chemical Engineering, vol. 64, October 1957.

69 Finnie I. (1972). "Some observations on the erosion of ductile metals." Wear. Volume 19. pp. 81-90

70 Finnie et al. (1977). Erosion: Prevention and Useful Application, ASTM STP 664, pp. 36-58, 1977.

71 Finnie I. and D. H.McFadden. (1978). "On the velocity dependence of the erosion of ductile materials by soild particles at low angles of incidence". Wear Vol. 48, pp. 181-190,

72 Hertz (1940).In: Bitter J. G. A. (1963). "A study of erosion phenomena - part I". Wear, Vol. 6, 5-21.

73 Tabor D. (1951). *The hardness of metals.* Oxford University Press.

74 Davies In: Bitter J. G. A. (1963). "A study of erosion phenomena - part I". Wear, Vol. 6, 5-21.

75 Andrews (1929). In: Bitter J. G. A. (1963). "A study of erosion phenomena - part I". Wear, Vol. 6, 5-21.

76 Andrews (1930). In:Bitter J. G. A. (1963). "A study of erosion phenomena - part I". Wear, Vol. 6, 5-21.

77 Neilson J. H., and A. Gilchrist. (1968). An analytical and experimental investigation of the velocities of particles entrained by the gas flow in nozzles. J. Fluid Mech. vol 33, part 1, pp. 131-149.

78 Goodwin et. al. (1969). A study of erosion by solid particles. In: *Proc. Inst. Mech. Engrs*, vol 184, no 15, pp. 279-298.

79 Meyer. In: Sheldon, G. L., and A. Kanhere. (1972). An investigation of impingement erosion using single particles. Wear, Vol. 21, pp. 195-209.

80 Zeng J. and T. J.Kim. (1989). "Material removal kinetics of Advanced Ceramics by a high pressure Abrasive Waterjet",In: *First International Symposium of the society for the Advancement of Materials and Process Engineering*, Chiba Japan.

81 Stephenson D.J. (1989). Erosion behaviour of materials in gas turbines. *Corros. Sci* no. 29, pp. 647-656.

82 Nicholls J.R., and D.J. Stephenson. (1995). "Monte Carlo modelling of erosion processes" *Proc. 8th International Conf on erosion by liquid and solid impact,* In:Wear Vol 186-187, pp. 64-77.

83 Walters C L and D. H. Saunders. (1990). "Diajet cutting for nuclear de-commissing", Chapter 29, In: *Jet cutting technology - Proceedings of the 10th International conference*, 1990, Amsterdam, pp. 427-440

84 Kim T. J. and J. L. Labus. (1993). *Abrasive Water Jetting Technology*. section 3. The Water Jet Technology Association, Missouri.

85 BRITE BE-4382. (1995). *Precision machining using abrasive water jets.* Final technical report.

86 Nadeau E. et al. (1991). The influence and role of abrasive velocity in abrasive water jet cutting. International Journal of water jet technology. vol. 1, No 3, pp. 109-117.

87 Benchaita M. T. et. al. (1983). "Erosion of metallic plate by solid particles entrained in a liquid jet". Journal of Engineering for Industry, vol. 115, pp. 215-222.

88 Blevin R. D. (1984). *Applied fluid dynamics handbook.* Van Nostrand Reinhold Company, New York.

89 Hashish, M. (1993). "Comparitive evaluation of abrasive liquid jet machining systems". Journal of Engineering for Industry. Vol. 115, 44-50

90 ISQ. (1995). Final Year Report. In: BRITE BE-4382. (1995). *Precision machining using abrasive water jets.* Final technical report.

91 Sheldon G. L. and I. Finnie. (1966). "The mechanism of material removal in the erosive cutting of brittle materials". Journal of Engineering for Industry, November. pp. 393-400.

92 Finnie I. et. al. (1967). Journal Materials, volume 2, pp. 682-700.

93 Saunders D. H. (1992). Performance prediction for DIAJET abrasive jet cutting. MR 115, BHR Group, England.

94 BRITE 4382. (1993). Test specification and certificate. In: Precision machining using abrasive water jets.

95 Mitotoyo. (1995). Measured response, no 18.

96 McLean D. (1977). *Mechanical properties of metals.* Robert E Krieger.

97 Griffith (1920). In: Smallman R. E. (1985). *Modern physical metallurgy.* 4th edition. Butterworths.

98 Colangelo V. J, amd F. A. Herser. (1987). *Analysis of Metalurgical failures.* 2nd edition. John Wiley and sons.

99 Lamb H. (1932). *Hydrodynamics.* 6th edition. Cambridge.

100 Zuber N. (1964). On the dispersed two-phase flow in a laminar flow region. Chem. Eng. Soc., vol 19, pp. 897-917.

101 Einstein A. (1906) Ann. Phys., no 4, pp. 209.

102 Axon. (1994). A801 instruction manual. Axon, Isle of Wight.

103 European Patent Specification 0 276 219. Feeding abrasive material.

104 Autoclave catalogue 6000.

105 Jacobs B. (1991). *Design of slurry transport systems.* Elsevier applied sciences.

106 Claffey E. (1993). *Feasibility study in the use of DIAJET cutting equipment as a precision slot cutter*. BHR Group Ltd, Cranfield.

107 Private communique with Tony Aldridge, April 1996.

108 Neusen K. F. et. al. (1993). Measurement of particle and drop velocities in a mixed abrasive waterjet using a forward-scatter LDV system. In: *11th International Conference on Jet Cutting Technology*, 8-10 September, in St. Andrews, Scotland.

109 Burgers J. M. (1938). *2nd report on viscosity and plasticity*. Kon. Ned. Akad. Wet., Verhand. chapter 3.

110 Sundararajan. G. (1995). *Proc. 8th International Conf on erosion by liquid and solid impact,* In:Wear Vol 186-187, pp. 129-144.

111 Stack. M.M. et al. (1995). *Proc. 8th International Conf on erosion by liquid and solid impact,* In:Wear Vol 186-187, pp. 523-532.

APPENDIX A - CALCULATION OF ENERGY ABSORBED BY IMPACTING SPHERES

From studies by Hertz [72], the force of an impacting sphere on an infinitely large sphere (i.e. flat surface) is given by:

$$F_{max} = \left[\frac{20\pi}{3}\rho_p\right]^{\frac{3}{5}} r^2 \left[6\left(\frac{1-\nu_1^2}{E_1}+\frac{1-\nu_2^2}{E_2}\right)\right]^{\frac{2}{5}} v^{\frac{6}{5}}$$

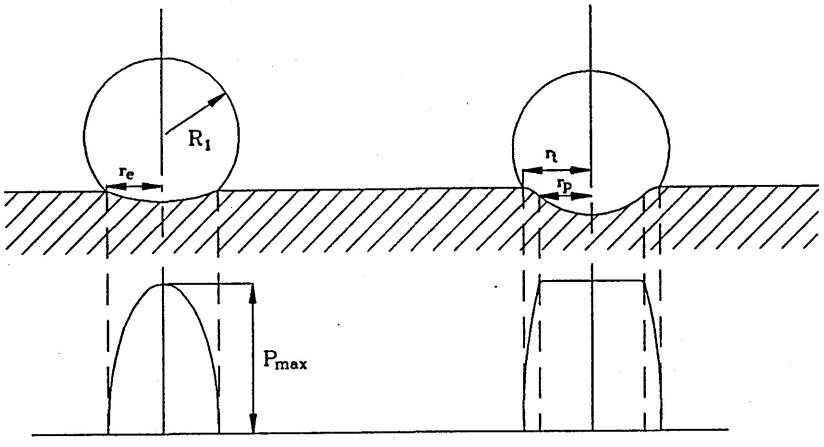

Figure A.1

Hertz also derived an equation for the radius of the projection of the contact area on the body surface (see figure A.1):

$$r_e = \left[\frac{3}{4}F_{max}r\left(\frac{1-\nu_1^2}{E_1}+\frac{1-\nu_2^2}{E_2}\right)\right]^{0.5}$$

Therefore the average surface pressure P_{av} can then be calculated from the above equations, yielding:

$$P_{av} = \frac{F_{max}}{\pi r_e^2} = \frac{2}{3}\left[\frac{40}{\pi^4}\rho_p\left(\frac{1-\nu_1^2}{E_1}+\frac{1-\nu_2^2}{E_2}\right)^{-4}\right]^{0.2} v^{0.4}$$

The average pressure is two-thirds the maximum surface pressure [72]. Therefore the elastic limit is reached when the average pressure reaches two-thirds of the elastic yield strength of the material. Substituting for σ_y and V_{el} and re-arranging yields:

$$V_{el} = \frac{\pi^2}{2\sqrt{10}} \frac{\sigma_y^{2.5}}{\rho_p^{0.5}} \left[\frac{1-\nu_1^2}{E_1} + \frac{1-\nu_2^2}{E_2} \right]^2$$

This is the minimum velocity below which no plastic deformation will occur.

The decrease in the centre of gravity between the bodies is then given by:

$$hel = \frac{\pi^2}{4} \sigma_y^2 r \left[\frac{1-\nu_1^2}{E_1} + \frac{1-\nu_2^2}{E_2} \right]^2$$

For the elastic-plastic collision, Hertz assumes the colliding sphere (particle) deforms only elastically, while the flat body deforms elastically and plastically. Also he assumed that no deformation hardening would take place, σ_y = constant.
For normal impacts elastic deformation will occur until σ_y is reached. After this point the area subjected to the yield stress increases, however, for the conditions here this area is relatively small and so the elastic compression is assumed constant in this area.

Let H be the depth of the concavity due to the plastic deformation. The total contact area is then approximately:

$$\pi r_t^2 \approx 2\pi R(H + h_{el})$$

The radius of the projection of the plastic deformed area, r_p, is thus

$$\pi r_p^2 \approx 2\pi RH$$

The area loaded elastically is:

$$\pi r_t^2 - \pi r_p^2 = 2\pi R h_{el} \approx \pi r_e^2$$

Therefore in the case of elastic-plastic impact the size of the part of the contact area subjected only to elastic deformation is independent of the size of the indentation formed and is equal to the Hertzian contact area in a perfectly elastic impact, in which $P_{max} = \sigma_y$. The preceding analysis then gives the elastic energy absorbed as:

$$Q_e = \frac{1}{2} m V_{el}^2$$

where V_{el} is as defined before.

The potential energy of the elastic deformation in the area subject to a plastic-elastic load, Qpe is:

$$Q_{pe} = \frac{1}{2} h_{el} \sigma_y \pi r_p^2$$

At the end of the first period of collision r_p has reached its maximum value and so has the elastic deformation energy. The elastic reaction forces then press the particle out of the body giving the particle an amount of kinetic energy equal to the stored elastic deformation energy resulting in a particle velocity v.

The formation of the permanent indentation requires an amount of energy equal to:

$$Q_p = \int_0^{H_{max}} \pi r_p^2 \sigma_y dH \approx \pi r H_{max}^2 \sigma_y$$

where H_{max} is the depth of the indentation after collision. As $r^2_{pmax} = 2RH_{max}$ we can write:

$$Q_{pe} = \sqrt{\frac{15}{4} Q_e Q_p}$$

Substituting into our total energy equation, re-arranging and neglecting second order terms gives:

$$Q_p \approx \left[\sqrt{Q} - \sqrt{Q_e}\right]^2$$

i.e.

$$Q_p \approx \frac{1}{2} m [V - V_{el}]^2$$

This shows that the energy transferred is directly proportional to the mass of the particle.

APPENDIX B - GOVERNING EQUATIONS FOR TWO PHASE FLOW

Multiphase flow is the simultaneous flow of several phases (states of matter, solid liquid or gaseous). In order to solve the motion of one phase relative to the other it is necessary to use a separated flow model, allowing different properties (velocity etc.) for each phase.

However, in considering the practical situation of multiple particles and wall effects, the flow can be modelled analytically by homogenous methods, treating the phases as a sort of pseudo-fluid. This leads to a modified value of viscosity and density, for instance.

Considering a suspension of particles in fluids, no surface tension, sub-division, or distortion is assumed significant so the basic model is simpler to develop. The particle shape will be considered spherical to further simplify the model, and agglomeration and inter particle forces will be neglected. Complications due to non-uniform flow patterns will be considered however. The main forces of interest are due to pressure, inertia, and interfacial drag. The basic equations governing the flow pattern are the conservation of mass and the conservation of momentum.

For incompressible flow, the conservation of mass (equation of continuity) is simplified to

$$div\, V = \nabla . V = 0 \qquad \text{B.1}$$

The conservation of momentum, or Newton's second law, equates the applied force(s) and the resultant acceleration of the particle. These applied forces may be sub-divided into surface forces and body forces. In this instance, as in most, the only body force to be considered is gravity. The surface forces arise from the stresses on the surface of the particle. This can be shown to be [57]:

$$\vec{f}_{sur} = \nabla . \sigma_{ij} = \frac{\partial \sigma_{ij}}{\partial x_j} \qquad \text{B.2}$$

where

$$\sigma_{ij} = -p\,\delta_{ij} + \mu\left(\frac{\partial u_i}{\partial x_j} + \frac{\partial u_j}{\partial x_i}\right) + \delta_{ij}\lambda\, div\, V \qquad \text{B.3}$$

σ_{ij} is the stress tensor, δ is the Kronecker delta function

Substituting the above forces into the force balance yields the equation of motion, called the Navier-Stokes equation

$$\rho \frac{DV}{Dt} = \rho g - \nabla p + \frac{\partial}{\partial x_j}\left[\mu\left(\frac{\partial u_i}{\partial x_j} + \frac{\partial u_j}{\partial x_i}\right) + \delta_{ij}\lambda \, div\, V\right] \qquad \text{B.4}$$

For incompressible flow and assuming μ is constant, σ_{ij} simplifies to $\sigma_{ij} = -p\delta_{ij} + \mu\left(\frac{\partial v_i}{\partial x_j} + \frac{\partial v_j}{\partial x_i}\right)$
Thus the Navier Stokes equation becomes

$$\rho \frac{DV}{Dt} = \rho g - \nabla p + \mu \nabla^2 V \qquad \text{B.5}$$

A further limitation is that the fluid velocity matches the particle velocity V(t) and angular velocity $\Omega(t)$ on the surface. This 'no-slip' condition is mathematically represented by:

$$v = V + \Omega X \, [x - Y(t)] \qquad \text{B.6}$$

The above equations are applied to a small rigid particle (sphere) of radius r located at y(t) in the fluid flow which in the absence of the particle would have a velocity u(x,t). The presence of the particle and its motion through the fluid will modify the flow locally and lead to a new flow field v(x,t). This modified flow field must satisfy the condition $v(x,t) - u(x,t)$ as $|x - Y(t)| \to \infty$ for an incompressible flow of uniform density. The equation of motion for the particle can be written as:

$$m_p \frac{dV_i}{dt} = m_p g_i + \oint_s \sigma_{ij} n_j \, dS$$

i.e. over the surface of the particle and n is the unit outward normal.

To solve the fluid mechanics problem it is convenient to make a change of co-ordinates to a frame moving with the centre of the particle. The changes of variable are:

$$z = x - Y(t) \quad and \quad x(z,t) = v(x,t) - V(t)$$

The equations now become:

$$\frac{\partial w_i}{\partial z_i} = 0$$

$$\rho\left(\frac{\partial w_i}{\partial t} + w_j \frac{\partial w_j}{\partial z_j}\right) = \rho\left(g_i - \frac{dV_i}{dt}\right) - \frac{\partial p}{\partial z_i} + \mu \frac{\partial^2 w_i}{\partial z_j^2}$$

$$wv = \Omega X\ [z] \text{ for } |z| < r$$

$$w = u - V \text{ as } |z| \to \infty$$

The stress tensor can be expressed similarly as:

$$\sigma_{ij} = -p\,\delta_{ij} + \mu\left(\frac{\partial w_i}{\partial z_j} + \frac{\partial w_j}{\partial z_i}\right)$$

In order to solve these equations the flow field is split into two parts, namely the undisturbed flow $w^{(0)}$ without application of the boundary condition and the disturbance flow $w^{(1)}$ set up by the particle [65]. Collecting each term separately yields the equations of motion as:

$$\rho\left(\frac{\partial w_i^{(0)}}{\partial t} + w_j^{(0)} \frac{\partial w_j^{(0)}}{\partial z_j}\right) = \rho\left(g_i - \frac{dV_i}{dt}\right) - \frac{\partial p^{(0)}}{\partial z_i} + \mu \frac{\partial^2 w^{(0)}{}_i}{\partial z_j^2} \qquad \text{B.7}$$

$$\rho\left(\frac{\partial w_i^{(1)}}{\partial t} + w_j^{(0)} \frac{\partial w_i^{(1)}}{\partial z_j} + w_j^{(1)} \frac{\partial w_i^{(0)}}{\partial z_j} + w_j^{(1)} \frac{\partial w_j^{(1)}}{\partial z_j}\right) = -\frac{\partial p^{(1)}}{\partial z_i} + \mu \frac{\partial^2 w^{(1)}{}_i}{\partial z_j^2} \qquad \text{B.8}$$

with each separately satisfying the incompressibility equation.

Forces arising from the undisturbed flow field

The contribution from the undisturbed flow can be quite generally determined from substituting the stress tensor into the particle equation of motion, yielding:

$$F_i^{(0)} = \oint_s n_j \left[-p^{(0)} \delta_{ij} + \mu \left(\frac{\partial w_i^{(0)}}{\partial z_j} + \frac{\partial w_j^{(0)}}{\partial z_i} \right) \right] \qquad \text{B.9}$$

Using the divergence theorem of Gauss, this may be converted to a volume integral and calculated from

$$F_i^{(0)} = \oint_V \nabla . \sigma_{ij} \, dV$$

From equation B.2 this is $f_{str} = \nabla . \sigma_{ij} = \frac{\partial \sigma_{ij}}{\partial x_j}$. Assuming that the particle (sphere) is so small that the stress can be taken as constant across it's surface, this volume integral yields $F_i^{(0)} = \frac{4}{3} \pi r^3 \left(\frac{\partial p^{(0)}}{\partial z_i} + \mu \frac{\partial^2 w_i^{(0)}}{\partial z_j^2} \right)$

Combining this with the equation of motion for the undisturbed flow equation B.9, we get:

$$F_i^{(0)} = -m_f g_i + m_f \left(\frac{dV_i}{dt} + \frac{\partial w_i^{(0)}}{\partial t} + w_j^{(0)} \frac{\partial w_j^{(0)}}{\partial z_j} \right)$$

or in terms of the undisturbed flow u(x,t) in the original frame of reference:

$$F_i^{(0)} = -m_f g_i + m_f \left(\frac{\partial u_i}{\partial t} + u_j \frac{\partial u_j}{\partial z_j} \right) \qquad \text{B.10}$$

Noting that

$$\left. \frac{Du_i}{Dt} \right|_{Y(t)} = \left(\frac{\partial u_i}{\partial t} + u_j \frac{\partial u_i}{\partial x_j} \right)_{x=Y(t)} \qquad \text{B.11}$$

the second term on the right hand side of equation B.10 can be replaced with the complete derivative $\frac{D}{DT}$.

Force from the unsteady Stokes flow

A scale analysis of the disturbance flow equation B.7 reveals that, for low Reynolds number, the advective terms may be neglected [65]. This reduces the problem to one of an unsteady Stokes flow.

Equation B.7 then simplifies to: $\rho \frac{\partial w_i^{(1)}}{\partial t} = -\frac{\partial p^{(1)}}{\partial z_i} + \mu \frac{\partial^2 w^{(1)}_i}{\partial z_j^2}$ for low relative Reynolds number.

Consider two unsteady Stokes flow fields u(x,t) and u'(x,t) in some volume V bounded by a surface S. As before:

$$\rho \frac{\partial u_i}{\partial x_j} - \frac{\partial \sigma_{ij}}{\partial x_j} = 0$$

$$\sigma_{ij} = -p\delta_{ij} + \mu\left(\frac{\partial v_i}{\partial x_j} + \frac{\partial v_j}{\partial x_i}\right)$$

$$\frac{\partial u_i}{\partial x_i} = 0$$

The volume integral of the Laplace transforms

$$\int_V \left(\hat{u}_i \frac{\partial}{\partial x_j}\hat{\sigma}_{ij} - \hat{u}_i \frac{\partial}{\partial x_j}\hat{\sigma}_{ij}\right) dV$$

leads to the equation:

$$\oint_s dS(\hat{u}_i \hat{\sigma}'_{ij} - \hat{u}'_i \hat{\sigma}_{ij}) m_j$$
$$= -\int_V dV \rho [u_i(x,0)\hat{u}'_i(x,s) - u'_i(x,0)\hat{u}_i(x,s)] \qquad \text{B.12}$$

where m is the outward normal. Provided the flows tend to zero far from the sphere, the integral over the surface at infinity will make no contribution. The surface integral then reduces to an integral over the surface of the sphere. The flow field u' is required to satisfy the boundary conditions

$$\begin{gathered} |u'| \mapsto 0 \ as |x| \to \infty \\ \hat{u}'(x,s) = (1,0,0)0n|x| = a \\ u'(x,t \le 0) = 0 \end{gathered} \qquad \text{B.13}$$

the origin being the centre of the sphere. The flow u' corresponds to the fluid motion

resulting from the sphere starting from rest and having an impulse velocity [δ(t),0,0]. The symmetry relationship then gives a method for evaluating the force on the sphere from the flow field as

$$\hat{F}_1 = \oint_s \hat{\sigma}_{ij} n_j dS = \oint_s \hat{u}_i \hat{\sigma}'_{ij} n_j dS + \int_V \rho u_i(x,0)\, \hat{u}'_i(x,s) dV \qquad \text{B.14}$$

where n is the unit normal out of the sphere. Similar results hold for the other components.

The flow u' can be found by adapting the unsteady Stokes flow solution of Burgers [109]. If $e^{(1)}$ denotes the unit vector (1,0,0)

$$\hat{u}' = (e^{(1)}.\nabla)\nabla\hat{\psi} - e^{(1)}\nabla^2\hat{\psi},$$
$$\hat{\psi}(r,s) = \frac{Q_1}{\rho s r} + \left(\frac{Q_2}{r}\right)e^{-\lambda r}$$

where $\lambda^2 = \rho s/\mu$, Re(λ) is taken as positive, and r is the radial disturbance from the origin. The boundary conditions give:

$$Q_1 = \frac{3}{2}a\mu(1 + \lambda a) + \frac{1}{2}a^3\rho s,$$
$$Q_2 = -\frac{3}{2}\left(\frac{a\mu}{\rho s}\right)e^{\lambda a}$$

and the surface of the sphere (r = a)

$$\hat{\sigma}'_{ij} n_j = -\frac{1}{2}a\rho s x_i x_j \frac{e_j^{(1)}}{a^2} - \frac{3}{2}\frac{\mu}{a(1 + \lambda a)e_i^{(1)}} \qquad \text{B.15}$$

For a flow field that is initially zero everywhere, and on the sphere has the form

$$\hat{u}_i(x,s) = \hat{A}_i + x_j\hat{B}_{ij} + \frac{1}{2}x_j x_k \hat{C}_{ijk}$$

$$\hat{F}_i = -\hat{A}_1[6\pi a\mu(1+ \lambda a) + \frac{1}{2}m_f s] - a^2[(\hat{C}_{ijj} + 2\hat{C}_{jji}) + \pi\mu a(1 + \lambda a) + \frac{1}{20}m_f s\hat{C}_{ijj} \qquad \text{B.16}$$

The inverse Laplace then gives the force, with (λa) yielding the usual Basset history integral. The boundary conditions yields values for the coefficients of:

$$A_i = V_i(t) - u_i[Y(t),t],$$
$$C_{ijk} = -\left.\frac{\partial^2 u_i}{\partial x_j \partial x_k}\right|_{Y(t)} \qquad \text{B.17}$$

Combining this solution with equations B.10 and B.11 yields the total equation of particle motion as:

$$\begin{aligned} m_p\frac{dV_i}{dt} &= (m_p - m_F)g_i + m_f\left.\frac{Du_i}{Dt}\right|_{Y(t)} \\ &- \frac{1}{2}m_f\frac{d}{dt}[V_i(t) - u_i[Y(t),t] - \frac{1}{10}a^2\nabla^2 u_i\Big|_{Y(t)}] \\ &- 6\pi a\mu[V_i(t) - u_i[Y(t),t] - \frac{1}{6}a^2\nabla^2 u_i\Big|_{Y(t)}] \qquad \text{B.18} \\ - 6\pi a^2\mu\int_0^t d\tau &\left(\frac{d/d\tau(V_i(\tau) - u_i[Y(\tau),\tau] - \frac{1}{6}a^2\nabla^2 u_i|_Y(t))}{\sqrt{\pi\nu(t-\tau)}}\right) \end{aligned}$$

APPENDIX C EXAMPLE OF MATHEMATICAL MODEL CALCULATION

$x := 0..7$

$bar \equiv (10^5) \cdot Pa$ $\mu m \equiv 10^{-6} \cdot m$

$$V_d := \frac{\pi^2 \cdot 1}{2 \cdot \sqrt{10}} \cdot (\sigma_y \cdot 3.2)^{\frac{5}{2}} \cdot \left(\frac{1}{\rho_p}\right)^{\frac{1}{2}} \cdot \left(\frac{1 - \nu_1^2}{E_1} + \frac{1 - \nu_2^2}{E_2}\right)^2$$

$$V_e := \frac{\pi^2 \cdot 1}{2 \cdot \sqrt{10}} \cdot (\sigma_{ult} \cdot 3.2)^{\frac{5}{2}} \cdot \left(\frac{1}{\rho_p}\right)^{\frac{1}{2}} \cdot \left(\frac{1 - \nu_1^2}{E_1} + \frac{1 - \nu_2^2}{E_2}\right)^2$$

Relative densities $s := \frac{\rho_p}{\rho_w}$ $s = 2.8$

Water velocity $Vj := Cv \cdot \sqrt{\frac{2 \cdot P}{\rho_w \cdot (1 - Ij) + \rho_p \cdot Ij}}$

Particle velocity $V_0 := Vj$

Abrasive flow rate $m1 := Ij \cdot \left(\frac{Cc \cdot Vj \cdot d_j^2 \cdot \pi \cdot \rho_p}{4}\right)$

$u_x :=$

$100 \cdot \frac{mm}{min}$
$150 \cdot \frac{mm}{min}$
$210 \cdot \frac{mm}{min}$
$270 \cdot \frac{mm}{min}$
$360 \cdot \frac{mm}{min}$
$450 \cdot \frac{mm}{min}$
$1650 \cdot \frac{mm}{min}$
$1700 \cdot \frac{mm}{min}$

$$C_K := \sqrt{\frac{9.6 \cdot \sigma_{ult} \cdot R_f^6}{\rho_p}}$$

$C_K = 932 \cdot m \cdot sec^{-1}$

$$\gamma := 1 + \frac{m1 \cdot \frac{(d_j)^2}{4}}{\left[\frac{.3 \cdot m1 \cdot (d_j)^2}{4}\right]}$$

$\gamma = 4.3$

Initial impact angle

$$\alpha t_x := \frac{V_e}{V_0} + \frac{1}{\left(\frac{14 \cdot ml}{\pi \cdot \rho_p \cdot u_x \cdot d_j^{\,2}}\right)^{.4} \cdot \left(\frac{V_0}{C_K}\right)}$$

$$\alpha t = \begin{bmatrix} 4.6 \\ 5.4 \\ 6.1 \\ 6.8 \\ 7.6 \\ 8.3 \\ 13.9 \\ 14 \end{bmatrix} \cdot deg$$

Transition impact angle

$$\alpha o := \left[\frac{3 \cdot \pi \cdot R_f^{\,.6}}{\frac{14 \cdot \gamma}{\sqrt{\frac{V_0}{C_K}}}}\right]^{\frac{2}{3}}$$

$$\alpha o = 18.7 \cdot deg$$

$$C_{1_x} := if\left(\alpha t_x < \alpha o, 1 - \frac{\alpha t_x}{\alpha o}, 0.0001\right)$$

$$C_{t_x} := if\left(C_{1_x} < 0.5, C_{1_x}, 1 - C_{1_x}\right)$$

$$\theta_x := 2 \cdot acos\left(1 - 2 \cdot C_{t_x}\right)$$

$$A_x := \frac{1}{2 \cdot \pi} \cdot \left(\theta_x - \sin\left(\theta_x\right)\right)$$

$$A_{d_x} := if\left(C_{1_x} < 0.5, A_x, 1 - A_x\right)$$

$$Ac_x := A_{d_x}$$

A_{d_x}

0.812
0.764
0.716
0.675
0.621
0.574
0.207
0.197

Cutting wear depth

$$h_{c_x} := \frac{\frac{V_0}{C_K} \cdot d_j \cdot C_{1_x}}{\left(\frac{\pi \cdot \rho_p \cdot u_x \cdot d_j^{\,2}}{14 \cdot ml \cdot Ac_x}\right)^{.4} + \frac{V_e}{C_K}}$$

$$h_c = \begin{bmatrix} 4.639 \\ 3.644 \\ 2.932 \\ 2.461 \\ 1.98 \\ 1.646 \\ 0.304 \\ 0.284 \end{bmatrix} \cdot mm$$

Deformation wear depth

$$h_{d_x} := \frac{1}{\left[\frac{\pi \cdot d_j \cdot \sigma \cdot u_x}{2 \cdot m1 \cdot (1-0) \cdot (V_0 - V_e)^2} + \frac{C_f}{d_j} \cdot \frac{V_0}{(V_0 - V_e)}\right]}$$

$$h_d = \begin{bmatrix} 9.838 \\ 7.33 \\ 5.614 \\ 4.548 \\ 3.54 \\ 2.898 \\ 0.848 \\ 0.824 \end{bmatrix} \cdot mm$$

$$h_x := if\left(\alpha t_x > \alpha o, h_{d_x}, if\left(V_e > V_0 \cdot \sin(\alpha t_x), h_{d_x}, h_{d_x} + h_{c_x}\right)\right)$$

$E_2 \equiv 125 \cdot 10^9 \cdot \frac{newton}{m^2}$ $E_1 \equiv 96 \cdot 10^9 \cdot \frac{newton}{m^2}$ $\nu_2 \equiv .29$ $\nu_1 \equiv .2$

$Cc \equiv .93$ Nozzle area coefficient $\sigma_y \equiv 125 \cdot 10^6 \cdot \frac{newton}{m^2}$ Material yield strength

$Cv \equiv .9$ Nozzle velocity coefficient $\sigma_{ult} \equiv 355 \cdot 10^6 \cdot \frac{newton}{m^2}$ Material ultimate strength

$R_f \equiv .57$ Roundness factor

$\rho_w \equiv 1000 \cdot \frac{kg}{m^3}$ Density of water $\rho_p \equiv 2800 \cdot \frac{kg}{m^3}$ Abrasive density, kg/m^3

$C_f \equiv .017$ Wall drag, from Re $\sigma \equiv \frac{E_2}{10}$ Material constant, proportional to Youngs modulus, N/mm^2

$$Re := \frac{Vj \cdot d_j}{1.14 \cdot 10^{-6} \cdot \frac{m^2}{sec}}$$ Reynold number for the nozzle flow $\frac{Re}{10^5} = 1.5$

$P \equiv 680 \cdot bar$ Operating pressure, bar $d_j \equiv .53 \cdot mm$ Nozzle diameter, mm

$Ij \equiv 0.0123$ Abrasive concentration by weight

Calculated depth of cut $h = \begin{bmatrix} 14.48 \\ 10.97 \\ 8.55 \\ 7.01 \\ 5.52 \\ 4.54 \\ 1.15 \\ 1.11 \end{bmatrix} \cdot mm$ Cut speed $u = \begin{bmatrix} 100 \\ 150 \\ 210 \\ 270 \\ 360 \\ 450 \\ 1650 \\ 1700 \end{bmatrix} \cdot \frac{mm}{min}$

Depth of cut vs. cutting speed

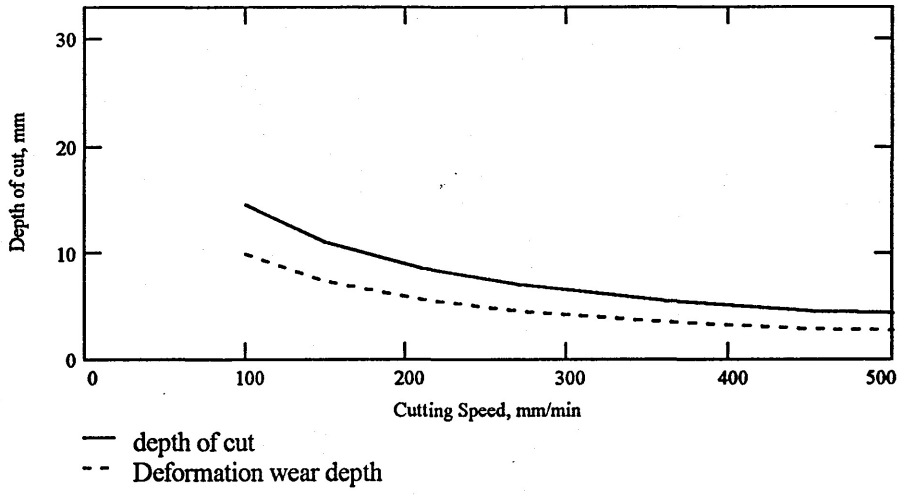

Cut surface area generation $SSU_x := h_x \cdot u_x$

